

# Structure–property relations for resistivity of iron alloys at planetary core conditions

---

## DISSERTATION

zur Erlangung des akademischen Grades eines  
Doktors der Naturwissenschaften (Dr. rer. nat.)

in der

Bayreuther Graduiertenschule für Mathematik und Naturwissenschaften  
(BayNAT)  
der Universität Bayreuth

vorgelegt von

**Fabian Wagle**

geboren in München

Bayreuth, 2018



Die vorliegende Arbeit wurde in der Zeit von Januar 2014 bis Juni 2018 in Bayreuth am Bayerischen Geoinstitut unter Betreuung von Herrn Dr. Gerd Steinle-Neumann angefertigt.

Vollständiger Abdruck der von der Bayreuther Graduiertenschule für Mathematik und Naturwissenschaften (BayNAT) der Universität Bayreuth genehmigten Dissertation zur Erlangung des akademischen Grades eines Doktors der Naturwissenschaften (Dr. rer. nat.).

Dissertation eingereicht am:	27. Juli 2018
Zulassung durch das Leitungsgremium:	29. Juni 2018
Wissenschaftliches Kolloquium:	30. August 2018

Amtierender Direktor: Prof. Dr. Dirk Schüler

**Prüfungsausschuss:**

Dr. Gerd Steinle-Neumann	(Gutachter)
Prof. Dr. Richard Secco	(Gutachter)
Prof. Dr. Dan Frost	(Vorsitz)
Prof. Dr. Gregor Golabek	



*“Ordnung ist die Verbindung des Vielen nach einer Regel”*

— Immanuel Kant



# Summary

Electronic transport properties of iron alloys under extreme conditions are critical parameters for the generation of magnetic fields in terrestrial planets, and thus of great importance for their evolution and habitability. Like many other material properties, electrical resistivity is closely related to the atomic and electronic structure of the material, both of which change with pressure and temperature. This thesis includes three studies on the relationship between structural properties and electrical resistivity of iron alloys at conditions of planetary cores.

In the first part of the thesis, we use density functional theory based molecular dynamics simulations in combination with the Kubo-Greenwood formalism to self-consistently determine atomic structure and electrical resistivity of potential core forming liquid iron alloys, with several weight per cent of silicon, oxygen and sulfur. We observe that with increasing compression and light element concentration, the temperature coefficient of resistivity decreases (for all alloys considered), eventually vanishes (Fe-Si) and even changes sign (Fe-S). By analyzing optical conductivity using a Drude model, we show that the electron mean free path approaches the interatomic distance, causing resistivity to saturate due to a combined effect of temperature, compression and chemical composition. Differences in the degree of saturation between the different alloys are explained by structural observations. In contrast to the interstitial-like incorporation of oxygen, silicon randomly substitutes for iron atoms in the liquid. While the addition of oxygen only marginally shortens the mean free path, silicon does so more efficiently due to its larger scattering cross section. Since the covalent component of bonding between sulfur and iron has been shown to strengthen under pressure, Fe-S alloys exhibit an effective mutual repulsion of sulfur atoms, resulting in high coordination with iron atoms. This leads to an even distribution of impurity atoms in the liquid with less overlap of impurity scattering cross-sections, causing resistivity to saturate more efficiently. A consequence of the saturation limit is the observation of a secondary electronic effect that leads to a negative temperature coefficient of resistivity for high

compression and sulfur concentration. In agreement with Mott’s theory, we find that thermal broadening and the associated decrease of the  $d$ -electron density of states at the Fermi level leads to a decreasing resistivity with increasing temperature.

Based on this analysis, we conclude that resistivity in the Earth’s core cannot exceed  $100 \mu\Omega\text{cm}$ , largely independent of temperature. The evolution of a dynamo is therefore only determined by the boundary conditions changed by a growing inner core and not by a variation of the conductivity profile.

In the second part of the thesis, we describe the resistivity discontinuity of iron along the melting curve, representative for potential inner core boundaries of terrestrial planets. Based on Ziman’s theory in the long-wavelength approximation, we derive an expression for the resistivity ratio of a coexisting solid and liquid phase of a metal at the melting point, which only depends on the corresponding density and compressibility ratios. Good agreement of the theory with experimental data for iron, cobalt and nickel at ambient pressure provides the basis for assuming the validity of this expression at high pressure. By using a thermodynamic model for density and compressibility and a resistivity model for liquid iron based on first-principles computations, we calculate electrical resistivity of solid iron along the melting curve. We find our model to be in good agreement with studies using static and dynamic compression experiments at conditions of the Earth’s core-mantle boundary and first principles computations at conditions of the inner core boundary.

For pure iron, the resistivity discontinuity at pressures of the Earth’s inner core boundary is found to be negligible, and only extreme differences in the chemical composition between outer and inner core would be able to cause a considerable difference in resistivity. Since silicon and sulfur—the elements with the largest influence on resistivity—nearly equally partition between the Earth’s inner and outer core, this scenario is highly unlikely.

# Zusammenfassung

Elektronische Transporteigenschaften von Eisenlegierungen unter extremen Bedingungen gehen als kritische Parameter in die Erzeugung von Magnetfeldern terrestrischer Planeten ein und sind deshalb von großer Wichtigkeit für deren Entwicklung und Bewohnbarkeit. Wie auch viele andere Materialeigenschaften hängt der spezifische elektrische Widerstand eng mit der atomaren und elektronischen Struktur des Materials zusammen, welche sich mit Druck und Temperatur ändern. Die vorliegende kumulative Dissertation enthält drei veröffentlichte Manuskripte, die die Zusammenhänge von Struktureigenschaften mit dem spezifischen Widerstand von Eisenlegierungen unter Bedingungen planetarer Kerne beschreiben.

Im ersten Teil der Dissertation benutzen wir Dichtefunktionaltheorie-basierte Molekulardynamiksimulationen in Kombination mit dem Kubo-Greenwood Formalismus, um auf selbstkonsistente Weise die atomare Struktur und den spezifischen Widerstand von potentiell kernformenden, flüssigen Eisenlegierungen mit Silizium, Sauerstoff und Schwefel zu bestimmen. Wir beobachten, dass der Temperaturkoeffizient des spezifischen Widerstands mit zunehmender Kompression und Konzentration leichter Elemente abnimmt (für alle untersuchten Legierungen) und schließlich verschwindet (Fe-Si), oder sogar das Vorzeichen wechselt (Fe-S). Durch die Analyse der optischen Leitfähigkeit mit Hilfe eines Drude-Modells zeigen wir, dass sich die mittlere freie Elektronenweglänge dem interatomaren Abstand annähert, was eine Sättigung des spezifischen Widerstands aufgrund eines kombinierten Effekts von Temperatur, Kompression und chemischer Zusammensetzung zur Folge hat. Unterschiede im Sättigungsgrad der einzelnen Legierungen werden mit Hilfe von strukturellen Beobachtungen erklärt: Im Gegensatz zu der Zwischengitterplatz-ähnlichen Eingliederung von Sauerstoff ersetzt Silizium auf zufällige Weise Eisenatome in der Flüssigkeit. Während bei Zugabe von Sauerstoff die mittlere freie Weglänge nur unwesentlich verkürzt wird, ist Silizium aufgrund seines größeren Streuquerschnitts dabei effizienter. Da gezeigt

wurde, dass der kovalente Bindungsanteil zwischen Schwefel und Eisen unter dem Einfluss von Druck verstärkt wird, zeigen Fe-S-Legierungen eine effektive gegenseitige Abstoßung von Schwefelatomen, was zu einer hohen Koordination mit Eisenatomen führt. Das wiederum führt zu einer gleichmäßigen Verteilung der Fremdatome mit geringerem Überlapp der entsprechenden Streuquerschnitte und damit zu einer effektiveren Widerstandssättigung. Aufgrund der erreichten Sättigung können wir einen elektronischen Effekt höherer Ordnung beobachten, der bei hoher Kompression und Schwefelkonzentration zu einem negativen Temperaturkoeffizienten des spezifischen Widerstands führt. In Übereinstimmung mit Motts Theorie stellen wir fest, dass thermische Verbreiterung und die damit einhergehende Abnahme der  $d$ -Elektronenzustandsdichte an der Fermikante zu einem abnehmenden Widerstand bei steigender Temperatur führt.

Wir schlussfolgern aufgrund dieser Untersuchungen, dass der spezifische Widerstand im Erdkern  $100 \mu\Omega\text{cm}$  nicht überschreiten kann und weitgehend temperaturunabhängig ist. Die Entwicklung eines Dynamos ist daher nur durch die Randbedingungen bestimmt, die sich durch das Wachstum eines inneren Kerns ändern, jedoch nicht durch ein sich änderndes Leitfähigkeitsprofil.

Im zweiten Teil der Dissertation beschreiben wir die Diskontinuität des spezifischen Widerstands von Eisen entlang der Schmelzkurve, stellvertretend für potentielle innere Kerngrenzen terrestrischer Planeten. Basierend auf Zimans Theorie im Grenzfalle langer Wellenlängen leiten wir einen Ausdruck für das Widerstandsverhältnis von koexistierenden flüssigen und festen Phasen eines Metalls am Schmelzpunkt her, der nur von den dazugehörigen Dichte- und Kompressibilitätsverhältnissen abhängt. Eine gute Übereinstimmung der Theorie mit experimentellen Daten für Eisen, Kobalt und Nickel bei Normaldruck ist die Grundlage für die Annahme, dass dieser Ausdruck seine Gültigkeit auch bei hohem Druck behält. Mit Hilfe eines thermodynamischen Modells für Dichte und Kompressibilität, sowie einem Widerstandsmodell für flüssiges Eisen, das auf Kubo-Greenwood-Simulationen beruht, berechnen wir den spezifischen Widerstand von festem Eisen entlang der Schmelzkurve. Wir stellen fest, dass unser Modell gut mit statischen und dynamischen Kompressionsexperimenten unter Bedingungen der Kern-Mantel-Grenze, sowie mit Simulationsergebnissen unter Bedingungen der inneren Kerngrenze der Erde übereinstimmt.

Im Falle von reinem Eisen wird die Diskontinuität an der inneren Kerngrenze vernachlässigbar; nur extreme Unterschiede in der chemischen Zusammensetzung zwi-

schen äußerem und innerem Erdkern könnten bedeutende Unterschiede im spezifischen Widerstand zur Folge haben. Da Silizium und Schwefel—die Elemente, die den Widerstand am meisten beeinflussen—einen nahezu identischen Verteilungskoeffizienten im inneren und äußeren Erdkern aufweisen, ist dieses Szenario höchst unwahrscheinlich.



# Contents

<b>1 Geophysical motivation</b>	<b>1</b>
Bibliography . . . . .	5
<b>2 Methods</b>	<b>9</b>
2.1 Density functional theory based molecular dynamics . . . . .	9
2.2 Structure of liquids . . . . .	11
2.3 Electrical resistivity . . . . .	15
2.3.1 Drude-Sommerfeld theory . . . . .	15
2.3.2 Ziman theory for resistivity of liquid metals . . . . .	17
2.3.3 Transport within density functional theory . . . . .	18
2.3.4 Resistivity saturation in iron alloys . . . . .	19
Bibliography . . . . .	23
<b>3 Synopsis</b>	<b>29</b>
3.1 Resistivity saturation . . . . .	31
3.2 Negative temperature coefficient of resistivity . . . . .	35
3.3 Resistivity of solid iron . . . . .	39
Bibliography . . . . .	44
<b>4 Wagle <i>et al.</i> (2018), C. R. Geosci. (in press)</b>	<b>49</b>
<b>5 Wagle <i>et al.</i> (2018), Phys. Rev. B 97, 094307</b>	<b>59</b>
<b>6 Wagle &amp; Steinle-Neumann (2018), Geophys. J. Int. 213, 237–243</b>	<b>77</b>



# 1 Geophysical motivation

While the protoplanetary disk in the early history of the solar system was cooling down, higher temperature condensates like silicates and metals coagulated and formed the building blocks for terrestrial planets. Through accretion, they increased in size and mass to form planetesimals and planetary embryos [Wetherill, 1990], until large scale melting due to ongoing impacts, self-compression and radioactive decay allowed droplets of molten metal to segregate from the less dense silicates and form a core [Rubie et al., 2007]. Iron meteorites are regarded as samples of such core material and mainly consist of an iron-nickel alloy [Buchwald, 1975].

Seismic observations reveal a shadow zone for shear wave propagation in the Earth's interior, indicating a core radius of  $\sim 3500$  km, which is—at least partly—in a liquid state [Gutenberg, 1914]. Although an inner core with a radius of  $\sim 1200$  km has been discovered more than 80 years ago by the observation of a seismic discontinuity [Lehmann, 1936], multiply converted shear waves from the inner core unambiguously showed that it is indeed in a solid state much later [Deuss et al., 2000]. In order to match observed densities and seismic velocities in the core, the presence of several weight per cent lighter elements is required in addition to iron and nickel [Birch, 1952]. At least one light element has to favor partitioning into the liquid over the solid, as suggested by the disproportionately high density jump at the inner core boundary [Shearer and Masters, 1990], that cannot solely be explained by the liquid-solid phase transition.

Estimates for approximate proportions of light elements have been based on simultaneously matching density and acoustic velocity from laboratory experiments to seismic reference models and, equally important, satisfying cosmochemical constraints [McDonough, 2003, Badro et al., 2015]. As those elements became enriched in the metal during or after core formation, they must be abundant and/or siderophile at the pres-

## 1 Geophysical motivation

sure and temperature conditions during differentiation and the present day core-mantle boundary.

Silicon is both sufficiently abundant and soluble in iron at both low and high pressures. Requiring reducing conditions during accretion, it is compatible with early core formation [Poirier, 1994] and therefore one of the most likely major light elements in the Earth's core. Sulfur is both cosmochemically abundant and siderophile, and is found in iron meteorites at high concentrations [Chabot, 2004]. The bulk Earth, however, is depleted in sulfur compared to CI carbonaceous chondrites, which best represent the solar abundances of moderately volatile elements [Dreibus and Palme, 1996]. While estimates for the sulfur content in the Earth's core based on this depletion fall below 2 wt.% [Dreibus and Palme, 1996], other terrestrial bodies like Mercury [Rivoldini et al., 2009], Mars [Lodders and Fegley, 1997] and Ganymede [Rückriemen et al., 2015] are expected to accommodate substantially more sulfur in their cores. Although lowering the overall density when alloying with iron, silicon and sulfur cannot account for the higher density deficit in the outer core, as they have been shown to almost equally partition between liquid and solid iron at inner core boundary conditions [Alfè et al., 2002]. Since oxygen is hardly soluble in iron at low pressure, it is assumed to have entered the core when the Earth had reached a considerable size, possibly by reaction with the mantle [Poirier, 1994]. The presence of oxygen would explain the larger density deficit of the outer core, due to its preferred partitioning into the liquid [Alfè et al., 2002]. A ternary iron alloy with silicon and oxygen could satisfy both seismological and geochemical constraints [Badro et al., 2015], and is consistent with the experimental observation of increasing mutual solubility of Si and O in iron with pressure [Tsuno et al., 2013].

Although experiments show the formation of iron hydrides [Fukai and Akimoto, 1983] and carbides [Scott et al., 2001], hydrogen and carbon are too volatile to build up in large amounts in the Earth's core [McDonough, 2003]. Based on an extrapolation of the volatility trend, their concentration in the core is likely below 0.2 %, which is smaller by one to two orders of magnitude than the major candidates described in the previous paragraph.

Physical properties of the core-forming alloys, like viscosity and electrical and thermal conductivity have a strong influence on possibly active dynamos in terrestrial planets. The Earth's magnetic field is generated by a convection-driven magneto-hydrodynamic (MHD) dynamo, converting the kinetic energy of a vortex pattern in the outer core

into magnetic energy [Merrill et al., 1996]. Space missions revealed that also Mercury and Ganymede exhibit an internally generated magnetic field [Ness, 1979, Kivelson et al., 2002], and large remanence fields indicate that Mars must have had an active dynamo, before it disappeared due to thermal death about four billion years ago [Weiss et al., 2002]. A magnetic field is vital for the habitability of a planet, as it prevents atmospheric erosion and protects the surface from highly energetic particles of the solar wind [Lammer et al., 2009].

The balance of generation and dissipation of a magnetic field  $\mathbf{H}$  in the context of MHD dynamos, and in the presence of an external magnetic field  $\mathbf{H}_{\text{ext}}$ , is described by the induction equation

$$\frac{\partial \mathbf{H}}{\partial t} = \frac{\rho_{\text{el}}}{\mu} \Delta \mathbf{H} + \nabla \times [\mathbf{v} \times (\mathbf{H} + \mathbf{H}_{\text{ext}})]. \quad (1.1)$$

If the vorticity of the Lorentz force in a convecting fluid with velocity field  $\mathbf{v}$  (proportional to the second term on the right hand side of Equation 1.1) vanishes, the magnetic field obeys a law of free diffusion ( $\propto \Delta \mathbf{H}$ ), at a rate determined by electrical resistivity  $\rho_{\text{el}}$  and magnetic permeability  $\mu$ .

In that sense, electronic transport properties of core material is crucial for the evolution of a planet. Since electrical resistivity determines the dissipation rate of the magnetic field, it sets the timescale for the decay of a magnetic dipole and a lower limit for the fluid velocity required for the generation of a magnetic field [Davies et al., 2015]. Thermal conductivity, generally related to electrical resistivity by the Wiedemann-Franz law, determines the heat flux along the core adiabat and the thermal gradient across the dynamo-active region, driving the convection necessary for a MHD dynamo to emerge from Equation (1.1). Several computational and experimental studies of recent years found high conductivity values of iron alloys at conditions of the Earth's core [de Koker et al., 2012, Pozzo et al., 2012, 2013, Gomi et al., 2013, Seagle et al., 2013]. This has severe consequences for the energy budget of the dynamo, leading to the conclusion that the Earth's magnetic field cannot be generated by a purely thermally driven dynamo. Instead, the buoyancy of exsolved light elements upon freezing of the inner core is required for driving thermo-chemical convection and explains the present day magnetic field [Olson, 2013].

A finite inner core resistivity has been found to have a stabilizing effect on the geodynamo in simulations, decreasing the frequency of global field reversals [Dharmaraj and

## 1 *Geophysical motivation*

Stanley, 2012]. Although these results are controversial [Wicht, 2002, Lhuillier et al., 2013], electrical resistivity of the Earth’s inner core might be of some relevance for a dynamo in terms of the magnetic boundary conditions during cooling of a planet. Resistivity of solid iron differs from that of liquid iron at ambient [van Zytveld, 1980] and low pressure [Secco and Schlössin, 1989], a discontinuity which has not yet been rigorously investigated along the melting curve towards conditions of the Earth’s inner core boundary. As the atomic structure influences electronic transport and the stable phase of the Earth’s inner core is still under debate [e.g., Tateno et al., 2010, Belonoshko et al., 2017], further research is required.

The scope of this thesis is to analyze structure-property relations for electrical resistivity of iron alloys at conditions of planetary cores, based on computations using density functional theory. In the two following chapters, I give an overview over the methods used and relevant aspects of their theoretical background (Chapter 2), and summarize the published manuscripts on the topic (Chapter 3). The manuscript themselves are included as Chapters 4–6.

## Bibliography

- D. Alfè, M. J. Gillan, and G. D. Price. Composition and temperature of the Earth's core constrained by combining ab initio calculations and seismic data. Earth Planet. Sci. Lett., 195:91–98, 2002. doi: 10.1016/S0012-821X(01)00568-4.
- J. Badro, J. P. Brodholt, H. Piet, J. Siebert, and F. J. Ryerson. Core formation and core composition from coupled geochemical and geophysical constraints. Proc. Natl. Acad. Sci. USA, 112:12310–12314, 2015. doi: 10.1073/pnas.1505672112.
- A. B. Belonoshko, T. Lukinov, J. Fu, J. Zhao, S. Davis, and S. I. Simak. Stabilization of body-centred cubic iron under inner-core conditions. Nat. Geosci., 10:312–316, 2017. doi: 10.1038/ngeo2892.
- F. Birch. Elasticity and constitution of the Earth's interior. J. Geophys. Res., 57: 227–286, 1952. doi: 10.1029/JZ057i002p00227.
- V. F. Buchwald. Handbook of Iron Meteorites. University of California Press, Berkeley, 1975.
- N. L. Chabot. Sulfur contents of the parental metallic cores of magmatic iron meteorites. Geochim. Cosmochim. Acta, 68:3607–3618, 2004. doi: 10.1016/j.gca.2004.03.023.
- C. Davies, M. Pozzo, D. Gubbins, and D. Alfè. Constraints from material properties on the dynamics and evolution of Earth's core. Nat. Geosci., 8:678–685, 2015. doi: 10.1038/ngeo2492.
- N. de Koker, G. Steinle-Neumann, and V. Vlček. Electrical resistivity and thermal conductivity of liquid Fe alloys at high P and T, and heat flux in Earth's core. Proc. Natl. Acad. Sci. USA, 109:4070–4073, 2012. doi: 10.1073/pnas.1111841109.
- A. Deuss, J. H. Woodhouse, H. Paulssen, and J. Trampert. The observation of inner core shear waves. Geophys. J. Int., 142:67–73, 2000. doi: 10.1046/j.1365-246x.2000.00147.x.
- G. Dharmaraj and S. Stanley. Effect of inner core conductivity on planetary dynamo models. Phys. Earth Planet. Inter., 212:1–9, 2012. doi: 10.1016/j.pepi.2012.09.003.

## BIBLIOGRAPHY

- G. Dreibus and H. Palme. Cosmochemical constraints on the sulfur content in the Earth's core. Geochim. Cosmochim. Acta, 60:1125–1130, 1996. doi: 10.1016/0016-7037(96)00028-2.
- Y. Fukai and S. Akimoto. Hydrogen in the Earth's core. Proc. Japan Acad., 59: 158–162, 1983. doi: 10.2183/pjab.59.158.
- H. Gomi, K. Ohta, K. Hirose, S. Labrosse, R. Caracas, M. J. Verstraete, and J. W. Hernlund. The high conductivity of iron and thermal evolution of the Earth's core. Phys. Earth Planet. Inter., 224:88–103, 2013. doi: 10.1016/j.pepi.2013.07.010.
- B. Gutenberg. Über Erdbebenwellen VIIA. Nachr. Ges. Wiss. Göttingen Math. Physik. Kl., 125:166–218, 1914.
- M. G. Kivelson, K. K. Khurana, and M. Volwerk. The permanent and inductive magnetic moments of Ganymede. Icarus, 157:507–522, 2002. doi: 10.1006/icar.2002.6834.
- H. Lammer, J. H. Bredehöft, A. Coustenis, M. L. Khodachenko, L. Kaltenegger, O. Grasset, D. Prieur, F. Raulin, P. Ehrenfreund, M. Yamauchi, J.-E. Wahlund, J.-M. Grießmeier, G. Stangl, C. S. Cockell, Y. N. Kulikov, J. N. Grenfell, and H. Rauer. What makes a planet habitable? Astron. Astrophys. Rev., 17:181–249, 2009. doi: 10.1007/s00159-009-0019-z.
- I. Lehmann. *P'*. Publ. Bur. Cent. Seismol. Int. A, 14:87–115, 1936.
- F. Lhuillier, G. Hulot, and Y. Gallet. Statistical properties of reversals and chrons in numerical dynamos and implications for the geodynamo. Phys. Earth Planet. Inter., 220:19–36, 2013. doi: 10.1016/j.pepi.2013.04.005.
- K. Lodders and B. Fegley. An oxygen isotope model for the composition of Mars. Icarus, 126:373–394, 1997. doi: 10.1006/icar.1996.5653.
- W. F. McDonough. Compositional model for the Earth's core. In R. W. Carlson, editor, Treatise on Geochemistry, volume 2, pages 547–568. Elsevier, Amsterdam, 2003. doi: 10.1016/B0-08-043751-6/02015-6.
- R. T. Merrill, M. W. McElhinny, and P. L. McFadden. The Magnetic Field of the Earth: Paleo-magnetism, the Core and the Deep Mantle. Academic Press, San Diego, 1996.
- N. F. Ness. The magnetic field of Mercury. Phys. Earth. Planet Inter., 20:209–217, 1979. doi: 10.1016/0031-9201(79)90044-X.

- P. Olson. The new core paradox. Science, 342:431–432, 2013. doi: 10.1126/science.1243477.
- J.-P. Poirier. Light elements in the Earth’s outer core: A critical review. Phys. Earth Planet. Inter., 85:319–337, 1994. doi: 10.1016/0031-9201(94)90120-1.
- M. Pozzo, C. Davies, D. Gubbins, and D. Alfè. Thermal and electrical conductivity of iron at Earth’s core conditions. Nature, 485:355–358, 2012. doi: 10.1038/nature11031.
- M. Pozzo, C. Davies, D. Gubbins, and D. Alfè. Transport properties for liquid silicon-oxygen-iron mixtures at Earth’s core conditions. Phys. Rev. B, 87:014110, 2013. doi: 10.1103/PhysRevB.87.014110.
- A. Rivoldini, T. Van Holst, and O. Verhoeven. The interior structure of Mercury and its core sulfur content. Icarus, 201:12–30, 2009. doi: 10.1016/j.icarus.2008.12.020.
- D. C. Rubie, F. Nimmo, and H. J. Melosh. Formation of Earth’s core. In D. J. Stevenson, editor, Treatise on Geophysics, volume 9, pages 51–90. Elsevier, Amsterdam, 2007. doi: 10.1016/B978-0-444-53802-4.00154-8.
- T. Rückriemen, D. Breuer, and T. Spohn. The Fe snow regime in Ganymede’s core: A deep-seated dynamo below a stable snow zone. J. Geophys. Res. Planets, 120: 1095–1118, 2015. doi: 10.1002/2014JE004781.
- H. P. Scott, Q. Williams, and E. Knittle. Stability and equation of state of Fe<sub>3</sub>C to 73 GPa: Implications for carbon in the Earth’s core. Geophys. Res. Lett., 28: 1875–1878, 2001. doi: 10.1029/2000GL012606.
- C. T. Seagle, E. Cottrell, Y. Fei, D. R. Hummer, and V. B. Prakapenka. Electrical and thermal transport properties of iron and iron-silicon alloy at high pressure. Geophys. Res. Lett., 40:5377–5381, 2013. doi: 10.1002/2013GL057930.
- R. A. Secco and H. H. Schlössin. The electrical resistivity of solid and liquid Fe at pressures up to 7 GPa. J. Geophys. Res. Solid Earth, 94:5887–5894, 1989. doi: 10.1029/JB094iB05p05887.
- P. Shearer and G. Masters. The density and shear velocity contrast at the inner core boundary. Geophys. J. Int., 102:491–498, 1990. doi: 10.1111/j.1365-246X.1990.tb04481.x.

## BIBLIOGRAPHY

- S. Tateno, K. Hirose, Y. Ohishi, and Y. Tatsumi. The structure of iron in Earth's inner core. Science, 330:359–361, 2010. doi: 10.1126/science.1194662.
- K. Tsuno, D. J. Frost, and D. C. Rubie. Simultaneous partitioning of silicon and oxygen into the Earth's core during early Earth differentiation. Geophys. Res. Lett., 40:66–71, 2013. doi: 10.1029/2012GL054116.
- J. B. van Zytveld. Electrical resistivities of liquid transition metals. Journal de Physique, 41:503–506, 1980. doi: 10.1051/jphyscol:19808126.
- B. P. Weiss, H. Vali, F. J. Baudenbacher, J. L. Kirschvink, S. T. Stewart, and D. L. Shuster. Records of an ancient Martian magnetic field in ALH84001. Earth Planet. Sci. Lett., 201:449–463, 2002. doi: 10.1016/S0012-821X(02)00728-8.
- G. W. Wetherill. Formation of the Earth. Annu. Rev. Earth Planet. Sci., 18:205–256, 1990. doi: 10.1146/annurev.ea.18.050190.001225.
- J. Wicht. Inner-core conductivity in numerical dynamo simulations. Phys. Earth Planet. Inter., 132:281–302, 2002. doi: 10.1016/S0031-9201(02)00078-X.

# 2 Methods and theoretical background

## 2.1 Density functional theory based molecular dynamics

The development of density functional theory (DFT) has been groundbreaking for calculating physical properties of quantum many-particle systems. This mean-field approach to electronic many-body interactions is based on the theorem of Hohenberg and Kohn [1964], which states that

1. the total energy of an  $N$ -electron system is a unique functional of the electron density  $n(\mathbf{r})$ , and
2. that this functional takes a minimum (the ground state energy) if and only if  $n(\mathbf{r})$  is the ground state density.

For determining the ground state energy, it is therefore not necessary to solve the many body Schrödinger equation, but to find the density for which the total energy becomes minimal. This is done by iteratively solving  $N$  single particle Schrödinger-like equations, the Kohn-Sham equations (here in atomic units) [Kohn and Sham, 1965]:

$$\left(-\frac{1}{2}\nabla^2 + v_{\text{eff}}(\mathbf{r}) - \epsilon_j\right) \phi_j(\mathbf{r}) = 0. \quad (2.1)$$

In Equation (2.1),  $\phi_j(\mathbf{r})$  are single particle Kohn-Sham wave functions,  $\epsilon_j$  the corresponding energy eigenvalues and

$$v_{\text{eff}}(\mathbf{r}) = v_{\text{ext}}(\mathbf{r}) + \int \frac{n(\mathbf{r}')}{|\mathbf{r} - \mathbf{r}'|} d\mathbf{r}' + v_{\text{xc}}(\mathbf{r}) \quad (2.2)$$

the effective potential acting on the electrons, decomposed in external potential  $v_{\text{ext}}(\mathbf{r})$  (e.g., Coulomb field of the nuclei), the electrostatic interaction between electrons (Hartree-term) and the exchange-correlation potential  $v_{\text{xc}}(\mathbf{r})$ . In DFT, the complexity due to many body interactions is treated by making approximations to  $v_{\text{xc}}(\mathbf{r})$ . One class of energy functionals uses the local spin density approximation (LSDA), where  $v_{\text{xc}}(\mathbf{r})$  depends on electron density at each point in space only and which, for example, describes the energy of exchange and correlation by that of a homogeneous electron gas of equal density. Although this approach has been applied very successfully for many systems [Jones and Gunnarsson, 1989], taking density gradients into account generally improves total and atomization energies [Perdew et al., 1993], and compensates for overbinding in LSDA predictions of bond lengths [Ozoliņš and Körling, 1993, Stixrude et al., 1994].

Starting from an arbitrary guess for  $n(\mathbf{r})$  (typically an overlap of atomic charge densities), one can calculate  $v_{\text{eff}}(\mathbf{r})$ , solve Equation (2.1) for  $\epsilon_j$  and  $\phi_j(\mathbf{r})$  and construct a new density by summing over the probability density of all Kohn-Sham orbitals, i.e.,

$$n(\mathbf{r}) = \sum_{j=1}^N |\phi_j(\mathbf{r})|^2. \quad (2.3)$$

This procedure is continued, until the total energy is minimal. Since we are interested in physical properties of infinite systems (treated by finite simulation boxes with periodic boundary conditions), plane waves provide a convenient choice for a basis set to expand  $\phi_j(\mathbf{r})$ .

Once the electronic ground state for a configuration of atoms has been found, forces can be computed using the Hellmann-Feynman theorem [Feynman, 1939], and the atoms can be displaced according to Newton's equations of motion. This can be used to perform molecular dynamics (MD) simulations in the Born-Oppenheimer approximation, in which the timescales of the atomic and electronic sub-systems are separated.

For this work, we use the Vienna Ab-initio Simulation Package (VASP) [Kresse and Hafner, 1993, Kresse and Furthmüller, 1996a,b] with pre-computed atomic data files within the projector augmented wave (PAW) method [Kresse and Joubert, 1999] and the PBE generalized gradient approximation [Perdew et al., 1996]. Cubic cells containing 128 atoms have been set up at constant volumes  $V$  (covering a pressure range between 0 and 360 GPa) based on liquid structures from previous studies. The oc-

cupation of electronic states obeys the Fermi-Dirac statistics at a fixed temperature  $T$ . We performed MD simulations in the  $N$ - $V$ - $T$  ensemble using the Nosé-thermostat [Nosé, 1984] at a time step of 1 fs and discarded the first few ps to allow for equilibration of the system. Computational parameters have been optimized with respect to performance and all necessary convergence tests have been performed. Non-vanishing slopes of the mean square displacement (MSD)

$$\text{MSD}(t) = \langle |\mathbf{r}_i(t) - \mathbf{r}_i(t_0)|^2 \rangle \quad (2.4)$$

from the MD trajectories, where  $\mathbf{r}_i(t)$  is the position of particle  $i$  at time step  $t$  and  $\langle \cdot \rangle$  the average over varying origin times  $t_0$  and particles, prove that the systems are indeed in a liquid state.

## 2.2 Structure of liquids

The radial distribution function  $g_{\alpha\beta}(r)$  describes the density variation of particles of type  $\alpha$  ( $\rho_\alpha$ ) as a function of distance from a reference particle of type  $\beta$  and is defined such that  $4\pi r^2 \rho_\beta g_{\alpha\beta}(r) dr$  is equal to the number of  $\alpha$ -particles in a spherical shell between  $r$  and  $r + dr$  around a  $\beta$ -particle. In a perfect crystal,  $g_{\alpha\beta}(r)$  has sharp peaks, corresponding to crystallographic sites and their respective coordination with atoms of a certain species. Since every atom can be reached by a set of symmetry operations on a reference atom of the same crystallographic site, particle density still varies at long distance from the reference atom. This long range order remains essentially unchanged by thermal vibrations of the crystal lattice, except for an observed peak broadening in  $g_{\alpha\beta}(r)$ .

Liquid and amorphous solid structures are characterized by the absence of long-range order, as illustrated in Figure 2.1. The pair distribution function is zero up to an effective hard-sphere radius, exhibits several maxima and minima of decaying amplitude and approaches unity (the limit of an ideal gas) for large  $r$ . Although the distributions of first and second nearest neighbor shells overlap, we define the first coordination number of  $\beta$ - around  $\alpha$ -particles as

$$C_{\alpha\beta} = 4\pi \rho_\beta \int_0^{r_{\min}} r^2 g_{\alpha\beta}(r) dr, \quad (2.5)$$

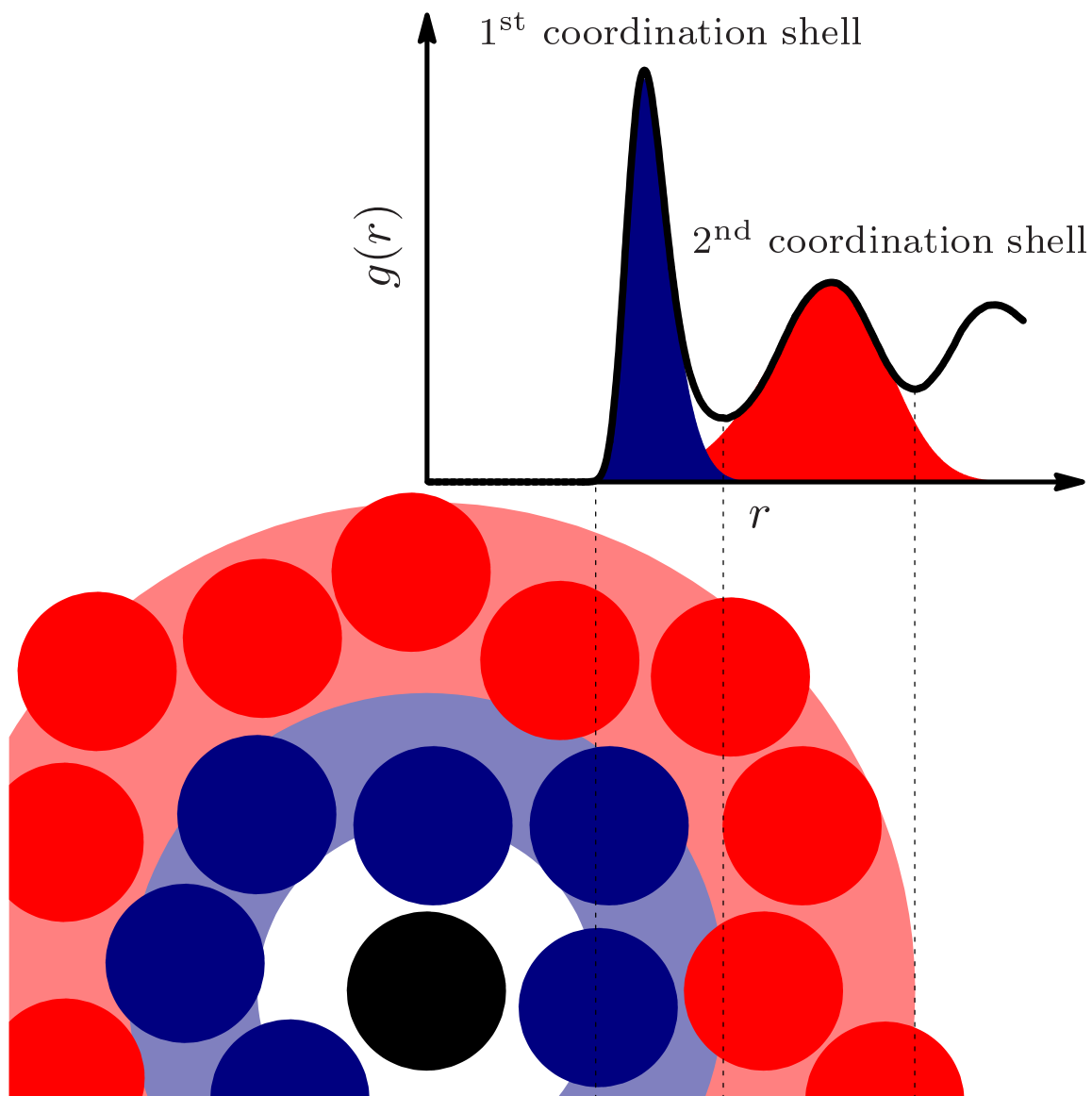


Figure 2.1: Illustration of the atomic short range order in a liquid (with first and second coordination shell in blue and red respectively) and its relation to the radial distribution function.

where the upper integration limit is the first minimum of  $g_{\alpha\beta}(r)$ . The individual distributions are asymmetric, allowing for several possible definitions of the interatomic distance: While we use the first maximum (mode) of the distribution in Chapter 5, we decided to change the definition in favor of the median between zero and the first minimum (Chapter 4). This definition better represents a typical bond length in the liquid and is more consistent with our definition of  $C_{\alpha\beta}$  from Equation (2.5). In our studies,  $g_{\alpha\beta}(r)$  was computed by post-processing and time-averaging over all equilibrated DFT-MD frames.

Equivalent information in momentum space is provided by the static structure factor  $S(q)$ , which is related to  $g(r)$  (here without the subscript, representing the case of a monoatomic liquid) by

$$S(q) = 1 + \rho \int_V e^{-i\mathbf{q}\cdot\mathbf{r}} g(r) d\mathbf{r}, \quad (2.6)$$

where  $\mathbf{q} = \mathbf{k} - \mathbf{k}'$  is the momentum change of a particle scattering off the structure, as for example, in neutron scattering experiments. In the limit of small scattering wavenumbers  $q = |\mathbf{k} - \mathbf{k}'|$  (or long wavelengths), the value of  $S(q)$  is related to thermodynamic properties by fluctuation theory [March, 1990]

$$\lim_{q \rightarrow 0} S(q) = \rho k_B T \beta_T, \quad (2.7)$$

where  $k_B$  is Boltzmann's constant and  $\beta_T$  isothermal compressibility. In the analysis of diffraction experiments and computations, this value cannot be directly determined, due to geometrical limitations of the experimental setup and the finite size of the simulation cell.

An analytic expression for  $S(q)$  exists for a hard sphere liquid [Wertheim, 1963, Ashcroft and Lekner, 1966] in the form

$$S(q) = \left\{ 1 + 4\pi\rho\sigma^3 \int_0^1 ds s^2 \frac{\sin(sq\sigma)}{sq\sigma} (\alpha + \beta s + \gamma s^3) \right\}^{-1}, \quad (2.8)$$

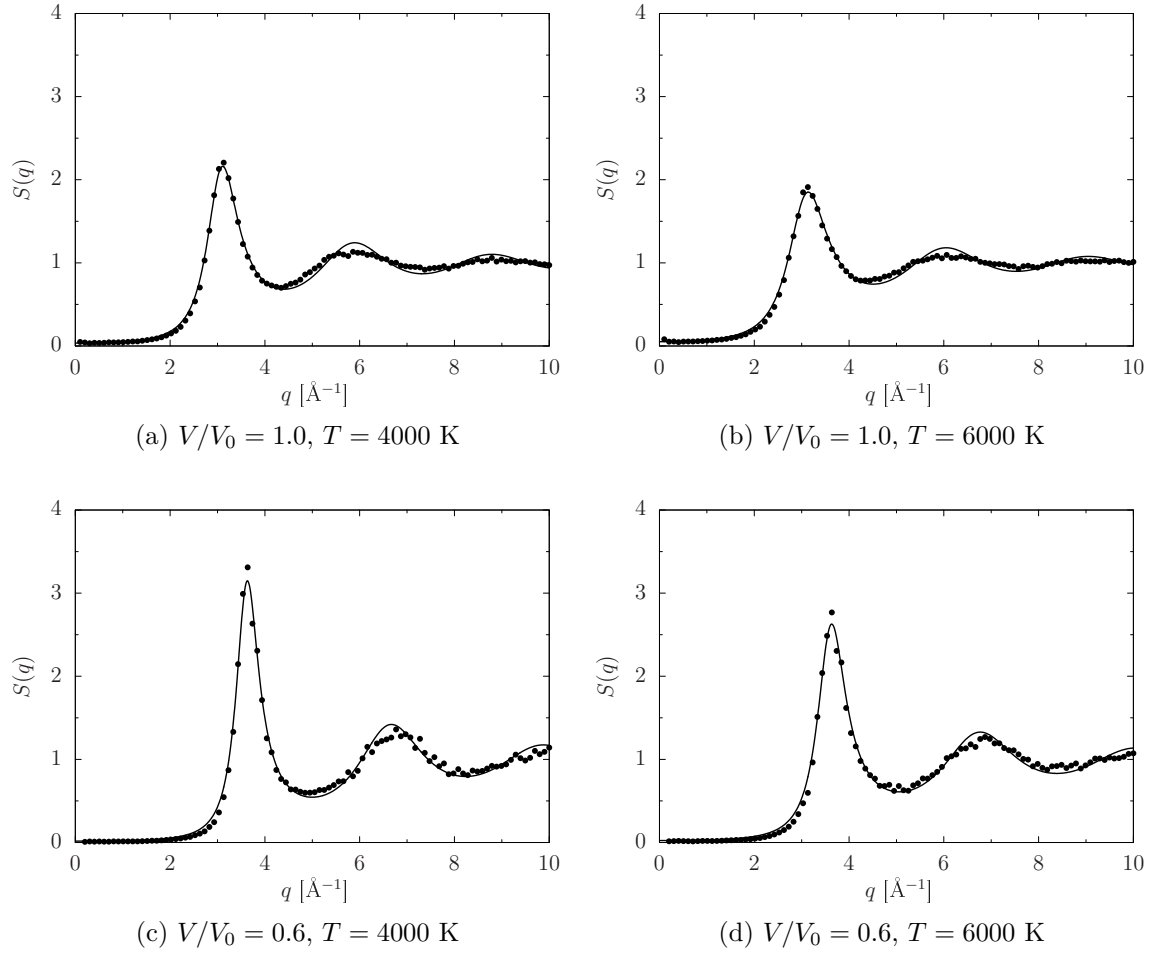


Figure 2.2: Static structure factor of liquid iron at different fractions of  $V_0 = 11.82 \text{ \AA}^3/\text{atom}$  and temperatures from molecular dynamics simulations (dots), with corresponding hard sphere fits (lines).

when using the Percus-Yevick closure relation [Percus and Yevick, 1958] to the Ornstein-Zernicke equation [Ornstein and Zernike, 1914]. The parameters  $\alpha$ ,  $\beta$  and  $\gamma$  are functions of the packing fraction  $\eta = (\pi/6)\rho\sigma^3$ :

$$\begin{aligned}\alpha &= (1 + 2\eta)^2 / (1 - \eta)^4 \\ \beta &= -6\eta(1 + \eta/2)^2 / (1 - \eta)^4 \\ \gamma &= (1/2)(1 + 2\eta)^2 / (1 - \eta)^4.\end{aligned}\tag{2.9}$$

With only two free parameters, namely density  $\rho$  and effective hard sphere radius  $\sigma$ , this expression can be used to fit  $S(q)$  from experiments or from MD data in order to extrapolate to the long wavelength limit (Figures 2.2 and S4 of Chapter 6).

Both  $g(r)$  and  $S(q)$  depend on pressure and temperature; peaks sharpen and shift to smaller  $r$ /larger  $q$  with increasing compression and broaden under the influence of temperature (Figure 2.2).

## 2.3 Electrical resistivity

### 2.3.1 Drude-Sommerfeld theory

In the absence of an external field, Drude's theory [Drude, 1900a,b] describes valence electrons in a metal to behave as free particles between collisions with rigid ions. Scattering events due to a yet unspecified mechanism occur instantaneously and, after an average time  $\tau$ , randomize the momentum of the scattered particle (relaxation time approximation). In the presence of an electric field  $\mathbf{E}$ , the random motion characterized by collisions is superimposed by a net momentum, resulting in a current density  $\mathbf{j}$ . Based on these assumptions, Ohm's law is recovered for a direct current (DC):

$$\mathbf{j} = \sigma_0 \mathbf{E},\tag{2.10}$$

with the DC conductivity (the inverse of resistivity  $\rho_{\text{el}}$ )

$$\sigma_0 = \frac{n_e e^2 \tau}{m_e}\tag{2.11}$$

## 2 Methods

and  $e$ ,  $n_e$  and  $m_e$  charge, number density and mass of an electron respectively. For an alternating current (AC), conductivity depends on frequency  $\omega$

$$\sigma(\omega) = \frac{\sigma_0}{1 - i\omega\tau}. \quad (2.12)$$

The real part

$$\Re[\sigma(\omega)] = \frac{\sigma_0}{1 + (\omega\tau)^2} \quad (2.13)$$

represents the in-phase current component, which is responsible for Joule heating and therefore for the dissipation of the magnetic field in Equation (1.1).

By taking into account that electrons obey Fermi-Dirac statistics instead of Boltzmann statistics from classical kinetic gas theory, Sommerfeld resolved many shortcomings of Drude's original theory [Sommerfeld, 1928], including the temperature dependence of electronic heat capacity and the Wiedemann-Franz law

$$\lambda\rho_{\text{el}} = L_0T. \quad (2.14)$$

With the Lorenz number from Drude-Sommerfeld theory,

$$L_0 = \frac{\pi^2}{3} \left( \frac{k_B}{e} \right)^2 \approx 2.44 \cdot 10^{-8} \text{ W}\Omega\text{K}^{-2}, \quad (2.15)$$

experimental observations of thermal conductivity  $\lambda$  could be explained [Ashcroft and Mermin, 1976].

Another consequence of Fermi-Dirac occupation of electronic states is that only electrons in a environment of  $k_B T$  around the Fermi energy  $E_F$  contribute to conduction and move through the metal at the Fermi-velocity  $v_F = \sqrt{2E_F/m_e}$ . The mean free path of an electron, which is defined as the average distance between collisions, is then simply

$$x = v_F\tau. \quad (2.16)$$

Despite its simplicity, the free electron model of metallic conduction has been successfully describing metals at room temperature in many ways, e.g., by predicting the Hall coefficient, magnetoresistance, electrical conductivity and its relation to thermal conductivity via the Wiedemann-Franz law [Ashcroft and Mermin, 1976].

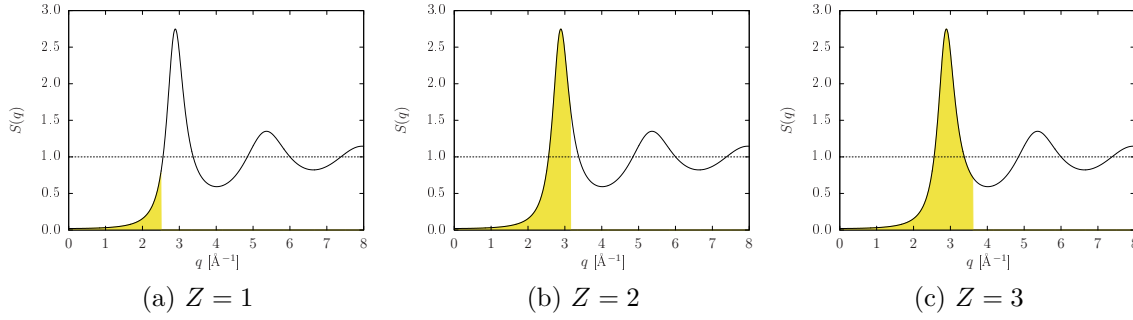


Figure 2.3: Schematic illustration of the static structure factor with the range of the integral in Equation (2.17) marked by the yellow area.

### 2.3.2 Ziman theory for resistivity of liquid metals

Using a so-called nearly free electron model, Ziman [1961] developed a theory for resistivity of liquid metals. It includes a more detailed consideration of the scattering mechanism and the structure of the liquid, both of which are included in the explicit evaluation of the collision integral in Boltzmann's semi-classical transport equation.

The collision integral, which describes the changing rate of the distribution function due to scattering, depends on the transition probability of an electronic state  $\mathbf{k}$  to a state  $\mathbf{k}'$  during a scattering event at an atomic potential  $U(q)$  and the spatial distribution of scattering centers, represented by the static structure factor  $S(q)$ . In the relaxation time approximation, the collision integral is proportional to  $\tau^{-1}$ , which can be substituted in Equation (2.11) to obtain

$$\rho_{\text{el}} = \frac{a_0 \hbar}{e^2} \frac{4\pi^3 Z}{a_0 k_F} \frac{1}{(2k_F)^4} \int_0^{2k_F} S(q) |U(q)|^2 q^3 dq, \quad (2.17)$$

where  $a_0 \hbar / e^2 \approx 21.74 \mu\Omega\text{cm}$  is the atomic unit of resistivity,  $Z$  the number of valence electrons,  $a_0$  the Bohr radius and  $k_F$  the Fermi wavenumber.

This approach has successfully predicted the resistivity of simple liquid metals [Ashcroft and Lekner, 1966] using model potentials for  $U(q)$  [Heine and Abarenkov, 1963, Abarenkov and Heine, 1965, Ashcroft, 1966], and explained the concentration dependence of binary liquid alloys [Faber and Ziman, 1965] and the temperature coefficient of resistivity (TCR) of liquid divalent metals [Güntherodt et al., 1976].

The integrand in Equation (2.17) is weighted strongly towards the upper integration limit  $\propto q^3$ , accounting for the fact that backscattered electrons ( $\mathbf{k}_F \rightarrow -\mathbf{k}_F$ ) contribute most to total resistivity. Therefore the valence is expected to determine the resistivity value (Figure 2.3). Since peaks of  $S(q)$  broaden with temperature, the amplitude of  $S(q)$  decreases at  $2k_F$  for divalent metals and explains the experimentally observed negative TCR for e.g., Eu, Yb and Ba [Güntherodt et al., 1976].

However, the integral also depends on the relative positions of peaks of  $S(q)$ , nodes of  $U(q)$  and the value of  $2k_F$ . The sensitivity with respect to the choice of model potentials, the change of  $2k_F$  with density and the complex electronic structure of iron, not accounted for by the theory in this simple form, does not permit a reliable determination of absolute resistivity values for our geophysical purposes. Efforts to replace local model potentials  $U(q)$  by the  $\mathcal{T}$ -matrix using a muffin-tin model were more successful in describing resistivity of transition metals [Evans et al., 1971]. This has also been applied for iron at conditions of the Earth’s core [Jain and Evans, 1971], yielding resistivity values which are larger by  $\sim 50\%$  compared to the Kubo-Greenwood results by de Koker et al. [2012].

Since predicting absolute resistivity values for iron alloys at high pressure/temperature conditions is problematic within the basic theory, we investigate its applicability on relative values at the solid-liquid phase transition. Ziman [1961] proposed that, as a first order approximation, the integral in Equation (2.17) is proportional to  $S(0)$ , which is related to  $\varrho$  and  $\beta_T$  by Equation (2.7). By taking the ratio of resistivity in the liquid and solid state at the melting point ( $T_m$ ) and accounting for the density dependence of  $k_F$  by a free electron model, the following simple expression holds (for derivation, see Chapter 6):

$$\frac{\rho_{\text{el}}^{\text{liquid}}}{\rho_{\text{el}}^{\text{solid}}} \simeq \frac{\beta_T^{\text{liquid}}}{\beta_T^{\text{solid}}} \left( \frac{\varrho^{\text{liquid}}}{\varrho^{\text{solid}}} \right)^{-2}. \quad (2.18)$$

### 2.3.3 Transport within density functional theory

In the Kubo-Greenwood theory [Kubo, 1957, Greenwood, 1958], electrical conductivity is derived from the first-order response of the density matrix to an electric field. Using

the reformulation by Chester and Thellung [1959], it is possible to calculate  $\sigma(\omega)$  explicitly within DFT by

$$\sigma(\omega) = \frac{\hbar e^2}{V_{\text{cell}}} \sum_{k',k} [f(\epsilon_{k'}) - f(\epsilon_k)] \delta(\epsilon_{k'} - \epsilon_k - \hbar\omega) \langle \psi_k | \hat{\mathbf{v}} | \psi_{k'} \rangle \langle \psi_{k'} | \hat{\mathbf{v}} | \psi_k \rangle, \quad (2.19)$$

where  $\psi_k$  and  $\psi_{k'}$  label electronic states with eigenvalues  $\epsilon_k$  and  $\epsilon_{k'}$ ,  $\hbar$  denotes the reduced Planck constant,  $V_{\text{cell}}$  the cell volume,  $\hat{\mathbf{v}} = 1/\hbar \cdot \partial\mathcal{H}/\partial\mathbf{k}$  the velocity operator with Hamiltonian  $\mathcal{H}$  and  $\mu_e$  the electronic chemical potential. Although electron-electron scattering and dynamical screening are neglected by the approach, using Kohn-Sham orbitals in Equation (2.19) yields the exact short-time dynamics in the semi-classical limit [Dufty et al., 2018].

As simulation cells in DFT-MD simulations are comparatively small and a momentary set of atomic coordinates can have a large impact on the electronic ground state, one needs to sample representative configurations of the system. In order to ensure that such snapshots are uncorrelated, we perform long DFT-MD runs and choose them separated by time periods longer than the decay time of the velocity autocorrelation function. Kohn-Sham wave functions  $\psi_k$ , their eigenvalues  $\epsilon_k$  and the Cartesian gradients of the Hamiltonian with respect to a shift in wave-vector  $\partial\mathcal{H}/\partial\mathbf{k}$  are computed using the *Abinit* software package [Gonze, 1997, Gonze et al., 2009, Torrent et al., 2008]. Equation (2.19) is implemented in the *conducti* module for *Abinit* [Recoules and Crocombette, 2005] and evaluated for each snapshot.

An average over  $\sigma(\omega)$  from Equation (2.19) and independent snapshots are well represented by the Drude model (Equation 2.13), which is used for extrapolating to the DC conductivity limit  $\sigma_0$  and to determine the relaxation time  $\tau$  of the system (Figures 2.4 and S1 in Chapter 5).

### 2.3.4 Resistivity saturation in iron alloys

The Fermi level intersects both the  $3d$ - and the  $4s$ -band of iron, which strongly influences electronic transport. Due to the difference in effective mass, the Fermi velocity is much lower in the  $d$ -band and therefore most of the current is transported by  $s$ -electrons. Electronic transitions from  $s$ - into  $d$ -states can be induced by scattering with phonons and are the reason for the high resistivity of transition metals [Mott,

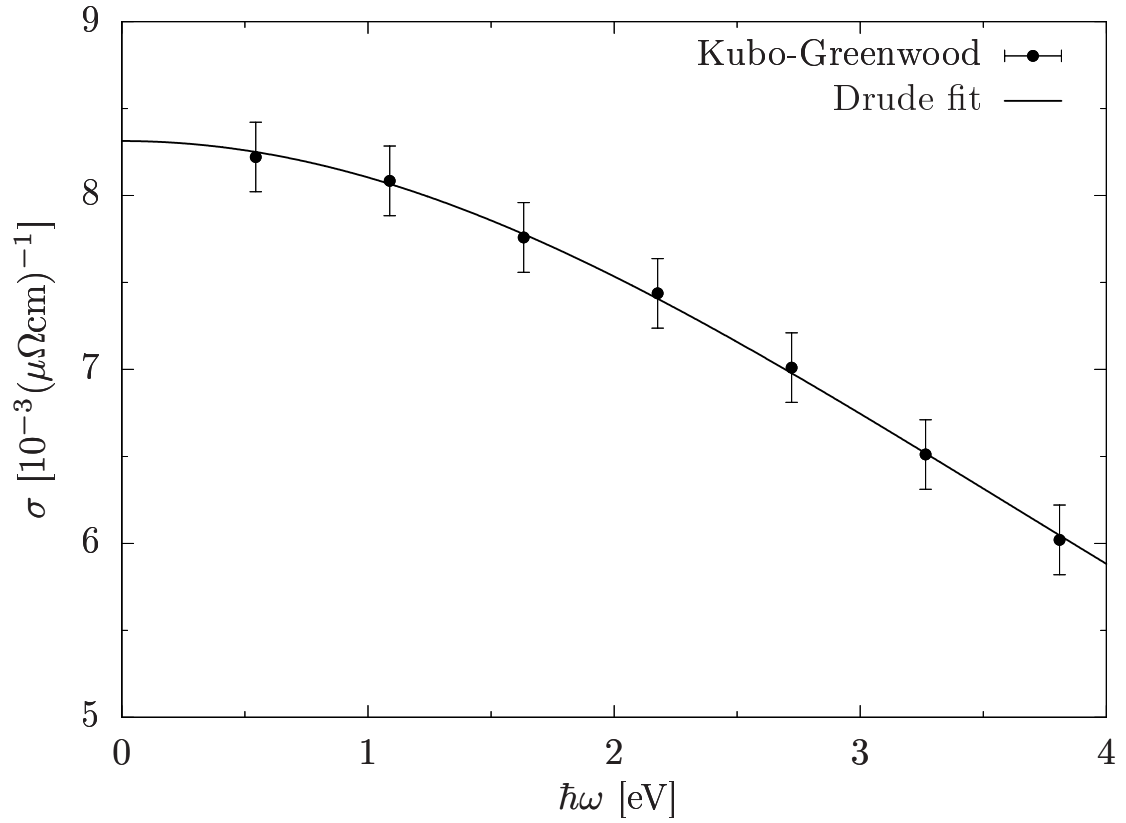


Figure 2.4: Optical conductivity of  $\text{Fe}_3\text{S}$  at near-ambient pressure from the Kubo-Greenwood equation with a Drude-fit to the data (modified from Wagle et al. [2018]).

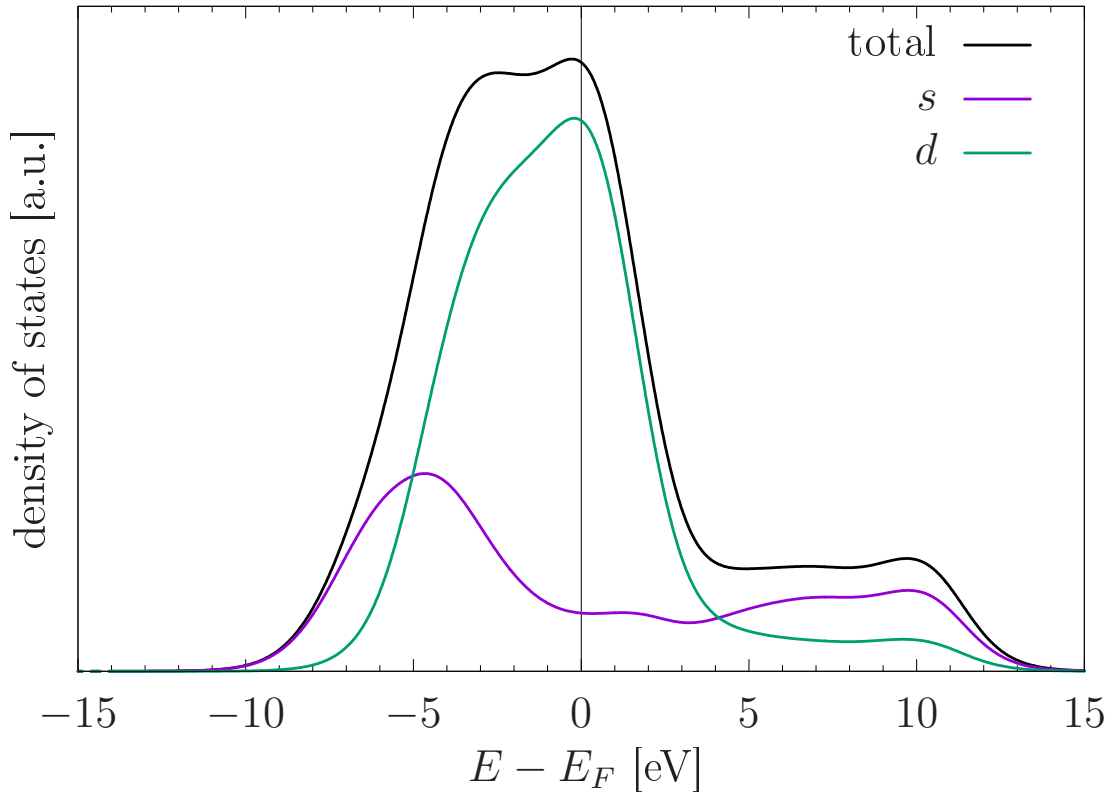


Figure 2.5: Site-projected density of states for liquid iron at near-ambient pressure.

1972]:  $d$ -electrons have a high density of states at the Fermi level  $N_d(E_F)$  (Figure 2.5), leading to a high probability for  $s$ - $d$ -scattering according to Fermi's golden rule, and

$$\rho \propto N_d(E_F), \quad (2.20)$$

as already considered by Stacey and Loper [2007] for resistivity models of iron at core conditions.

The effective mean free path is already short in highly resistive transition metals, and is expected to further decrease with the addition of impurities and compression. The presence of impurity atoms, such as the predominant light elements in the Earth's core Si, S and O, introduces an additional scattering mechanism, while compression merely increases the density of scattering centers.

If one assumes that electrons can only be scattered by phonons/ions, this trend can only continue down to the typical interatomic spacing in the system [Ioffe and Regel,

## 2 *Methods*

1960, Gunnarsson et al., 2003], causing resistivity to saturate. This concept has been well-established in the solid state physics community [e.g., Mooij, 1973] and recently adopted in resistivity models in the context of planetary cores [Gomi et al., 2013, 2016, Ohta et al., 2016]. As a consequence, the applicability of Matthiessen's rule for impurity resistivity and the Wiedemann-Franz law have been questioned.

## Bibliography

- I. Abarenkov and V. Heine. The model potential for positive ions. Philos. Mag., 12: 529–537, 1965. doi: 10.1080/14786436508218898.
- N. W. Ashcroft. Electron-ion pseudopotentials in metals. Phys. Lett., 23:48–50, 1966. doi: 10.1016/0031-9163(66)90251-4.
- N. W. Ashcroft and J. Lekner. Structure and resistivity of liquid metals. Phys. Rev., 145:83–90, 1966. doi: 10.1103/PhysRev.145.83.
- N. W. Ashcroft and N. D. Mermin. Solid State Physics. Saunders College, Philadelphia, 1976.
- G. V. Chester and A. Thellung. On the electrical conductivity of metals. Proc. Phys. Soc., 73:745–766, 1959. doi: 10.1088/0370-1328/73/5/308.
- N. de Koker, G. Steinle-Neumann, and V. Vlček. Electrical resistivity and thermal conductivity of liquid Fe alloys at high P and T, and heat flux in Earth’s core. Proc. Natl. Acad. Sci. USA, 109:4070–4073, 2012. doi: 10.1073/pnas.1111841109.
- P. Drude. Zur Elektronentheorie der Metalle. Ann. Phys., 306:566–613, 1900a. doi: 10.1002/andp.19003060312.
- P. Drude. Zur Elektronentheorie der Metalle; II. Teil. Galvanomagnetische und thermomagnetische Effecte. Ann. Phys., 308:369–402, 1900b. doi: 10.1002/andp.19003081102.
- J. Dufty, J. Wrighton, K. Luo, and S. B. Trickey. On the Kubo-Greenwood model for electron conductivity. Contrib. Plasma Phys., 58:150–154, 2018. doi: 10.1002/ctpp.201700102.
- R. Evans, D. A. Greenwood, and P. Lloyd. Calculations of the transport properties of liquid transition metals. Phys. Lett. A, 35:57–58, 1971. doi: 10.1016/0375-9601(71)90543-3.
- T. E. Faber and J. M. Ziman. A theory of the electrical properties of liquid metals, III. The resistivity of binary alloys. Philos. Mag., 11:153–173, 1965. doi: 10.1080/14786436508211931.
- R. P. Feynman. Forces in molecules. Phys. Rev., 56:340–343, 1939. doi: 10.1103/PhysRev.56.340.

## BIBLIOGRAPHY

- H. Gomi, K. Ohta, K. Hirose, S. Labrosse, R. Caracas, M. J. Verstraete, and J. W. Hernlund. The high conductivity of iron and thermal evolution of the Earth's core. Phys. Earth Planet. Inter., 224:88–103, 2013. doi: 10.1016/j.pepi.2013.07.010.
- H. Gomi, K. Hirose, H. Akai, and Y. Fei. Electrical resistivity of substitutionally disordered hcp Fe-Si and Fe-Ni alloys: Chemically-induced resistivity saturation in the Earth's core. Earth Planet. Sci. Lett., 451:51–61, 2016. doi: 10.1016/j.epsl.2016.07.011.
- X. Gonze. Dynamical matrices, Born effective charges, dielectric permittivity tensors, and interatomic force constants from density-functional perturbation theory. Phys. Rev. B, 55:10355–10368, 1997. doi: 10.1103/PhysRevB.55.10355.
- X. Gonze, B. Amadon, P.-M. Anglade, J.-M. Beuken, F. Bottin, P. Boulanger, F. Bruneval, D. Caliste, R. Caracas, M. Côté, T. Deutsch, L. Genovese, Ph. Ghosez, M. Giantomassi, S. Goedecker, D. R. Hamann, P. Hermet, F. Jollet, G. Jomard, S. Leroux, M. Mancini, S. Mazevet, M. J. T. Oliveira, G. Onida, Y. Pouillon, T. Rangel, G.-M. Rignanese, D. Sangalli, R. Shaltaf, M. Torrent, M. J. Verstraete, G. Zerah, and J. W. Zwanziger. Abinit: First-principles approach to material and nanosystem properties. Comput. Phys. Commun., 180:2582–2615, 2009. doi: 10.1016/j.cpc.2009.07.007.
- D. A. Greenwood. The Boltzmann equation in the theory of electrical conduction in metals. Proc. Phys. Soc., 71:585–596, 1958. doi: 10.1088/0370-1328/71/4/306.
- O. Gunnarsson, M. Calandra, and J. E. Han. Saturation of electrical resistivity. Rev. Mod. Phys., 75:1085–1099, 2003. doi: 10.1103/RevModPhys.75.1085.
- H.-J. Güntherodt, E. Hauser, H. U. Künzi, R. Evans, J. Evers, and E. Kaldis. Negative temperature coefficients of electrical resistivity: the divalent liquid metals Eu, Yb and Ba. J. Phys. F: Metal Phys., 6:1513–1522, 1976. doi: 10.1088/0305-4608/6/8/011.
- V. Heine and I. Abarenkov. A new method for the electronic structure of metals. Philos. Mag., 9:451–465, 1963. doi: 10.1080/14786436408222957.
- P. Hohenberg and W. Kohn. Inhomogeneous electron gas. Phys. Rev., 136:B864, 1964. doi: 10.1103/PhysRev.136.B864.
- A. F. Ioffe and A. R. Regel. Non-crystalline, amorphous and liquid electronic semiconductors. Prog. Semicond., 4:237–291, 1960.

- A. Jain and R. Evans. Calculation of the electrical resistivity of liquid iron in the Earth's core. Nature Physical Science, 235:165–167, 1971. doi: 10.1038/physci235165a0.
- R. O. Jones and O. Gunnarsson. The density functional formalism, its applications and prospects. Rev. Mod. Phys., 61:689–746, 1989. doi: doi.org/10.1103/RevModPhys.61.689.
- W. Kohn and L. J. Sham. Self-consistent equations including exchange and correlation effects. Phys. Rev., 140:A1133, 1965. doi: 10.1103/PhysRev.140.A1133.
- G. Kresse and J. Furthmüller. Efficiency of ab-initio total energy calculations for metals and semiconductors using a plane-wave basis set. Comput. Mat. Sci., 6:15–50, 1996a. doi: 10.1016/0927-0256(96)00008-0.
- G. Kresse and J. Furthmüller. Efficient iterative schemes for ab initio total-energy calculations using a plane-wave basis set. Phys. Rev. B, 54:11169–11186, 1996b. doi: 10.1103/PhysRevB.54.11169.
- G. Kresse and J. Hafner. Ab initio molecular dynamics for liquid metals. Phys. Rev. B, 47:558–561, 1993. doi: 10.1103/PhysRevB.47.558.
- G. Kresse and D. Joubert. From ultrasoft pseudopotentials to the projector augmented-wave method. Phys. Rev., 59:1758–1775, 1999. doi: 10.1103/PhysRevB.59.1758.
- R. Kubo. Statistical mechanical theory of irreversible processes. I. General theory and simple applications to magnetic and conduction problems. J. Phys. Soc. Jpn., 12: 570–586, 1957. doi: 10.1143/JPSJ.12.570.
- N. H. March. Liquid Metals: Concepts and Theory. Cambridge University Press, Cambridge, 1990.
- J. H. Mooij. Electrical conduction in concentrated disordered transition metal alloys. Phys. Stat. Sol. A, 17:521–530, 1973. doi: 10.1002/pssa.2210170217.
- N. F. Mott. The electrical resistivity of liquid transition metals. Philos. Mag., 26: 1249–1261, 1972. doi: 10.1080/14786437208220339.
- S. Nosé. A unified formulation of the constant temperature molecular dynamics methods. J. Chem. Phys., 81:511–519, 1984. doi: 10.1063/1.447334.

## BIBLIOGRAPHY

- K. Ohta, Y. Kuwayama, K. Hirose, K. Shimizu, and Y. Ohishi. Experimental determination of the electrical resistivity of iron at Earth's core conditions. Nature, 534: 95–98, 2016. doi: 10.1038/nature17957.
- L. S. Ornstein and F. Zernike. Integral equation in liquid state theory. Proc. Acad. Sci. Amsterdam, 17:793, 1914.
- V. Ozoliņš and M. Körling. Full-potential calculations using the generalized gradient approximation: Structural properties of transition metals. Phys. Rev. B, 48:18304–18307, 1993. doi: 10.1103/PhysRevB.48.18304.
- J. K. Percus and G. J. Yevick. Analysis of classical statistical mechanics by means of collective coordinates. Phys. Rev., 110:1–13, 1958. doi: 10.1103/PhysRev.110.1.
- J. P. Perdew, J. A. Chevary, S. H. Vosko, K. A. Jackson, M. R. Pederson, D. J. Singh, and C. Fiolhais. Atoms, molecules, solids, and surfaces: Applications of the generalized gradient approximation for exchange and correlation. Phys. Rev. B, 46: 6671–6687, 1993. doi: 10.1103/PhysRevB.46.6671.
- J. P. Perdew, K. Burke, and M. Ernzerhof. Generalized gradient approximation made simple. Phys. Rev. Lett., 77:3865–3868, 1996. doi: 10.1103/PhysRevLett.77.3865.
- V. Recoules and J. P. Crocombette. Ab initio determination of electrical and thermal conductivity of liquid aluminum. Phys. Rev. B, 72:104202, 2005. doi: 10.1103/PhysRevB.72.104202.
- A. Sommerfeld. Zur Elektronentheorie der Metalle auf Grund der Fermischen Statistik. Z. Phys., 47:1–32, 1928. doi: 10.1007/BF01391052.
- F. D. Stacey and D. E. Loper. A revised estimate of the conductivity of iron alloy at high pressure and implications for the core energy balance. Phys. Earth Planet. Inter., 161:13–18, 2007. doi: 10.1016/j.pepi.2006.12.001.
- L. Stixrude, R. E. Cohen, and D. J. Singh. Iron at high pressure: Linearized-augmented-plane-wave computations in the generalized-gradient approximation. Phys. Rev. B, 50:6442–6445, 1994. doi: 10.1103/PhysRevB.50.6442.
- M. Torrent, F. Jollet, F. Bottin, G. Zérah, and X. Gonze. Implementation of the projector augmented-wave method in the abinit code: Application to the study of iron under pressure. Comput. Mater. Sci., 42:337–351, 2008. doi: 10.1016/j.commatsci.2007.07.020.

- F. Wagle, G. Steinle-Neumann, and N. de Koker. Saturation and negative temperature coefficient of electrical resistivity in liquid iron-sulfur alloys at high densities from first principles calculations. Phys. Rev. B, 97:094307, 2018. doi: 10.1103/PhysRevB.97.094307.
- M. S. Wertheim. Exact solution of the Percus-Yevick integral equation for hard spheres. Phys. Rev. Lett., 10:321–323, 1963. doi: 10.1103/PhysRevLett.10.321.
- J. M. Ziman. A theory of the electrical properties of liquid metals. I: The monovalent metals. Philos. Mag., 6:1013–1034, 1961. doi: 10.1080/14786436108243361.



### 3 Synopsis and scope of the thesis

Until a few years ago, the accurate determination of electrical resistivity at elevated pressure ( $P$ ) had been limited to conditions accessible with the large volume press [Secco and Schlössin, 1989] or along the shock Hugoniot [Keeler, 1971, Matassov, 1977]. Recent years have seen substantial technological advances in the field of high pressure research, both in experiments and computations: Resistivity calculations for liquids within the DFT-MD framework require large supercells containing  $>100$  atoms, which has routinely become feasible using state-of-the-art supercomputers, and theoretical and algorithmic developments [Burke, 2012, Beck, 2000, Román-Pérez and Soler, 2009]. The first of those studies on electrical and thermal conductivity of liquid iron alloys predicted values much higher than previously assumed at conditions of the Earth's core, challenging the traditional view of a purely thermally driven dynamo. While first principle studies consistently find thermal conductivity values above  $140 \text{ Wm}^{-1}\text{K}^{-1}$  depending on the composition [de Koker et al., 2012, Pozzo et al., 2012, 2013], traditional theoretical estimates, based on a pressure-dependent model for electrical resistivity and the Wiedemann-Franz law, yielded less than half of those values [Stacey and Anderson, 2001, Stacey and Loper, 2007]. Static compression at similar conditions can only be generated in a diamond anvil cell (DAC), with the sample size restricted to a few tens to a hundred microns. Although novel sample preparation techniques have made static resistivity measurements feasible up to the megabar regime [Gomi et al., 2013, Seagle et al., 2013], heating above the melting temperature of iron remains extremely challenging in high  $P$  experiments and there are only few data on liquids. Some recent studies have attributed the high electrical conductivity to resistivity saturation, and used the concept for extrapolating DAC experiments to high  $T$ , where they found values consistent with the predictions by first principles computations [Gomi et al., 2013, Seagle et al., 2013, Ohta et al., 2016].

As the spatial arrangement of atomic scattering potentials in a liquid is closely related to electrical resistivity [Ziman, 1961] (see Section 2.3.2), knowledge of the struc-

### 3 Synopsis

ture can provide some insight into electronic transport properties. Radial distribution functions  $g(r)$  and structure factors  $S(q)$  are easily accessible by post-processing of DFT-MD trajectories. Even for cells containing  $\sim 100$  atoms, this does not require very long simulation time (Section 2.1): About 1000 MD steps yield sufficiently good statistics for smooth histograms. If adequate pair potentials are used<sup>1</sup>, the comparatively unlimited cell size in classical MD may open new perspectives for understanding the structure of multi-component alloys, even at extreme conditions. Time-resolved information on atomistic mechanisms and structural properties is beyond the reach of traditional experimental diffraction methods and can only be provided by free electron laser facilities with sub-nanometer resolution, such as the European XFEL in Hamburg [Tschentscher et al., 2017].

The aim of the work presented in this thesis is to use DFT-MD results and theoretical considerations to investigate the relationship between electrical resistivity and structure of iron alloys at planetary core conditions. We examine the effect of the geophysically relevant light elements Si, O and S (Section 3.1) on electrical resistivity and explicitly show for the first time that the Ioffe-Regel condition for resistivity saturation (Section 2.3.4) is satisfied for high concentrations of Si and S at high  $P$  and  $T$ . In the saturation limit, Fe-S alloys exhibit a unique decrease of resistivity with temperature, which we explain in terms of the electronic structure (Section 3.2). Finally, we quantify the resistivity discontinuity of iron upon melting and infer resistivity of solid iron along the melting curve (Section 3.3).

---

<sup>1</sup>As part of a side project, I fitted forces from DFT-MD snapshots of one  $P/T$  condition in order to generate pair potentials within the embedded-atom-method, to be used in the force field code LAMMPS.  $S(q)$  at very different  $P/T$  conditions were reproduced very well by corresponding simulations performed in LAMMPS, with up to  $10^6$  atoms. In addition to computational efficiency and better statistics, the more accurate representation of the long wavelength limit of  $S(q)$  is one of the major benefits.

## 3.1 Resistivity saturation in liquid iron–light-element-alloys

*This section summarizes the following published paper included in Appendix 4:*

*F. Wagle, G. Steinle-Neumann & N. de Koker (2018), Resistivity saturation in liquid iron–light-element-alloys at conditions of planetary cores from first principles computations, C. R. Geosci. (in press).*

*I analyzed previously published DFT-MD trajectories and resistivity results with respect to structure-property relations for resistivity, and wrote a first draft of the manuscript.*

This work is based on published results for electrical resistivity in liquid Fe, Fe-Si, Fe-O [de Koker et al., 2012] and Fe-S [Wagle et al., 2018] alloys. It provides an overview over these results, explores their relation to structural properties of the binary liquid alloys studied and puts them into a geophysical context.

With the addition of impurities to a metal, resistivity generally increases. They serve as an additional source of electron scattering, which reduces the electron mean free path as a function of their concentration. Although impurity resistivities are additive in many cases (Matthiessen’s rule, see Section 2.3.4), this behavior has been shown to break down if the system is close to saturation [Gomi et al., 2016].

While pure iron and Fe-O alloys retain a positive temperature coefficient of resistivity (TCR) in the compression range studied, alloys with high concentrations of silicon or sulfur exhibit constant resistivity, or even a negative TCR at high compression (Figure 3.1). The decrease of the TCR is a consequence of resistivity saturation due to compression and increasing impurity concentration, which we show by explicitly calculating the electron mean free path (Section 2.3.1) and comparing it to the mean interatomic distance. For Fe<sub>3</sub>S and Fe<sub>3</sub>Si at the highest compression, the mean free path becomes equal to the interatomic distance, known as the Ioffe-Regel limit [Ioffe and Regel, 1960]. This indicates a state of saturation, in which increasing  $T$  does not lead to higher resistivity. The origin of the negative TCR observed in Fe-S alloys has been explained in a separate paper (Section 3.2).

### 3 Synopsis

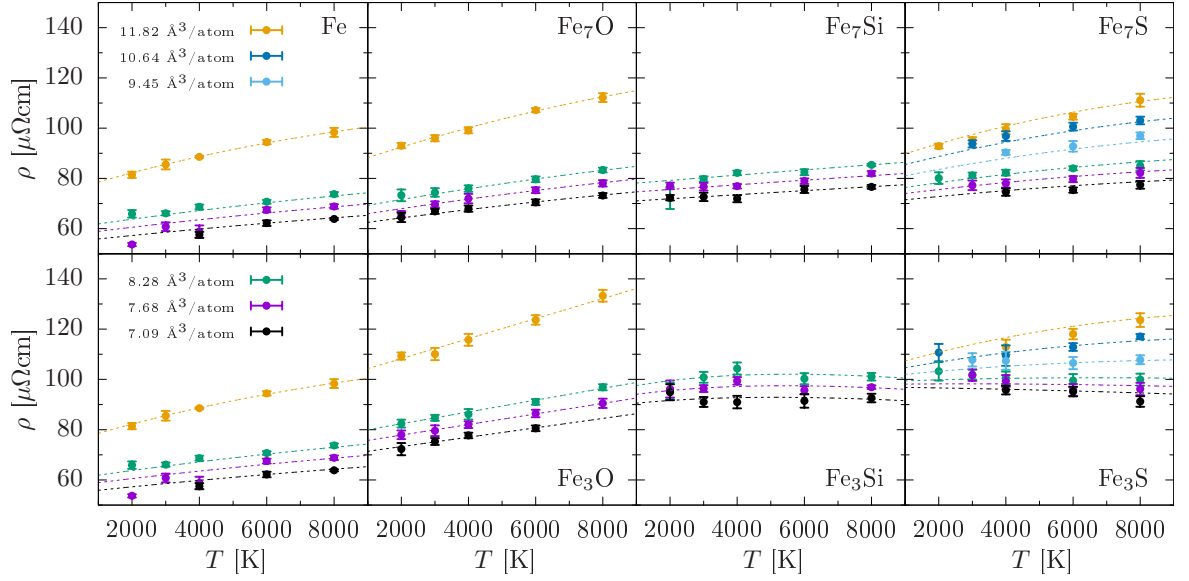


Figure 3.1: Electrical resistivity of liquid iron and various binary iron alloys as a function of temperature along isochores. The resistivity model fit for  $\rho(V, T)$  (Equation 3.1) is shown by dashed lines.

The spatial arrangement of atoms is crucial for electronic transport properties and differs significantly between the liquid alloys studied:

- Based on the evaluation of nearest-neighbor peaks in  $g_{\alpha\beta}(r)$ , interaction radii of silicon and iron are very similar. Silicon therefore incorporates well into the liquid structure, randomly substituting for iron atoms. Fe-Fe and Fe-Si coordination numbers equally increase slightly with compression.
- Sulfur has a slightly smaller interaction radius than iron and exhibits interstitial-like incorporation at low  $P$ . Fe-S bonds have been shown to strengthen with increasing  $P$  [Alfè and Gillan, 1998], which results in an increasing Fe-S coordination number. This can be observed directly by the virtual absence of a nearest-neighbor peak in  $g_{SS}(r)$  at high compression, indicating an effective S-S repulsion.
- Oxygen has a much smaller interaction radius than iron. The low Fe-O coordination number shows that oxygen occupies interstitial-like sites in liquid iron and it increases slightly with  $P$ . Oxygen incorporation remains interstitial even at pressures of the Earth's inner core.

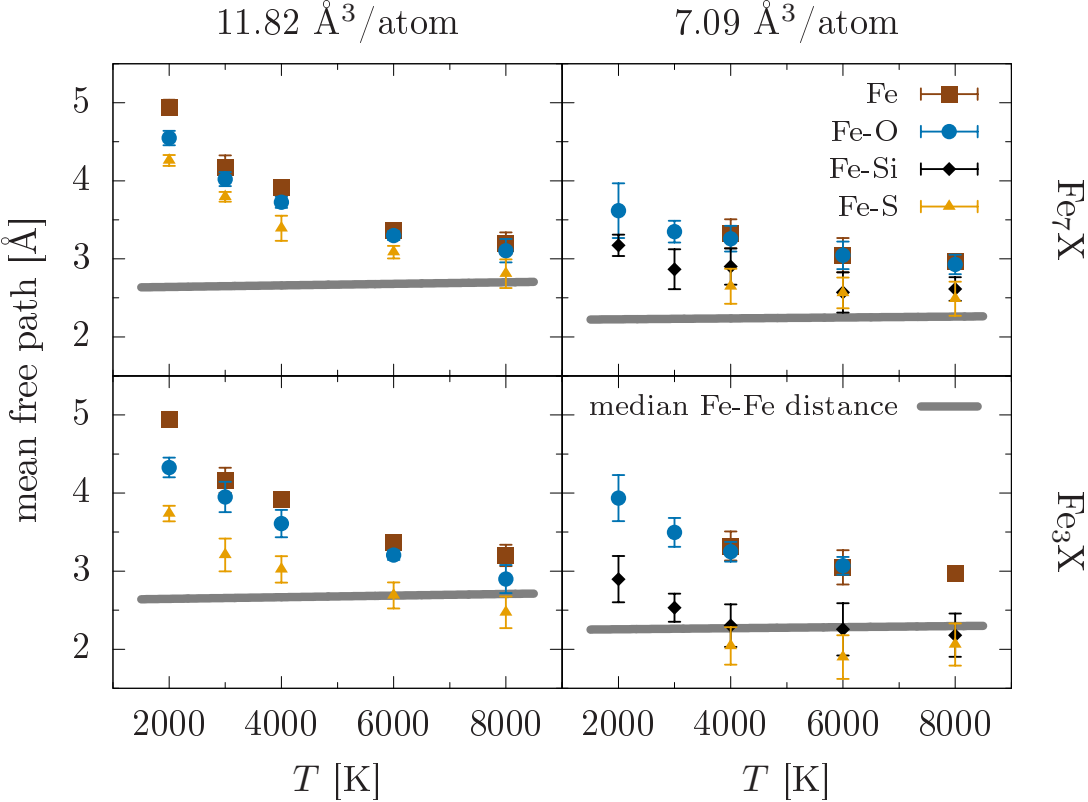


Figure 3.2: Electron mean free path for liquid iron with 12.5 at.% (top) and 25 at.% (bottom) light element content for two cell volumes, near ambient  $P$  (left) and largest compression (right), obtained by a Drude-fit to optical conductivity. The mean free path approaches the interatomic Fe-Fe distance in the alloys (median, thick gray lines) with increasing temperature, compression and impurity concentration. For  $\text{Fe}_3\text{Si}$  and  $\text{Fe}_3\text{S}$  at the smallest cell volume, the Ioffe-Regel condition is satisfied.

### 3 Synopsis

Resistivity saturation is more efficiently triggered by silicon and sulfur than by oxygen (Figure 3.2), consistent with the classical theory of electron scattering: Impurity atoms with large cross-sections lead to a high scattering probability and to a shorter mean free path than smaller atoms. A possible reason why the negative TCR—and the high degree of saturation necessary for its observation—occurs only in the Fe-S system, is a smaller overlap of impurity scattering cross sections due to the effective S-S repulsion.

We conclude that saturation is a dominant effect at high  $P$ , limiting resistivity to  $\sim 100 \mu\Omega\text{cm}$  at conditions of the Earth's core. Resistivity profiles along adiabats are independent of  $T$  and the evolution of a planetary dynamo is therefore not influenced by the resistivity profile changing over time.

## 3.2 Negative temperature coefficient of resistivity in liquid iron–sulfur alloys

*This section summarizes the following published paper included in Chapter 5:*

*F. Wagle, G. Steinle-Neumann & N. de Koker (2018), Saturation and negative temperature coefficient of electrical resistivity in liquid iron-sulfur alloys at high densities from first principles calculations, Phys. Rev. B **97**, 094307.*

*I performed DFT-MD and linear response calculations at conditions previously not investigated, analyzed the results in terms of transport properties, electron mean free path and density of states, developed the resistivity model and wrote a first draft of the manuscript.*

Focus of this work is to investigate the influence of sulfur on electronic transport properties of liquid iron, describe saturation mechanisms of electrical resistivity based on first principles computations, and identify the reason for the negative TCR described in Section 3.1.

Using DFT-MD over a wide  $P$ - $T$  range, we produce representative configurations of liquid Fe-S alloys and calculate electrical resistivity and thermal conductivity with the Kubo-Greenwood formula. By fitting optical conductivity from the Kubo-Greenwood results, we explicitly calculate an average electron mean free path for all  $P/T$  conditions. The mean free path decreases with increasing  $T$ , compression and sulfur concentration and asymptotically approaches the interatomic distance (Figure 3.2). In the case of pure electron-ion scattering, this sets a lower boundary for the electron mean free path, and is referred to as the Ioffe-Regel condition as discussed in Section 3.1.

In order to understand the complexity of resistivity behavior shown in Figure 3.1, one has to consider the electronic structure of iron and its alloys (see Section 2.3.4). Most of the electric current in  $3d$  transition metals is carried by  $s$ -electrons. As  $d$ -electrons have a high density of states (DOS) at the Fermi level and a comparatively low Fermi velocity, resistivity is dominated by  $s$ - $d$  scattering. Fermi's golden rule implies that resistivity is proportional to the  $d$ -electron density of states at the Fermi level [Mott, 1972], giving rise to two effects:

### 3 Synopsis

- The  $d$ -DOS at the Fermi level drops substantially with increasing compression (Figure 3.3a). This effect of band dispersion due to stronger interactions between atoms is well known [Cohen et al., 1997], resulting in the observed resistivity decrease in iron alloys upon compression.
- Broadening of the DOS with increasing  $T$  (Figure 3.3b) is less pronounced and reflects dynamic changes of the short range order in the liquid. A larger amount of thermal energy in the system allows for shorter interatomic distances, that are also expressed by thermal pressure [Hunt et al., 2003]. As a consequence of the corresponding decrease of  $N_d(E_F)$ , resistivity decreases with increasing  $T$ . Since this is a secondary effect in comparison to the increase of vibrational amplitudes with  $T$ , the negative TCR is only noticeable once resistivity has saturated.

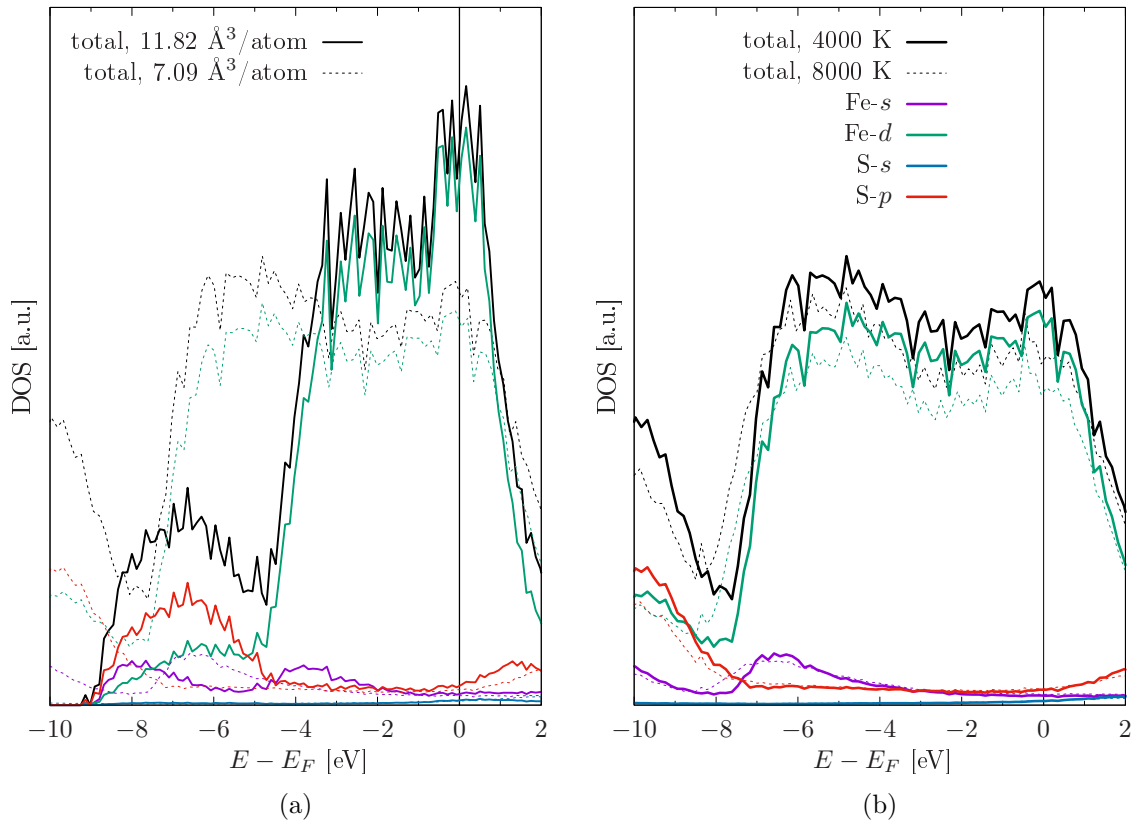


Figure 3.3: (a) Broadening of site- and angular momentum-projected electron densities of states for  $\text{Fe}_3\text{S}$  at 4000 K with decreasing cell volume. (b) Broadening of site- and angular momentum-projected electron densities of states with increasing  $T$  (4000 K and 8000 K) for  $\text{Fe}_3\text{S}$  at a cell volume of  $7.09 \text{ \AA}^3/\text{atom}$ .

### 3.2 Negative temperature coefficient of resistivity

These observations lead us to revise the Bloch-Grüneisen-based resistivity model of de Koker et al. [2012] in order to account for both saturation and the negative TCR explicitly. We describe the resistivity behavior  $\rho(V, T)$  by a parallel resistor model:

$$\frac{1}{\rho(V, T)} = \frac{1}{\rho_{\text{BG}}(V, T)} + \frac{1}{\rho_{\text{sat}}(V)} + \frac{1}{\rho_{\text{el}}(T)}, \quad (3.1)$$

where

$$\rho_{\text{BG}} = \rho_0 \left(\frac{V}{V_0}\right)^a + \rho_1 \left(\frac{V}{V_0}\right)^b \frac{T}{T_0} \quad (3.2)$$

is the empirical expression used by de Koker et al. [2012] based on the Bloch-Grüneisen formula.

$$\rho_{\text{sat}} = c \left(\frac{V}{V_0}\right)^{\frac{1}{3}} \quad (3.3)$$

is a term accounting for resistivity saturation proportional to the interatomic distance and

$$\rho_{\text{el}} = d \frac{T_0}{T} \quad (3.4)$$

describes the effect of thermal broadening of the DOS proportional to inverse temperature.

By transforming our results into  $P/T$ -space using an equation-of-state-fit for our MD results [de Koker and Stixrude, 2009, Vlček et al., 2012], we find that resistivity saturates at approximately constant  $100 \mu\Omega\text{cm}$  across the Earth's entire OC (Figure 3.4). This is substantially higher than extrapolated estimates by Suehiro et al. [2017], based on ambient  $T$  experiments on the ternary Fe-Si-S system. Using Matthiessen's rule and previous experimental results for the Fe-Si system [Gomi et al., 2013, 2016], they find impurity resistivity of sulfur to be significantly less than that of silicon, contrarily to our results. This discrepancy might stem from the violation of Matthiessen's rule in the limit of resistivity saturation [Gomi et al., 2016].

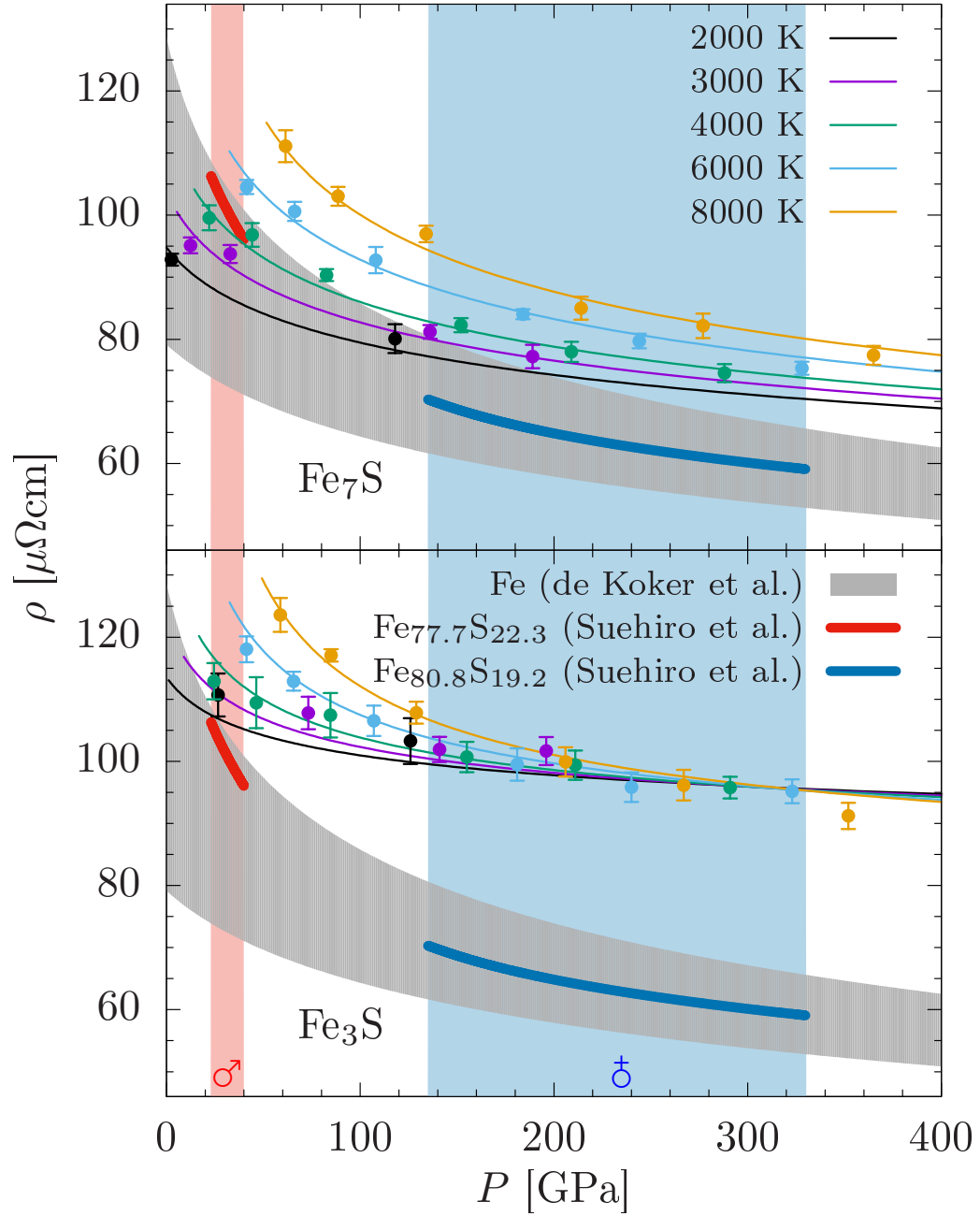


Figure 3.4: Electrical resistivity of liquid Fe–S alloys as a function of pressure for  $\text{Fe}_7\text{S}$  (top) and  $\text{Fe}_3\text{S}$  (bottom). Solid lines are best fits of a parallel resistor model to  $\rho(V, T)$  (equation 3.1) converted from  $V$ - $T$  to  $P$ - $T$  conditions using an equation of state fit. Results from an experimental study [Suehiro et al., 2017] along a model areotherm (red line) and geotherm (blue line) as well as computational results for pure Fe [de Koker et al., 2012] between 2000 and 8000 K (gray area) are included for comparison.

### 3.3 Resistivity of solid iron at inner core boundary conditions

*This section summarizes the following published paper included in Chapter 6:*

*F. Wagle & G. Steinle-Neumann (2018), Resistivity discontinuity of iron along the melting curve, Geophys. J. Int. **213**, 237–243.*

*I compiled experimental data, reformulated Ziman’s approximation to account for the density dependence, and wrote a first draft of the manuscript.*

As a consequence of the transition from a crystalline to an amorphous structure, electrical resistivity of metals generally increases upon melting. This discontinuity has been observed for many metals at ambient  $P$  (for a comprehensive study see Rosenfeld and Stott [1990]) and constitutes  $\sim 8\%$  for iron. A large volume press experiment by Secco and Schlössin [1989], a recent DAC experiment by Ohta et al. [2016] and computational studies by Pozzo et al. [2012, 2014] have shown that the resistivity jump on melting persists up to conditions of the Earth’s core. In describing resistivity of liquid iron at core conditions, experimental high pressure studies on  $\epsilon$ -Fe have either neglected the resistivity jump [Gomi et al., 2013] or assumed it to be as large as 20% [Ohta et al., 2016].

Aim of this study was to test the validity of Ziman’s approximation (see Section 2.3.2),

$$\frac{\rho_{\text{el}}^{\text{liquid}}}{\rho_{\text{el}}^{\text{solid}}} \left( \frac{\varrho^{\text{liquid}}}{\varrho^{\text{solid}}} \right)^2 \left( \frac{\beta_T^{\text{liquid}}}{\beta_T^{\text{solid}}} \right)^{-1} \simeq 1, \quad (3.5)$$

on iron at ambient  $P$  and estimate resistivity in the solid ( $\rho_{\text{el}}^{\text{solid}}$ ), based on resistivity in the liquid ( $\rho_{\text{el}}^{\text{liquid}}$ ), and densities ( $\varrho$ ) and isothermal compressibilities ( $\beta_T$ ) from a thermodynamic model.

Experimental data for resistivity, density and compressibility of a variety of metals were compiled just above and below the melting point at ambient  $P$  in order to calculate the left hand side of Equation (3.5). The conversion of sound velocity measurements (which yield adiabatic elastic properties) to isothermal compressibility is very sensitive with respect to the choice of thermal expansivity  $\alpha$ . For liquid iron, the value of  $\alpha$  has been topic of some debate over systematic errors occurring in different methods of measurement [Nasch and Steinemann, 1995, Williams, 2009], yielding values below

### 3 Synopsis

Table 3.1: Thermophysical data for pure iron at ambient pressure at the melting point ( $T_m = 1808 \pm 5$  K)<sup>a</sup>. Resistivities have been measured by Cezairliyan and McClure [1974]<sup>a</sup> and van Zytveld [1980]<sup>b</sup>. If not reported directly, values measured by Dever [1972]<sup>c</sup>, Basinski et al. [1955]<sup>d</sup>, Tsu et al. [1985]<sup>e</sup>, Drotning [1981]<sup>f</sup> and compiled by Desai [1986]<sup>g</sup> have been extrapolated to  $T_m$  while using the misfit as uncertainty. For the liquid phase, a scenario including values for  $\rho$  and  $\alpha$  from Assael et al. [2006]<sup>h</sup> has been tabulated for comparison. A column of properties for liquid Fe from the thermodynamic model of Komabayashi [2014] has been included.

	$\delta$ -Fe	liquid Fe		
		Drotning	Assael	Komabayashi
$\rho_{el}$ [ $\mu\Omega\text{cm}$ ]	$127.0 \pm 0.6^a$		$137.6 \pm 1.0^b$	
$v_p$ [ $\text{km s}^{-1}$ ]	$4.73 \pm 0.07^c$	$3.98 \pm 0.03^e$		3.98
$v_s$ [ $\text{km s}^{-1}$ ]	$2.49 \pm 0.06^c$			
$\rho$ [ $\text{g cm}^{-3}$ ]	$7.29 \pm 0.02^d$	$7.017 \pm 0.002^f$	$7.04 \pm 0.06^h$	7.09
$\alpha$ [ $10^{-5}\text{K}^{-1}$ ]	$6.5 \pm 0.1^d$	$8.8 \pm 0.1^f$	$13.2 \pm 0.1^h$	9.0
$c_p$ [ $\text{J g}^{-1}\text{K}^{-1}$ ]	$0.80 \pm 0.06^a$		$0.84 \pm 0.05^g$	0.82
$\beta_S$ [ $\text{GPa}^{-1}$ ]	$1/(103 \pm 6)$	$1/(111 \pm 2)$	$1/(112 \pm 2)$	1/112
$\beta_T$ [ $\text{GPa}^{-1}$ ]	$1/(91 \pm 5)$	$1/(88 \pm 2)$	$1/(70 \pm 2)$	1/87
$\frac{\rho_{el}^{\text{liquid}}}{\rho_{el}^{\text{solid}}} \left( \frac{\rho^{\text{liquid}}}{\rho^{\text{solid}}} \right)^2 \left( \frac{\beta_T^{\text{liquid}}}{\beta_T^{\text{solid}}} \right)^{-1}$		$0.97 \pm 0.05$	$0.78 \pm 0.05$	$0.98 \pm 0.05$

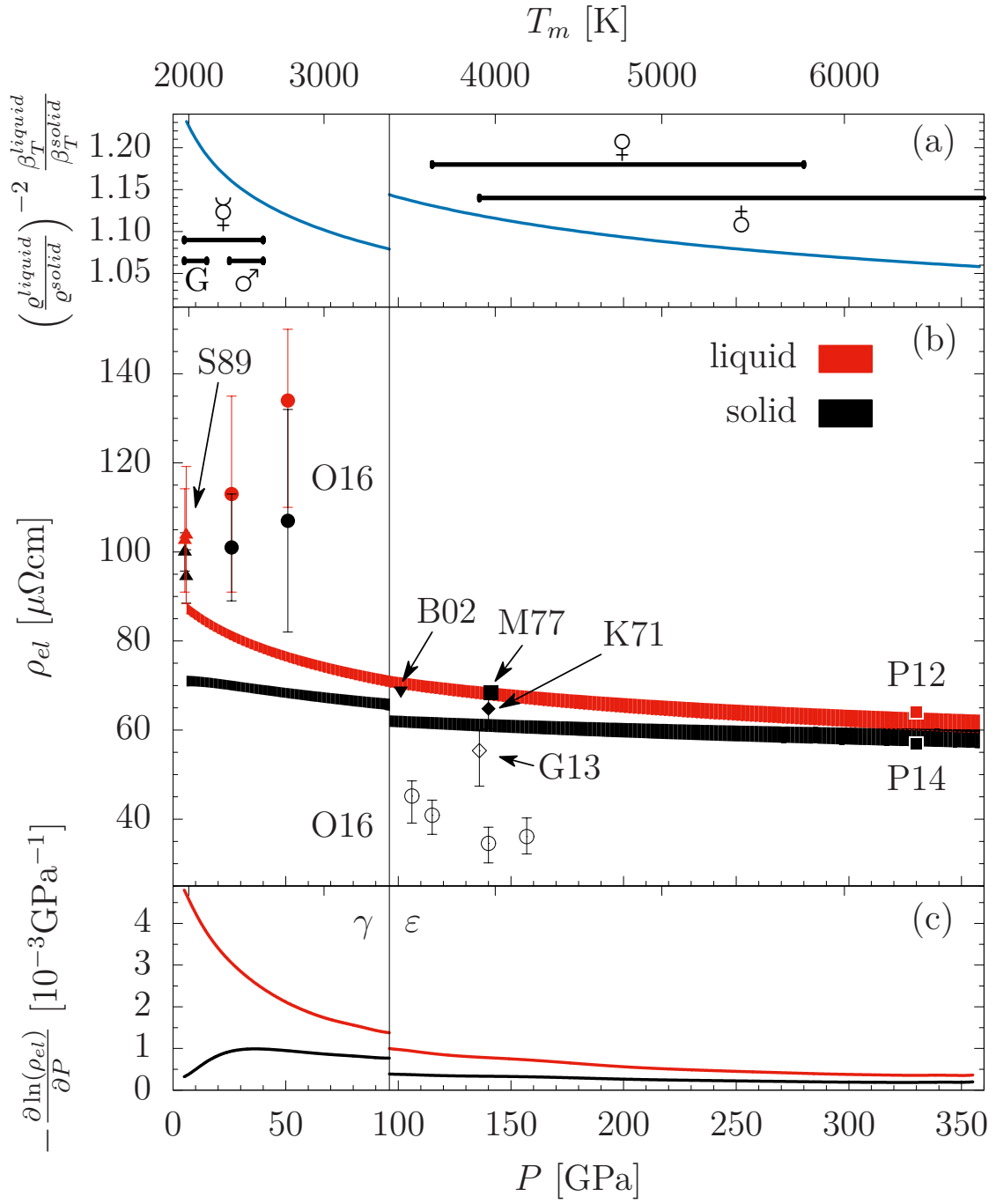
$9 \cdot 10^{-5} \text{ K}^{-1}$  (widely accepted by the geophysical community) or above  $11 \cdot 10^{-5} \text{ K}^{-1}$  (NIST recommended value [Assael et al., 2006]). As the difference between those values have a large effect on Equation (3.5), we chose an alternative way for determining  $\beta_T$ , independent of the experiments previously discussed: Based on long wavelength extrapolations of experimentally determined liquid structure factors [Waseda and Ohtani, 1974], we find values consistent with the thermodynamic model we use for  $\rho$  and  $\beta_T$  along the melting curve (Table 3.1).

We observe that Equation (3.5) is satisfied for simple metals (Na and Al, see Table S3 in Chapter 6) and transition metals with partially filled  $d$ -bands (Fe, Co and Ni, see Table S4 in Chapter 6), while it does not hold for noble metals (Cu, Ag and Au, see Table S5 in Chapter 6). Assuming the validity of Equation (3.5) for iron at high  $P$ , we use the model fit for  $\rho_{el}^{\text{liquid}}$  by de Koker et al. [2012], and  $\rho$  and  $\beta_T$  from the thermodynamic model of Komabayashi [2014] and calculate  $\rho_{el}^{\text{solid}}$  along the melting curve of iron. As density and compressibility in liquid and solid iron become more similar with increasing  $P$ , the discontinuity at inner core boundary (ICB) conditions is found to become negligible ( $\sim 7\%$ , see Figure 3.5). However, this might depend on the stable phase in

the inner core: Based on experiments [Tateno et al., 2010, Anzellini et al., 2013] and a first principles study by Godwal et al. [2015], we assumed hexagonal-close-packed iron to be in equilibrium with the liquid at ICB conditions. This has been questioned most recently by a computational study, showing a dynamically stabilized body-centered-cubic phase using DFT-MD in a large simulation cell [Belonoshko et al., 2017]. Testing the influence of this possible phase on the resistivity discontinuity predicted by Ziman’s approximation would require an accurate equation of state, which is not available to date.

Considerations based on Ziman’s theory and approximation can also serve as a predictive tool for estimating electrical resistivity in the liquid, which is still challenging to measure at high  $P$ , and provide a physically-based alternative to using *ad hoc* values as in [Ohta et al., 2016].

While the influence of a conducting inner core on the geodynamo is still under debate [Wicht, 2002, Dharmaraj and Stanley, 2012, Lhuillier et al., 2013], significant changes of magnetic boundary conditions at the ICB can only be achieved if one assumes a large difference in chemical composition due to partitioning of light elements between liquid and solid portions of the core. Since silicon and sulfur—the elements with the largest influence on resistivity—nearly equally partition between solid and liquid iron at conditions of the Earth’s ICB [Alfè et al., 2002], this scenario is highly unlikely.



---

Figure 3.5 (preceding page): (a) Liquid to solid compressibility/density ratio for Fe along the melting curve from the thermodynamic model of Komabayashi [2014] used in our evaluation of Ziman’s approximation. The lower  $x$ -axis label and ticks show pressure, the upper ones the corresponding melting temperature. Pressure intervals indicated correspond to core  $P$  in the terrestrial bodies of our solar system (Ganymede, Mercury, Mars, Venus and Earth). The vertical line represents the  $\gamma$ - $\varepsilon$ -liquid triple point in the model of Komabayashi [2014] (96 GPa and 3300 K). (b) Electrical resistivities in the liquid (red curve) and the solid (black curve) phases of Fe along the melting curve. For the liquid phase, the modified Bloch-Grüneisen fit from de Koker et al. [2012] has been evaluated along the melting curve, while the resistivity in the solid has been calculated using the ratios shown in panel (a) and applying Equation (3.5). The band widths take fitting uncertainties of the original Kubo-Greenwood results by de Koker et al. [2012] into account. Laboratory data (filled symbols) are by Secco and Schlössin [1989] (S89) and Ohta et al. [2016] (O16) from static experiments, and by Bi et al. [2002] (B02), Keeler [1971] (K71) and Matassov [1977] (M77) from shock wave experiments. For  $\rho_{\text{el}}^{\text{liquid}}$  and  $\rho_{\text{el}}^{\text{solid}}$ , data by Secco and Schlössin [1989] and Ohta et al. [2016] up to 51 GPa have been fitted linearly in the liquid and solid regions, respectively, and extrapolated towards  $T_m$  from both sides (see Chapter 6). For the shock wave experiments, the lowest  $P$  point by Bi et al. [2002] and the highest  $P$  point each by Keeler [1971] and Matassov [1977] have been used, all for the solid phase. Temperatures along the Hugoniot at these pressures are significantly below melting [Brown and McQueen, 1986]. Open circles in the  $P$ -range between 100 and 160 GPa show values calculated from combined Bloch-Grüneisen/resistivity-saturation fit parameters given in Ohta et al. [2016] and evaluated at  $T_m$  of Komabayashi [2014]. G13 (open diamond) represents the high  $T$  extrapolation of a room temperature DAC experiment reported in Gomi et al. [2013]. At inner core boundary  $P$ , the Kubo-Greenwood results by Pozzo et al. [2012, 2014] (P12 and P14) are included for liquid and solid Fe, respectively. (c) Negative logarithmic derivative  $-\partial(\ln \rho_{\text{el}})/\partial P$  for liquid and solid iron along its melting curve. While the  $P$ -gradient is significant in the liquid, it is negligible in the solid, particularly for  $\varepsilon$ -Fe.

## Bibliography

- D. Alfè and M. J. Gillan. First-principles simulations of liquid Fe-S under Earth's core conditions. Phys. Rev. B, 58:8248–8256, 1998. doi: 10.1103/PhysRevB.58.8248.
- D. Alfè, M. J. Gillan, and G. D. Price. Composition and temperature of the Earth's core constrained by combining ab initio calculations and seismic data. Earth Planet. Sci. Lett., 195:91–98, 2002. doi: 10.1016/S0012-821X(01)00568-4.
- S. Anzellini, A. Dewaele, M. Mezouar, P. Loubeyre, and G. Morard. Melting of iron at Earth's inner core boundary based on fast X-ray diffraction. Science, 340:464–466, 2013. doi: 10.1126/science.1233514.
- M. J. Assael, K. Kakosimos, R. M. Banish, J. Brillo, I. Egry, R. Brooks, P. N. Quested, K. C. Mills, A. Nagashima, Y. Sato, and Wakeham W. A. Reference data for the density and viscosity of liquid aluminum and liquid iron. J. Phys. Chem. Ref. Data, 35:285–300, 2006. doi: 10.1063/1.2149380.
- Z. S. Basinski, W. Hume-Rothery, and A. L. Sutton. The lattice expansion of iron. Proc. R. Soc. A, 229:459–467, 1955. doi: 10.1098/rspa.1955.0102.
- T. L. Beck. Real-space mesh techniques in density-functional theory. Rev. Mod. Phys., 72:1041–1080, 2000. doi: 10.1103/RevModPhys.72.1041.
- A. B. Belonoshko, T. Lukinov, J. Fu, J. Zhao, S. Davis, and S. I. Simak. Stabilization of body-centred cubic iron under inner-core conditions. Nat. Geosci., 10:312–316, 2017. doi: 10.1038/ngeo2892.
- Y. Bi, H. Tan, and F. Jing. Electrical conductivity of iron under shock compression up to 200 GPa. J. Phys.: Condens. Matter, 14:10849–10854, 2002. doi: 10.1088/0953-8984/14/44/389.
- J. M. Brown and R. G. McQueen. Phase transitions, Grüneisen parameter, and elasticity for shocked iron between 77 GPa and 400 GPa. J. Geophys. Res. Solid Earth, 91:7485–7494, 1986. doi: 10.1029/JB091iB07p07485.
- K. Burke. Perspective on density functional theory. J. Chem. Phys., 136:150901, 2012. doi: 10.1063/1.4704546.
- A. Cezairliyan and J. L. McClure. Thermophysical measurements on iron above 1500 K using a transient (subsecond) technique. J. Res. Nat. Bur. Stds., 78A:1–4, 1974.

- R. E. Cohen, L. Stixrude, and E. Wasserman. Tight-binding computations of elastic anisotropy of Fe, Xe, and Si under compression. Phys. Rev. B, 56:8575–8589, 1997. doi: 10.1103/PhysRevB.56.8575.
- N. de Koker and L. Stixrude. Self-consistent thermodynamic description of silicate liquids, with application to shock melting of MgO periclase and MgSiO<sub>3</sub> perovskite. Geophys. J. Int., 178:162–179, 2009. doi: 10.1111/j.1365-246X.2009.04142.x.
- N. de Koker, G. Steinle-Neumann, and V. Vlček. Electrical resistivity and thermal conductivity of liquid Fe alloys at high P and T, and heat flux in Earth’s core. Proc. Natl. Acad. Sci. USA, 109:4070–4073, 2012. doi: 10.1073/pnas.1111841109.
- P. D. Desai. Thermodynamic properties of iron and silicon. Phys. Chem. Ref. Data, 15:967–983, 1986. doi: 10.1063/1.555761.
- D. J. Dever. Temperature dependence of the elastic constants in  $\alpha$ -iron single crystals: relationship to spin order and diffusion anomalies. J. Appl. Phys., 43:3293–3301, 1972. doi: 10.1063/1.1661710.
- G. Dharmaraj and S. Stanley. Effect of inner core conductivity on planetary dynamo models. Phys. Earth Planet. Inter., 212:1–9, 2012. doi: 10.1016/j.pepi.2012.09.003.
- W. D. Drotning. Thermal expansion of iron, cobalt, nickel, and copper at temperatures up to 600 K above melting. High Temp. – High Press., 13:441–458, 1981.
- B. K. Godwal, F. González-Cataldo, A. K. Verma, L. Stixrude, and R. Jeanloz. Stability of iron crystal structures at 0.3-1.5 TPa. Earth Planet. Sci. Lett., 409:299–306, 2015. doi: 10.1016/j.epsl.2014.10.056.
- H. Gomi, K. Ohta, K. Hirose, S. Labrosse, R. Caracas, M. J. Verstraete, and J. W. Hernlund. The high conductivity of iron and thermal evolution of the Earth’s core. Phys. Earth Planet. Inter., 224:88–103, 2013. doi: 10.1016/j.pepi.2013.07.010.
- H. Gomi, K. Hirose, H. Akai, and Y. Fei. Electrical resistivity of substitutionally disordered hcp Fe-Si and Fe-Ni alloys: Chemically-induced resistivity saturation in the Earth’s core. Earth Planet. Sci. Lett., 451:51–61, 2016. doi: 10.1016/j.epsl.2016.07.011.
- P. Hunt, M. Sprik, and R. Vuilleumier. Thermal versus electronic broadening in the density of states of liquid water. Chem. Phys. Lett., 376:68–74, 2003. doi: 10.1016/S0009-2614(03)00954-0.

## BIBLIOGRAPHY

- A. F. Ioffe and A. R. Regel. Non-crystalline, amorphous and liquid electronic semiconductors. Prog. Semicond., 4:237–291, 1960.
- R. N. Keeler. Electrical conductivity of condensed media at high pressures. In Physics of High Energy Density, volume 7, page 271, 1971.
- T. Komabayashi. Thermodynamics of melting relations in the system Fe-FeO at high pressure: Implications for oxygen in the Earth’s core. J. Geophys. Res. Solid Earth, 119:4164–4177, 2014. doi: 10.1002/2014JB010980.
- F. Lhuillier, G. Hulot, and Y. Gallet. Statistical properties of reversals and chrons in numerical dynamos and implications for the geodynamo. Phys. Earth Planet. Inter., 220:19–36, 2013. doi: 10.1016/j.pepi.2013.04.005.
- G. Matassov. The Electrical Conductivity of Iron-Silicon Alloys at High Pressures and the Earth’s Core. PhD thesis, University of California, 1977.
- N. F. Mott. The electrical resistivity of liquid transition metals. Philos. Mag., 26: 1249–1261, 1972. doi: 10.1080/14786437208220339.
- P. M. Nasch and S. G. Steinemann. Density and thermal expansion of molten manganese, iron, nickel, copper, aluminum and tin by means of the gamma-ray attenuation technique. Phys. Chem. Liquids, 29:43–58, 1995. doi: 10.1080/00319109508030263.
- K. Ohta, Y. Kuwayama, K. Hirose, K. Shimizu, and Y. Ohishi. Experimental determination of the electrical resistivity of iron at Earth’s core conditions. Nature, 534: 95–98, 2016. doi: 10.1038/nature17957.
- M. Pozzo, C. Davies, D. Gubbins, and D. Alfè. Thermal and electrical conductivity of iron at Earth’s core conditions. Nature, 485:355–358, 2012. doi: 10.1038/nature11031.
- M. Pozzo, C. Davies, D. Gubbins, and D. Alfè. Transport properties for liquid silicon-oxygen-iron mixtures at Earth’s core conditions. Phys. Rev. B, 87:014110, 2013. doi: 10.1103/PhysRevB.87.014110.
- M. Pozzo, C. Davies, D. Gubbins, and D. Alfè. Thermal and electrical conductivity of solid iron and iron-silicon mixtures at Earth’s core conditions. Earth Planet. Sci. Lett., 393:159–164, 2014. doi: 10.1016/j.epsl.2014.02.047.

- G. Román-Pérez and J. M. Soler. Efficient implementation of a van der Waals density functional: Application to double-wall carbon nanotubes. Phys. Rev. Lett., 103:096102, 2009. doi: 10.1103/PhysRevLett.103.096102.
- A. M. Rosenfeld and M. J. Stott. Change in resistivity of simple metals on melting. Phys. Rev. B, 42:3406–3414, 1990. doi: 10.1103/PhysRevB.42.3406.
- C. T. Seagle, E. Cottrell, Y. Fei, D. R. Hummer, and V. B. Prakapenka. Electrical and thermal transport properties of iron and iron-silicon alloy at high pressure. Geophys. Res. Lett., 40:5377–5381, 2013. doi: 10.1002/2013GL057930.
- R. A. Secco and H. H. Schlössin. The electrical resistivity of solid and liquid Fe at pressures up to 7 GPa. J. Geophys. Res. Solid Earth, 94:5887–5894, 1989. doi: 10.1029/JB094iB05p05887.
- F. D. Stacey and O. L. Anderson. Electrical and thermal conductivities of Fe-Ni-Si alloy under core conditions. Phys. Earth Planet. Inter., 124:153–162, 2001. doi: 10.1016/S0031-9201(01)00186-8.
- F. D. Stacey and D. E. Loper. A revised estimate of the conductivity of iron alloy at high pressure and implications for the core energy balance. Phys. Earth Planet. Inter., 161:13–18, 2007. doi: 10.1016/j.pepi.2006.12.001.
- S. Suehiro, K. Ohta, K. Hirose, G. Morard, and Y. Ohishi. The influence of sulfur on the electrical resistivity of hcp iron: Implications for the core conductivity of Mars and Earth. Geophys. Res. Lett., 44:8254–8259, 2017. doi: 10.1002/2017GL074021.
- S. Tateno, K. Hirose, Y. Ohishi, and Y. Tatsumi. The structure of iron in Earth’s inner core. Science, 330:359–361, 2010. doi: 10.1126/science.1194662.
- T. Tschentscher, C. Bressler, J. Grünert, A. Madsen, A. P. Mancuso, M. Meyer, A. Scherz, H. Sinn, and U. Zastra. Photon beam transport and scientific instruments at the European XFEL. Appl. Sci., 7:592, 2017. doi: 10.3390/app7060592.
- Y. Tsu, K. Takano, and Y. Shiraishi. The velocities of ultrasound in molten iron, cobalt and nickel. Bull. Res. Inst. Miner. Dressing Metall., 41:1–8, 1985.
- J. B. van Zytveld. Electrical resistivities of liquid transition metals. Journal de Physique, 41:503–506, 1980. doi: 10.1051/jphyscol:19808126.

## BIBLIOGRAPHY

- V. Vlček, N. de Koker, and G. Steinle-Neumann. Electrical and thermal conductivity of al liquid at high pressures and temperatures from ab initio computations. Phys. Rev. B, 85:184201, 2012. doi: 10.1103/PhysRevB.85.184201.
- F. Wagle, G. Steinle-Neumann, and N. de Koker. Saturation and negative temperature coefficient of electrical resistivity in liquid iron-sulfur alloys at high densities from first principles calculations. Phys. Rev. B, 97:094307, 2018. doi: 10.1103/PhysRevB.97.094307.
- Y. Waseda and M. Ohtani. Static structure of liquid noble and transition metals by X-ray diffraction. Phys. Status Solidi B, 62:535–546, 1974. doi: 10.1002/pssb.2220620224.
- J. Wicht. Inner-core conductivity in numerical dynamo simulations. Phys. Earth Planet. Inter., 132:281–302, 2002. doi: 10.1016/S0031-9201(02)00078-X.
- Q. Williams. Bottom-up versus top-down solidification of the cores of small solar system bodies: Constraints on paradoxical cores. Earth Planet. Sci. Lett., 284: 564–569, 2009. doi: doi.org/10.1016/j.epsl.2009.05.019.
- J. M. Ziman. A theory of the electrical properties of liquid metals. I: The monovalent metals. Philos. Mag., 6:1013–1034, 1961. doi: 10.1080/14786436108243361.

**4 Wagle *et al.* (2018),  
C. R. Geosci. (in press)**



Contents lists available at ScienceDirect

Comptes Rendus Geoscience

www.sciencedirect.com



Internal Geophysics (Physics of Earth's Interior)

## Resistivity saturation in liquid iron–light-element alloys at conditions of planetary cores from first principles computations

Fabian Wagle<sup>a,\*</sup>, Gerd Steinle-Neumann<sup>a</sup>, Nico de Koker<sup>a,b</sup>

<sup>a</sup>Bayerisches Geoinstitut, Universität Bayreuth, 95440 Bayreuth, Germany

<sup>b</sup>School of Geosciences, University of the Witwatersrand, Private Bag 3, 2050 Wits, South Africa

### ARTICLE INFO

#### Article history:

Received 8 March 2018

Accepted after revision 14 May 2018

Available online xxx

Handled by James Badro

#### Keywords:

Electrical conductivity

Resistivity saturation

Mean free path

Planetary interiors

Earth's core

Coordination numbers

### ABSTRACT

We present a comprehensive analysis of electrical resistivity for liquid Fe–Si, Fe–S, and Fe–O alloys from first principles computations, covering the pressure/temperature conditions and major light element candidates inside the cores of terrestrial planets. By fitting optical conductivity with the Drude formula, we explicitly calculate the effective electron mean free path, and show that it becomes comparable to the interatomic distance for high densities and Si/S concentrations (Ioffe–Regel criterion). In approaching the Ioffe–Regel criterion, the temperature coefficient of resistivity decreases with compression for all compositions, eventually vanishes (Fe–Si), or even changes sign (Fe–S). Differences in resistivity and the degree of saturation between the iron alloys studied are explained in terms of iron–light element coordination numbers and their density dependence. Due to competing temperature and pressure effects, resistivity profiles along proposed core adiabats exhibit a small negative pressure gradient.

© 2018 Académie des sciences. Published by Elsevier Masson SAS. All rights reserved.

### 1. Introduction

In the generation of Earth's magnetic field by thermochemical convection in the outer core (OC) (Merrill et al., 1996), the electrical resistivity  $\rho$  of the convecting liquid determines the dissipation of the magnetic field. It constrains two critical aspects of the geodynamo: (i) the timescale of dipole decay (Wicht, 2002), and therefore the stability of the magnetic field in a specific polarity, and (ii) the fluid velocity required for generating a given magnetic field strength (Davies et al., 2015).

Resistivity and the energy budget of convection depend on chemical composition, for which the current understanding inside Earth's core is based on seismic observations in combination with cosmochemical constraints.

Both the solid inner core (IC) and the liquid OC are less dense than pure iron or iron–nickel alloys, which requires the presence of one or more lighter elements (Birch, 1952). Furthermore, the density discontinuity at the inner core boundary (ICB) is too large to be caused by a liquid–solid phase transition alone, suggesting that at least one light element preferentially partitions into the OC (Masters and Gubbins, 2003). Light elements need to be sufficiently abundant in the solar system and readily alloy with iron under the conditions at which the Earth differentiated, making silicon, oxygen and sulfur primary candidates (Poirier, 1994). In addition to density, acoustic velocities need to match those of a seismic reference model, such as PREM (Dziewonski and Anderson, 1981), which cannot be achieved by a binary alloy of one of those elements with iron (Badro et al., 2015). As the Earth is depleted in sulfur compared to chondritic composition (Dreibus and Palme, 1996), silicon and oxygen are assumed to be the major light

\* Corresponding author.

<https://doi.org/10.1016/j.crte.2018.05.002>

1631–0713/© 2018 Académie des sciences. Published by Elsevier Masson SAS. All rights reserved.

Please cite this article in press as: Wagle F, et al. Resistivity saturation in liquid iron–light-element alloys at conditions of planetary cores from first principles computations. C. R. Geoscience (2018), <https://doi.org/10.1016/j.crte.2018.05.002>

elements in the core (Tsuno et al., 2013) with estimated concentrations of 2–3.5% Si and 2.7–5% O (Badro et al., 2015). The presence of carbon and hydrogen is likely limited to below 0.2% due to their volatility (McDonough, 2003), and consequently these elements are not considered in the present study.

While the sulfur concentration in the Earth's core has been estimated to be below 2% (Dreibus and Palme, 1996), other terrestrial planets are expected to contain substantially more sulfur. Its high solubility in iron, its high abundance in iron meteorites, the absence of a giant impact that leads to a loss of volatiles from the Earth (Halliday, 2004), and more reducing conditions during planetary differentiation (Namur et al., 2016) support models for the cores of Mercury (Hauck et al., 2013; Rivoldini et al., 2009), Mars (Lodders and Fegley, 1997), and Ganymede (Rückriemen et al., 2015) which assume sulfur to be the sole light element.

There have been considerable advances in constraining electronic transport properties in recent years, both experimentally and computationally. First principles calculations on liquid iron (de Koker et al., 2012; Pozzo et al., 2012) first predicted resistivity at conditions of the Earth's core to be substantially lower than previous estimates (Stacey and Anderson, 2001; Stacey and Loper, 2007). The results are consistent with dynamic compression experiments at high pressure ( $P$ ) and temperature ( $T$ ) (Keeler, 1971), while  $\rho$  is underestimated at ambient (van Zytveld, 1980) and low  $P$  conditions (Secco and Schlössin, 1989). Recently, similarly low resistivity values of hexagonal close packed iron at high  $P$ /high  $T$  have been reported by Ohta et al. (2016), using a laser-heated diamond anvil cell (DAC).

In addition to early static and dynamic compression experiments (Bridgman, 1957; Matassov, 1977), resistivity of Fe–Si alloys has been measured in large-volume press experiments at low  $P$  and high  $T$  (Kiarasi and Secco, 2015), and beyond 100 GPa in the DAC (Gomi et al., 2013; Seagle et al., 2013). High-temperature extrapolations based on DAC experiments at ambient  $T$  yield values consistent with computational results at conditions inside Earth's core.

Single-phase samples of iron alloys containing oxygen and sulfur are challenging to synthesize (Mori et al., 2017); therefore, resistivity data is scarce for compositions in these systems. A recent study circumvented this problem by calculating impurity resistivity of sulfur from measured values of Fe, Fe–Si (Gomi et al., 2013, 2016) and the ternary Fe–Si–S alloy using Matthiessen's rule (Suehiro et al., 2017).

An important assumption in fitting experimental data was that resistivity of iron and its alloys does not follow a linear trend with  $T$ , as expected from the Bloch–Grüneisen equation, but appears to saturate at high  $P$ / $T$  conditions (Gomi et al., 2013, 2016; Ohta et al., 2016). Resistivity saturation occurs for highly resistive transition metal alloys (Gunnarsson et al., 2003), where the electron mean free path becomes comparable to the interatomic distance, which is known as the Ioffe–Regel criterion (Ioffe and Regel, 1960). First principles computations suggest a decrease in the slope of  $\rho(T)$  for hexagonal-close-packed iron at high compression (Pozzo and Alfè, 2016), approaching saturation.

With the incorporation of light elements, resistivity increases due to the additional impurity scattering mechanism. For crystalline alloys, the concentration ( $c$ ) dependence of resistivity is generally described by Nordheim's rule as  $\rho \propto c(1 - c)$  (Nordheim, 1928), but fundamental deviations from that relation have been observed in liquid and amorphous alloys (e.g., Enderby and Howe, 1968).

Faber–Ziman theory (Faber and Ziman, 1965; Ziman, 1961) relates the dependence of resistivity for liquid alloys on concentration to structural properties of the liquid, i.e. to the microscopic short-range order described by partial structure factors  $S_{\alpha\beta}(q)$ . While qualitative features are described well by Faber–Ziman theory, there is substantial quantitative disagreement, especially for transition metal alloys. Iron and iron alloys have a complex electronic structure with partially filled  $d$ -bands at the Fermi level and are therefore not well described by Faber–Ziman theory, as far as absolute resistivity values are concerned.

We build our study on density functional theory-based molecular dynamics (DFT–MD) trajectories and resistivity results for liquid Fe, Fe–Si, and Fe–O alloys by de Koker et al. (2012), and Fe–S alloys by Wagle et al. (2018). In this paper, we consider in detail the relation between the liquid structure and computed values of  $\rho$  for binary iron alloys with the major light element candidates Si, O, and S. We do so by calculating the effective mean free path from the Drude response of optical conductivity, from which we identify different saturation mechanisms and show correlations with structural properties of the liquid. Finally, we discuss implications on conductivity profiles, and their influence on the dynamos of terrestrial planets.

## 2. Methods

DFT–MD simulations were performed on cells containing 128 atoms in the  $N$ – $V$ – $T$  ensemble, using the plane-wave code VASP (Kresse and Furthmüller, 1996a,b; Kresse and Hafner, 1993). Cubic cells in a volume range between 7.09 and 11.82 Å<sup>3</sup>/atom ( $V_0$ )—covering the  $P$ -range of the Earth—and light element contents of 12.5 (Fe<sub>7</sub>X) and 25 at.% (Fe<sub>3</sub>X) were set up by randomly replacing iron with light element atoms (X) in molten configurations. Atomic coordinates were updated using a time step of 1 fs, and  $T$  was controlled by the Nosé thermostat (Nosé, 1984), with  $T$  ranging from 2000 K to 8000 K. At each time step, the electron density was computed using the projector-augmented-wave (PAW) method (Kresse and Joubert, 1999) with the PBE exchange–correlation functional (Perdew et al., 1996) and a plane wave cutoff energy of 400 eV. Electronic states were occupied according to Fermi–Dirac statistics at  $T$  of the thermostat. Brillouin zone sampling was restricted to the zone center. After equilibration of  $P$ ,  $T$ , and the total energy ( $E$ ) had been achieved (typically after a few hundred fs), the DFT–MD simulations were continued for at least 15 ps.

We observe non-vanishing slopes of the atomic mean square displacement at all simulation conditions, even for  $T$  below the liquidus at high density. This indicates that the liquid is metastable, i.e. cells are not frozen to a glass for

which the mean square displacement would reach a constant value after some simulation time.

Partial radial distribution functions  $g_{\alpha\beta}(r)$  were obtained by a time average over all equilibrated configurations from the DFT-MD trajectories. The unnormalized radial distribution function  $G_{\alpha\beta}(r) = 4\pi r^2 \rho g_{\alpha\beta}(r)$ , with number density  $\rho$ , describes how the particle density of species  $\beta$  varies with distance to a reference particle of species  $\alpha$ . We define the properties of the first coordination shell by  $G_{\alpha\beta}(r)$  up to the first minimum: the first coordination number is then represented by the integral and the interatomic distance by the median of the distribution.

For calculating electronic transport properties, at least six uncorrelated snapshots were extracted from the MD simulations (i.e. separated by time periods greater than that required for the velocity autocorrelation function to decay to zero) and Kohn–Sham wavefunctions  $\psi_k$ , their energy eigenvalues  $\epsilon_k$ , and the gradient of the Hamiltonian with respect to reciprocal wave vector  $\partial H/\partial \mathbf{k}$  were computed using the *Abinit* software package (Gonze, 1997; Gonze et al., 2009; Torrent et al., 2008). From those, optical conductivity was calculated within the Kubo–Greenwood formalism as

$$\sigma(\omega) = \frac{he^2}{V_{\text{cell}}} \sum_{k,k'} [f(\epsilon_{k'}) - f(\epsilon_k)] \delta(\epsilon_{k'} - \epsilon_k - \hbar\omega) \langle \psi_{k'} | \mu | \psi_k \rangle \langle \psi_k | \mu | \psi_{k'} \rangle, \quad (1)$$

implemented in the *conducti*-module of *Abinit* (Recoules and Crocombette, 2005). In Eq. (1),  $\hbar$  denotes the reduced Planck constant,  $e$  the elementary charge,  $V_{\text{cell}}$  the cell volume,  $\omega$  the frequency of the external field and  $\mu = 1/\hbar \cdot \partial H/\partial \mathbf{k}$  the velocity operator.

By fitting the Drude formula

$$R[\sigma(\omega)] = \frac{\sigma_0}{1 + (\omega\tau)^2} \quad (2)$$

to the Kubo–Greenwood results for each snapshot, we extracted the DC limit of electrical resistivity  $\rho = \sigma_0^{-1}$  and the effective relaxation time  $\tau$ . We averaged  $\sigma$  and  $\tau$  over the snapshots and took one standard deviation as uncertainty. Calculations with denser grids of  $2 \times 2 \times 2$  and  $3 \times 3 \times 3$   $k$ -points showed that  $\sigma(\omega)$  is sufficiently converged (to within 3%) using a single  $k$ -point (Wagle et al., 2018).

The resulting  $\rho(V, T)$  values were fit with a parallel resistor model to interpolate between results and extrapolate to

conditions not investigated:

$$\frac{1}{\rho(V, T)} = \frac{1}{\rho_{\text{BG}}(V, T)} + \frac{1}{\rho_{\text{sat}}(V)} + \frac{1}{\rho_{\text{el}}(T)}, \quad (3)$$

where

$$\rho_{\text{BG}} = \rho_0 \left(\frac{V}{V_0}\right)^a + \rho_1 \left(\frac{V}{V_0}\right)^b \frac{T}{T_0} \quad (4)$$

is the empirical expression used by de Koker et al. (2012) based on the Bloch–Grüneisen formula.

$$\rho_{\text{sat}} = c \left(\frac{V}{V_0}\right)^{\frac{1}{3}} \quad (5)$$

is a term accounting for resistivity saturation, similar to expressions used by Gomi et al. (2013) and Suehiro et al. (2017), and

$$\rho_{\text{el}} = d \frac{T_0}{T} \quad (6)$$

describes the effect of thermal broadening of the density of states, which, for the Fe–S system, is analyzed in more detail by Wagle et al. (2018). The fitting parameters are listed in Table 1.

In order to describe electrical resistivity as a function of  $P$ , suitable for comparison to experiments and for applications in planetary models, we fit a thermodynamic model to the DFT-MD results that is based on a separation of the Helmholtz energy into ideal gas, electronic, and excess terms (de Koker and Stixrude, 2009; Vlček et al., 2012). The volume dependence of the excess term is represented by Eulerian finite strain ( $f$ ) with exponent  $n=2$  and a similarly reduced  $T$ -term ( $\theta$ ) with exponent  $m=0.79$  and expansion orders  $O_f=3$  and  $O_\theta=2$ , parameters that best describe the results for liquid iron (de Koker et al., 2012). The thermodynamic properties at reference conditions are summarized in Table 2.

### 3. Results and discussion

#### 3.1. Liquid structure

The results of our structural analysis in terms of  $g_{\alpha\beta}(r)$ , interatomic distances and coordination numbers (Figs. 1 and 2) for the binary alloys in the Fe–S, Fe–O, and Fe–Si systems reveal the following key observations.

- (i) Silicon incorporates substitutionally into liquid iron, with average nearest-neighbor distances very similar

**Table 1**

Fit parameters of the models for  $\rho(V, T)$  (Eq. (3)) for the liquid iron–light-element alloys considered. As the individual terms (Eqs. (4)–(6)) for describing resistivity results are difficult to separate, the fit is not well constrained and uncertainties in the fitting parameters exceed their values in most cases. Parameters for Fe and the Fe–S alloys have been reported in a previous study (Wagle et al., 2018).

		Fe	Fe <sub>7</sub> O	Fe <sub>3</sub> O	Fe <sub>7</sub> Si	Fe <sub>3</sub> Si	Fe <sub>7</sub> S	Fe <sub>3</sub> S
$\rho_{\text{OR}}$	[ $\mu\Omega$ cm]	75.10	87.80	100.3	97.09	193.4	89.03	105.2
$\rho_{\text{IR}}$	[ $\mu\Omega$ cm]	21.48	11.88	7.979	4.377	76.74	12.73	12.06
$a$		0.792	0.645	0.717	0.607	0.465	0.389	0.124
$b$		1.479	1.695	1.482	1.617	2.495	1.804	2.686
$c$	[ $\mu\Omega$ cm]	747.2	1823	$7.771 \times 10^5$	6030	254.0	2077	6609
$d$	[ $\mu\Omega$ cm]	1405	4202	$2.356 \times 10^6$	24810	2006	2829	2910

Please cite this article in press as: Wagle F, et al. Resistivity saturation in liquid iron–light-element alloys at conditions of planetary cores from first principles computations. C. R. Geoscience (2018), <https://doi.org/10.1016/j.crte.2018.05.002>

**Table 2**

Parameters of the modified thermodynamic model by de Koker and Stixrude (2009) for  $V_0 = 11.82 \text{ \AA}^3/\text{atom}$  and  $T_0 = 2000 \text{ K}$  (reference conditions). Values for extensive variables are per mol of formula units. Parameters for Fe and the Fe–S alloys have been reported in a previous study (Wagle et al., 2018).

		Fe	Fe <sub>7</sub> O	Fe <sub>3</sub> O	Fe <sub>7</sub> Si	Fe <sub>3</sub> Si	Fe <sub>7</sub> S	Fe <sub>3</sub> S
$P_{\text{XS0}}$	[GPa]	−2.335	−1.186	5.534	0.846	5.534	0.846	5.534
$K_{T,\text{XS0}}$	[GPa]	131.4	101.0	42.56	137.3	133.1	137.8	140.0
$K'_{T,\text{XS0}}$		5.161	5.706	9.223	5.031	5.122	4.694	4.736
$\alpha K_{T,\text{XS0}}$	[GPa/K]	$8.822 \times 10^{-3}$	$5.939 \times 10^{-3}$	$1.252 \times 10^{-3}$	$8.363 \times 10^{-3}$	$6.138 \times 10^{-3}$	$8.620 \times 10^{-3}$	$7.194 \times 10^{-3}$
$V_0 \left( \frac{\partial \alpha K_T}{\partial V} \right)_{T,\text{XS0}}$	[GPa/K]	$-1.563 \times 10^{-2}$	$-1.518 \times 10^{-2}$	$-2.131 \times 10^{-2}$	$-1.229 \times 10^{-2}$	$-9.111 \times 10^{-3}$	$-1.660 \times 10^{-2}$	$-1.327 \times 10^{-2}$
$T_0 \left( \frac{\partial \alpha K_T}{\partial T} \right)_{T,\text{XS0}}$	[GPa/K]	$-3.348 \times 10^{-3}$	$-1.352 \times 10^{-3}$	$4.956 \times 10^{-4}$	$-3.288 \times 10^{-3}$	$-1.739 \times 10^{-3}$	$-2.376 \times 10^{-3}$	$-1.808 \times 10^{-3}$
$V_0^2 \left( \frac{\partial^2 \alpha K_T}{\partial V^2} \right)_{T,\text{XS0}}$	[GPa/K]	$2.840 \times 10^{-2}$	$3.401 \times 10^{-2}$	$5.741 \times 10^{-2}$	$2.115 \times 10^{-2}$	$9.670 \times 10^{-3}$	$5.115 \times 10^{-2}$	$3.534 \times 10^{-2}$
$C_{V,\text{XS0}}$	[J/(mol K)]	18.50	183.1	100.5	189.5	102.3	185.1	92.90
$V_0 \left( \frac{\partial C_V}{\partial V} \right)_{T,\text{XS0}}$	[kJ/(mol K)]	15.84	313.6	86.07	324.7	87.66	317.1	79.57
$V_0^2 \left( \frac{\partial^2 C_V}{\partial V^2} \right)_{T,\text{XS0}}$	[kJ/(mol K)]	$2.113 \times 10^{-2}$	$1.626 \times 10^{-1}$	$1.193 \times 10^{-1}$	$6.850 \times 10^{-2}$	$-3.449 \times 10^{-2}$	$3.094 \times 10^{-1}$	$1.033 \times 10^{-1}$
$\zeta_0$	[J/(mol K <sup>2</sup> )]	3.486	32.67	14.51	27.18	12.35	30.04	12.36
$\xi$		0.843	0.911	0.671	0.730	0.925	1.096	1.006

for Fe–Fe, Fe–Si, and Si–Si (Fig. 1). Fe–Si alloys are in the vicinity of the close-packing limit of a twelve-fold coordination, which does not change with  $P$  (Fig. 2), in agreement with previous results (Posner et al., 2017b). Structural data from *in situ* X-ray diffraction show the same trend in the low- $P$  range (Morard et al., 2008; Sanloup et al., 2002).

- (ii) The average Fe–O distance is substantially shorter than the Fe–Fe distance, and two oxygen atoms are typically separated by one iron atom. This difference in size has been attributed to account for the observation that oxygen preferentially partitions into the liquid over the solid (Alfè et al., 2002; Morard et al., 2014). With increasing  $P$ , the six-fold coordination of iron

around oxygen at ambient conditions increases to eight-fold at core conditions. The transition of the compression mechanism from changing coordination to shortening the interatomic distance has been shown to affect diffusive transport for the Fe–O system (Posner et al., 2017a,c).

- (iii) Fe–S alloys at high  $P$  exhibit a net S–S repulsion, as shown by the virtual absence of a typical nearest-neighbor peak for  $g_{\text{SS}}(r)$  between 2.0 and 2.5 Å and the presence of a next-nearest neighbor maximum at  $\sim 3.5 \text{ \AA}$  (Fig. 1a). This has been linked to a strengthening of covalent bonds between Fe and S with increasing  $P$ , resulting in high Fe–S coordination (Alfè and Gillan, 1998). Fig. 2 shows increasing Fe–S coordination with compression, suggesting sulfur to shift from interstitial-like to substitutional incorporation in the liquid. At the highest compressions, Fe–S approaches a close-packed short-range structure.

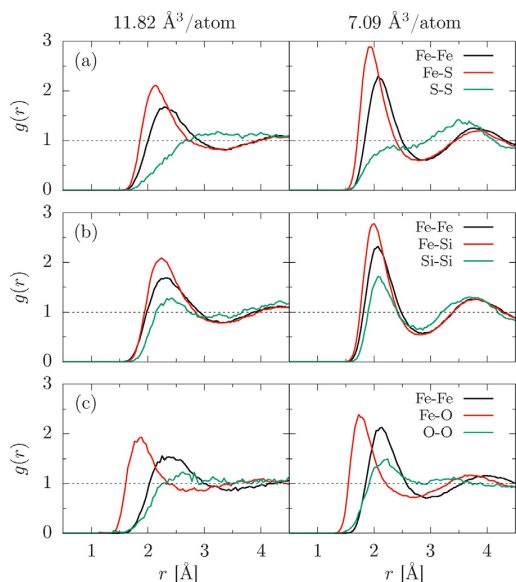


**Fig. 1.** Partial radial distribution functions for (a) Fe<sub>3</sub>S, (b) Fe<sub>3</sub>Si, and (c) Fe<sub>3</sub>O at 8000 K and two unit cell volumes ( $V_0$  and  $V/V_0=0.6$ ).

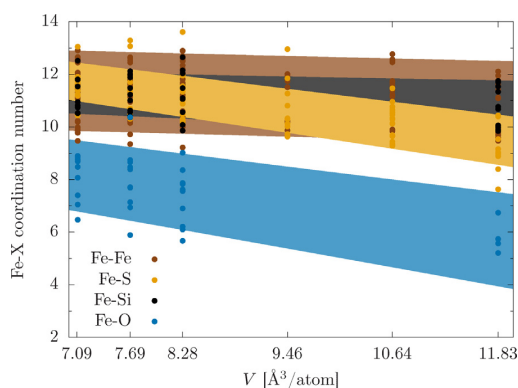


**Fig. 2.** First iron coordination numbers around an atom of species X. The vertical scatter at each volume arises from including results for different light element concentrations at different temperatures. Linear regressions with propagated uncertainty bands are shown in matching colors to guide the eye.

Please cite this article in press as: Wagle F, et al. Resistivity saturation in liquid iron–light-element alloys at conditions of planetary cores from first principles computations. C. R. Geoscience (2018), <https://doi.org/10.1016/j.crte.2018.05.002>

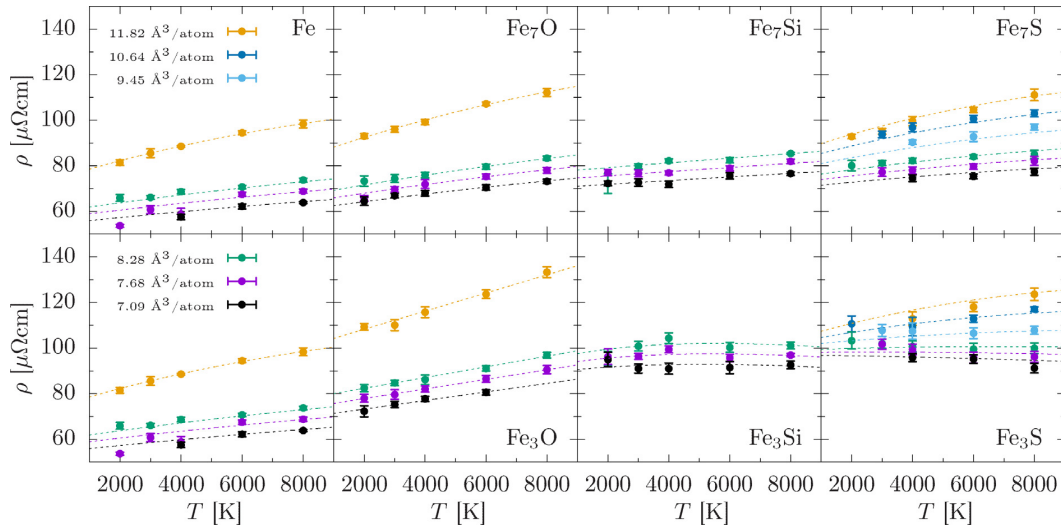


Fig. 3. Electrical resistivity of liquid iron and various binary iron alloys as a function of temperature along isochores. The resistivity model fit for  $\rho(V, T)$  (Eq. (3)) is shown by dashed lines.

### 3.2. Resistivity saturation and electron mean free path

As a structural dependence of resistivity is expected from transport theory of liquid metals (Faber and Ziman, 1965; Ziman, 1961), it is our goal to describe the correlations between the observations made in Section 3.1 and resistivity calculated from first principles (Fig. 3).

Generally,  $\rho$  increases with  $T$  and  $c$ . Larger vibrational amplitudes and shorter distances between impurity atoms lead to a decrease in the effective electron mean free path ( $\chi_{\text{eff}}$ ), approaching the Ioffe–Regel saturation limit, where  $\chi_{\text{eff}}$  becomes comparable to the interatomic distance. However, the addition of the same mole fraction of different light elements leads to resistivity increases by different amounts, depending on volume and temperature.

For the low impurity concentrations considered ( $\text{Fe}_7\text{X}$ ), resistivity can be described reasonably well by a linear  $T$ -dependence above the Debye temperature ( $\Theta_D$ ) ( $\sim 1000$  K at low compression), consistent with Bloch–Grüneisen theory. With compression,  $\Theta_D$  increases based on the thermodynamic parameters from the DFT–MD simulation, and the values of  $\rho$  decrease. This behavior is well captured by the resistivity model (Eq. (3)).

For higher impurity concentrations ( $\text{Fe}_3\text{X}$ ), we find that  $\rho$  is higher (Fig. 3) and that the Bloch–Grüneisen behavior breaks down for  $\text{Fe}_3\text{Si}$  and  $\text{Fe}_3\text{S}$ . The temperature coefficient of resistivity (TCR) decreases with compression for all alloys, vanishes within uncertainty for the three smallest volumes of  $\text{Fe}_3\text{Si}$  and changes sign for  $\text{Fe}_3\text{S}$  for the smallest two volumes we consider. We have previously explained the negative TCR for  $\text{Fe}_3\text{S}$  by changes in the electronic structure that are only noticeable once the liquid has reached the Ioffe–Regel condition (Wagle et al., 2018).

In order to illustrate resistivity saturation mechanisms from a semi-classical picture of electron transport, we calculate the effective electron mean free path as  $\chi_{\text{eff}} = v_F \tau$ , where  $v_F = (\hbar/m) \cdot (3\pi^2 n_{\text{eff}})^{1/3}$  is the Fermi velocity,  $n_{\text{eff}} = (m\sigma_0)/(e^2 \tau)$  the effective number density of conduction electrons, and  $m$  the electron mass. Fig. 4 reveals three distinctive features.

- (i) For ambient  $P$  volumes ( $V_0 = 11.82 \text{ \AA}^3/\text{atom}$ ),  $\chi_{\text{eff}}$  approaches the mean interatomic distance asymptotically with increasing  $T$ , consistent with the thermally driven saturation process found in previous studies (Mooij, 1973; Pozzo and Alfè, 2016).
- (ii) At the lowest cell  $V$  considered ( $V = 7.09 \text{ \AA}^3/\text{atom}$ ),  $\chi_{\text{eff}}$  becomes shorter than at lower compression, due to the increased density of scattering centers. At first glance, this observation appears to be inconsistent with the fact that  $\rho$  decreases with compression (Fig. 3), but can be understood in terms of electronic structure (Wagle et al., 2018).
- (iii) With increasing light element concentration,  $\chi_{\text{eff}}$  decreases significantly. This reflects the expected behavior of an increased probability of impurity-caused scattering. For the highest compression, the Ioffe–Regel condition is satisfied for  $\text{Fe}_3\text{Si}$  and  $\text{Fe}_3\text{S}$  as  $\chi_{\text{eff}}$  becomes equal to the mean interatomic distance within uncertainty.

These observations match the resistivity behavior shown in Fig. 3 and explain the temperature effect on resistivity: while  $\chi_{\text{eff}}$  in pure iron and Fe–O alloys is still somewhat larger than the average spacing of scattering centers, resistivity is not yet saturated, and its  $T$ -

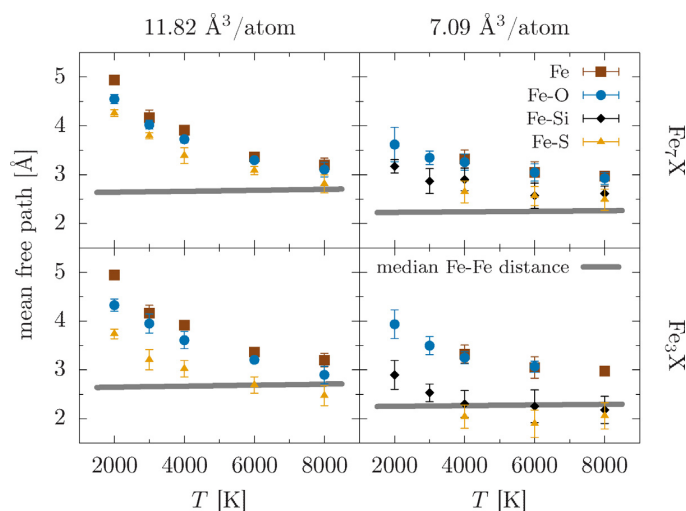


**Fig. 4.** Electron mean free path for liquid iron with 12.5 at.% (top) and 25 at.% (bottom) light element content for two cell volumes, near ambient  $P$  (left) and largest compression (right), obtained by a Drude fit to optical conductivity (Eq. (2)). The mean free path approaches the interatomic Fe–Fe distance in the alloys (median, thick gray lines) with increasing temperature, compression, and impurity concentration. For  $\text{Fe}_3\text{Si}$  and  $\text{Fe}_3\text{S}$  at the smallest cell volume, the Ioffe–Regel condition is satisfied.

dependence is retained. High concentrations of Si and S in the liquid iron alloy, on the other hand, drive the system into the Ioffe–Regel limit, resulting in a vanishing TCR.

A possible reason for the short mean free path of Fe–S alloys can be found in the S–S avoidance (Fig. 1) and high Fe–S coordination (Fig. 2), leading to a quasi-ordered short-range distribution of impurity scatterers in the liquid. Sulfur is the only alloying element that leads to a negative TCR. As saturation with compression is reached, secondary electronic effects at the Fermi surface are noticeable (Wagle et al., 2018). By contrast, silicon substitutes for iron in a random fashion to a good approximation, as shown by the similarity of pair distribution functions and coordination numbers compared to pure iron (Figs. 1 and 2). Impurity resistivity of oxygen is the lowest among the light elements investigated. It occupies interstitial positions between iron atoms and has the smallest scattering cross section, with little influence on total resistivity.

#### 4. Resistivity profiles of the cores of Mars and the Earth

The significance of saturation mechanisms on resistivity profiles of planetary cores is presented in Fig. 5, where we show  $\rho(P)$  along proposed core isentropes of Mars (Fei and Bertka, 2005) and the Earth (Kamada et al., 2012). The simultaneous increase of  $T$  and  $P$  along an isentrope leads to competing effects on resistivity (Section 3.2):  $\rho$  increases with  $T$  and decreases with  $P$ , with a net effect of slowly decreasing resistivity as a function of pressure. Fe–S alloys exhibit a significantly shallower slope than pure Fe, Fe–O and Fe–Si alloys at both low and high  $P$  conditions. This results in a resistivity crossover of the corresponding silicon and sulfur concentrations at conditions of the Earth’s OC, an

effect that is related to the ongoing coordination change in the highly saturated Fe–S alloy. Considering that  $x_{\text{eff}}$  is similarly shortened in both Fe–S and Fe–Si alloys (Fig. 4), the increase in Fe–S coordination with  $P$  (Fig. 2) and the effective S–S repulsion (Fig. 1) leads to more efficient impurity scattering than the randomly distributed Si atoms.

Fig. 5 contains datapoints for Fe–Si alloys, which have been directly measured in dynamic compression experiments or based on low- $T$  static experiments. Shock data for comparable Fe–Si alloys by Matassov (1977) show somewhat larger values than our computed resistivity profiles near the core–mantle boundary (CMB) pressure. Although the temperature corresponding to these data differs from the proposed isentrope by up to 1000 K,  $T$  is expected to have a small effect on resistivity in the highly resistive systems considered. We find our results to be in excellent agreement with the extrapolation of Gomi et al. (2013) at CMB pressure, and slightly higher at ICB pressure ( $\sim 10\%$ ).

Previous computational results for ternary liquid Fe–Si–O alloys along a different core adiabat (Pozzo et al., 2013) plot between our  $\text{Fe}_3\text{Si}$  and  $\text{Fe}_3\text{O}$  profiles, suggesting that the presence of O in an Fe–Si alloy lowers resistivity significantly. As a consequence of the Ioffe–Regel limit, the difference in  $T$  between the different adiabats used here and that in Pozzo et al. (2013) is not expected to have a large effect on resistivity. For pure iron, without the effect of saturation, their numbers along a hotter core adiabat ( $T_{\text{ICB}} \approx 6350$  K) are somewhat higher than ours.

Based on an analysis of experimental data for the Fe–Si–S system, Suehiro et al. (2017) calculated substantially lower and steeper resistivity profiles along the same isentropes, and, in contrast to our results, find sulfur to cause a smaller impurity resistivity than silicon. While the

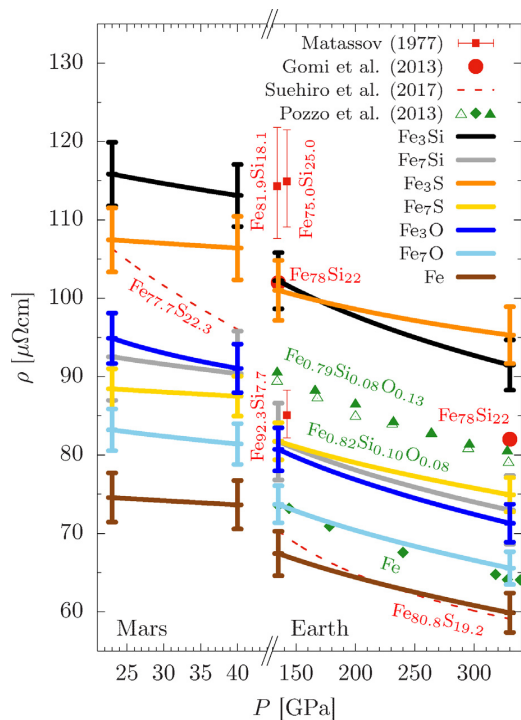


Fig. 5. Electrical resistivity profiles for various iron–light-element alloys along the proposed core isentropes of Mars (Fei and Bertka, 2005) and of the Earth (Kamada et al., 2012). The error bars shown have been calculated from the largest relative uncertainty of all resistivity datapoints of a given composition (Fig. 3). Results for  $\text{Fe}_{77.7}\text{S}_{22.3}$  (Mars) and  $\text{Fe}_{80.8}\text{S}_{19.2}$  (Earth) by Suehiro et al. (2017), computational results for the ternary Fe–Si–O system by Pozzo et al. (2012, 2013), as well as results from studies of various Fe–Si alloys made by Matassov (1977) (dynamic compression) and Gomi et al. (2013) (extrapolation of ambient temperature experiments) are included for comparison.

underlying extrapolated resistivity data for pure Fe and Fe–Si alloys (Gomi et al., 2013, 2016) are consistent with the DFT–MD–based results by de Koker et al. (2012) at conditions of the Earth’s core, it is surprising that the (inferred) conductivity profile of  $\text{Fe}_{80.8}\text{S}_{19.2}$  is very close to the computational results for pure iron. However, Matthiessen’s rule—which Suehiro et al. (2017) use for calculating the impurity resistivity of sulfur from pure Fe, Fe–Si, and Fe–Si–S resistivity—has been shown to break down in the saturation limit (Gomi et al., 2016), which might in part account for the discrepancy.

As resistivity of a liquid iron alloy with a large amount of light elements is saturated, and, as a consequence, the resistivity profile is virtually independent of  $T$ , it is not expected to change significantly over geological time as the planet cools. This likely remains valid across the melting point upon the formation of an inner core, for two reasons. (i) Si and S, the elements that are mostly responsible for resistivity saturation, partition almost equally between the liquid and the solid (Alfè et al., 2002). Oxygen, which preferentially remains in the liquid

portion of the core, contributes only little to total impurity resistivity. (ii) The resistivity discontinuity across the melting curve is expected to become negligible at high  $P$  (Wagle and Steinle-Neumann, 2018).

The evolution of a magnetic field generated by a convection-driven dynamo is therefore—to the first order—determined by the vigor of thermo-chemical convection, changing spatial constraints and magnetic boundary conditions as the inner core grows, not by changes in resistivity.

## 5. Conclusions

By using first principles simulations, we compute the structural properties and the electrical resistivity of liquid iron alloys up to pressure and temperature of the Earth’s inner core, with different concentrations of silicon, oxygen, and sulfur. We find correlations between short-range order and the effective electron mean free path.

At high pressure, silicon and sulfur substitute for iron in the liquid structure, and are found to substantially shorten the mean free path, which is reflected by high coordination numbers, near the close packing limit. As the mean free path becomes comparable to the mean interatomic distance, resistivity saturates. Once the system is close to saturation, resistivity becomes independent of temperature. Confirming results of previous studies, sulfur atoms prefer to be isolated from one another (Alfè and Gillan, 1998; Morard et al., 2014) and therefore distribute more evenly in liquid iron than silicon. Compared to a randomly substituted configuration, electron scattering is then more efficient, as scattering cross sections of impurity atoms are less likely to overlap. In the saturation limit at high densities and sulfur concentrations, this leads to a negative temperature coefficient of resistivity due to secondary electronic effects at the Fermi level, which cannot be observed in the Fe–Si system.

Oxygen, which is incorporated into the liquid on interstitial positions and has a considerably smaller scattering cross section, does not affect the mean free path compared to pure iron in a significant way. Correspondingly, the Fe–O system is not close to the Ioffe–Regel limit and retains a positive temperature coefficient of resistivity throughout the pressure and temperature range investigated.

Computed resistivity profiles along core adiabats for Mars and the Earth are considerably shallower than estimates based on experimental data using Matthiessen’s rule. As liquid iron alloys with high concentration of sulfur or silicon are in the Ioffe–Regel limit at high densities, resistivity will be independent of temperature and is therefore unlikely to change substantially with time during core evolution.

## Acknowledgments

This work was supported by Deutsche Forschungsgemeinschaft (German Science Foundation, DFG) in the Focus Program “Planetary Magnetism” (SPP 1488) with Grant STE1105/10-1 and Research Unit “Matter under Planetary

Interior Conditions” (FOR 2440) with Grant STE1105/13-1. Computing and data resources for the current project were provided by the Leibniz Supercomputing Centre of the Bavarian Academy of Sciences and Humanities ([www.lrz.de](http://www.lrz.de)). Comments by two anonymous reviewers helped to significantly improve the manuscript.

## References

- Alfè, D., Gillan, M.J., 1998. First-principles simulations of liquid Fe-S under Earth's core conditions. *Phys. Rev. B* 58, 8248–8256, <http://dx.doi.org/10.1103/PhysRevB.58.8248>.
- Alfè, D., Gillan, M.J., Price, G.D., 2002. Composition and temperature of the Earth's core constrained by combining ab initio calculations and seismic data. *Earth Planet. Sci. Lett.* 195, 91–98, [http://dx.doi.org/10.1016/S0012-821X\(01\)00568-4](http://dx.doi.org/10.1016/S0012-821X(01)00568-4).
- Badro, J., Brodholt, J.P., Piet, H., Siebert, J., Ryerson, F.J., 2015. Core formation and core composition from coupled geochemical and geophysical constraints. *Proc. Natl. Acad. Sci. USA* 112, 12310–12314, <http://dx.doi.org/10.1073/pnas.1505672112>.
- Birch, F., 1952. Elasticity and constitution of the Earth's interior. *J. Geophys. Res.* 57, 227–286, <http://dx.doi.org/10.1029/JZ057i002p0227>.
- Bridgman, P.W., 1957. Effects of pressure on binary alloys V fifteen alloys of metals of moderately high melting point. *Proc. Am. Acad. Arts Sci.* 84, 131–177.
- Davies, C., Pozzo, M., Gubbins, D., Alfè, D., 2015. Constraints from material properties on the dynamics and evolution of Earth's core. *Nat. Geosci.* 8, 678–685, <http://dx.doi.org/10.1038/ngeo2492>.
- Dreibus, G., Palme, H., 1996. Cosmochemical constraints on the sulfur content in the Earth's core. *Geochim. Cosmochim. Acta* 60, 1125–1130, [http://dx.doi.org/10.1016/0016-7037\(96\)00028-2](http://dx.doi.org/10.1016/0016-7037(96)00028-2).
- Dziewonski, A.M., Anderson, D.L., 1981. Preliminary reference Earth model. *Phys. Earth Planet. Inter.* 25, 297–356, [http://dx.doi.org/10.1016/0031-9201\(81\)90046-7](http://dx.doi.org/10.1016/0031-9201(81)90046-7).
- Enderby, J.E., Howe, R.A., 1968. Electron transport in liquid Cu-Sn. *Philos. Mag.* 18, 923–927, <http://dx.doi.org/10.1080/14786436808227514>.
- Faber, T.E., Ziman, J.M., 1965. A theory of the electrical properties of liquid metals. III. The resistivity of binary alloys. *Philos. Mag.* 11, 153–173, <http://dx.doi.org/10.1080/14786436508211931>.
- Fei, Y., Bertka, C., 2005. The interior of Mars. *Science* 308, 1120–1121, <http://dx.doi.org/10.1126/science.1110531>.
- Gomi, H., Hirose, K., Akai, H., Fei, Y., 2016. Electrical resistivity of substitutionally disordered hcp Fe-Si and Fe-Ni alloys: chemically-induced resistivity saturation in the Earth's core. *Earth Planet. Sci. Lett.* 451, 51–61, <http://dx.doi.org/10.1016/j.epsl.2016.07.011>.
- Gomi, H., Ohta, K., Hirose, K., Labrosse, S., Caracas, R., Verstraete, M.J., Hernlund, J.W., 2013. The high conductivity of iron and thermal evolution of the Earth's core. *Phys. Earth Planet. Inter.* 224, 88–103, <http://dx.doi.org/10.1016/j.pepi.2013.07.010>.
- Gonze, X., 1997. Dynamical matrices. Born effective charges, dielectric permittivity tensors, and interatomic force constants from density-functional perturbation theory. *Phys. Rev. B* 55, 10355–10368, <http://dx.doi.org/10.1103/PhysRevB.55.10355>.
- Gonze, X., Amadon, B., Anglade, P.M., Beuken, J.M., Bottin, F., Boulanger, P., Bruneval, F., Caliste, D., Caracas, R., Côté, M., Deutsch, T., Genovese, L., Ghosez, P., Giantomassi, M., Goedecker, S., Hamann, D.R., Hermet, P., Jollet, F., Jomard, G., Leroux, S., Mancini, M., Mazevet, S., Oliveira, M.J.T., Onida, G., Pouillon, Y., Rangel, T., Rignanese, G.M., Sangalli, D., Shaltaf, R., Torrent, M., Verstraete, M.J., Zerah, G., Zwanziger, J.W., 2009. Abinit: First-principles approach to material and nanosystem properties. *Comput. Phys. Commun.* 180, 2582–2615, <http://dx.doi.org/10.1016/j.cpc.2009.07.007>.
- Gunnarsson, O., Calandra, M., Han, J.E., 2003. Saturation of electrical resistivity. *Rev. Mod. Phys.* 75, 1085–1099, <http://dx.doi.org/10.1103/RevModPhys.75.1085>.
- Halliday, A.N., 2004. Mixing, volatile loss and compositional change during impact-driven accretion of the Earth. *Nature* 427, 505–509, <http://dx.doi.org/10.1038/nature02275>.
- Hauck, S.A., Margot, J.L., Solomon, S.C., Phillips, R.J., Johnson, C.L., Lemoine, F.G., Mazarico, E., McCoy, T.J., Padovan, S., Peale, S.J., Perry, M.E., Smith, D.E., Zuber, M.T., 2013. The curious case of Mercury's internal structure. *J. Geophys. Res.* 118, 1204–1220, <http://dx.doi.org/10.1002/jgre.20091>.
- Ioffe, A.F., Regel, A.R., 1960. Non-crystalline, amorphous and liquid electronic semiconductors. *Prog. Semicond.* 4, 237–291.
- Kamada, S., Ohtani, E., Terasaki, H., Sakai, T., Miyahara, M., Ohishi, Y., Hirao, N., 2012. Melting relationships in the Fe-Fe<sub>3</sub>S system up to the outer core conditions. *Earth Planet. Sci. Lett.* 359, 26–33, <http://dx.doi.org/10.1016/j.epsl.2012.09.038>.
- Keeler, R.N., 1971. Electrical conductivity of condensed media at high pressures. In: Caldirola, P., Knoepfel, H. (Eds.), *Physics of High Energy Density*. Academic Press, New York, pp. 106–125.
- Kiarasi, S., Secco, R.A., 2015. Pressure-induced electrical resistivity saturation of Fe<sub>7</sub>Si. *Phys. Status Solidi B* 252, 2034–2042, <http://dx.doi.org/10.1002/pssb.201552029>.
- de Koker, N., Steinle-Neumann, G., Vlček, V., 2012. Electrical resistivity and thermal conductivity of liquid Fe alloys at high P and T, and heat flux in Earth's core. *Proc. Natl. Acad. Sci. USA* 109, 4070–4073, <http://dx.doi.org/10.1073/pnas.1111841109>.
- de Koker, N., Stixrude, L., 2009. Self-consistent thermodynamic description of silicate liquids, with application to shock melting of MgO periclase and MgSiO<sub>3</sub> perovskite. *Geophys. J. Int.* 178, 162–179, <http://dx.doi.org/10.1111/j.1365-246X.2009.04142.x>.
- Kresse, G., Furthmüller, J., 1996a. Efficiency of ab-initio total energy calculations for metals and semiconductors using a plane-wave basis set. *Comput. Mat. Sci.* 6, 15–50, [http://dx.doi.org/10.1016/0927-0256\(96\)00008-0](http://dx.doi.org/10.1016/0927-0256(96)00008-0).
- Kresse, G., Furthmüller, J., 1996b. Efficient iterative schemes for ab initio total-energy calculations using a plane-wave basis set. *Phys. Rev. B* 54, 11169–11186, <http://dx.doi.org/10.1103/PhysRevB.54.11169>.
- Kresse, G., Hafner, J., 1993. Ab initio molecular dynamics for liquid metals. *Phys. Rev. B* 47, 558–561, <http://dx.doi.org/10.1103/PhysRevB.47.558>.
- Kresse, G., Joubert, D., 1999. From ultrasoft pseudopotentials to the projector augmented-wave method. *Phys. Rev. B* 59, 1758–1775, <http://dx.doi.org/10.1103/PhysRevB.59.1758>.
- Lodders, K., Fegley, B., 1997. An oxygen isotope model for the composition of Mars. *Icarus* 126, 373–394, <http://dx.doi.org/10.1006/icar.1996.5653>.
- Masters, G., Gubbins, D., 2003. On the resolution of density within the Earth. *Phys. Earth Planet. Inter.* 140, 159–167, <http://dx.doi.org/10.1016/j.pepi.2003.07.008>.
- Matassov, G., 1977. *The Electrical Conductivity of Iron-Silicon Alloys at High Pressures and the Earth's Core* (Ph.D. thesis) University of California, CA, USA.
- McDonough, W.F., 2003. *Treatise on Geochemistry*, vol. 2. Elsevier, Amsterdam, pp. 547–568, <http://dx.doi.org/10.1016/B0-08-043751-6/02015-6>.
- Merrill, R.T., McElhinny, M.W., McFadden, P.L., 1996. *The Magnetic Field of the Earth: Paleo-magnetism, the Core and the Deep Mantle*. Academic Press, San Diego, CA, USA.
- Moos, J.H., 1973. Electrical conduction in concentrated disordered transition metal alloys. *Phys. Status Solidi A* 17, 521–530, <http://dx.doi.org/10.1002/pssa.2210170217>.
- Morard, G., Andraut, D., Antonangeli, D., Bouchet, J., 2014. Properties of iron alloys under the Earth's core conditions. *C. R. Geoscience* 346, 130–139, <http://dx.doi.org/10.1016/j.crte.2014.04.007>.
- Morard, G., Sanloup, C., Guillot, B., Fiquet, G., Mezouar, M., Perrillat, J.P., Garbarino, G., Mibe, K., Komabayashi, T., Funakoshi, K., 2008. In situ structural investigation of Fe-S-Si immiscible liquid system and evolution of Fe-S bond properties with pressure. *J. Geophys. Res.* Solid Earth 113, B10205, <http://dx.doi.org/10.1029/2008JB005663>.
- Mori, Y., Ozawa, H., Hirose, K., Sinmyo, R., Tateno, S., Morard, G., Ohishi, Y., 2017. Melting experiments on Fe-Fe<sub>3</sub>S system to 254 GPa. *Earth Planet. Sci. Lett.* 464, 135–141, <http://dx.doi.org/10.1016/j.epsl.2017.02.021>.
- Namur, O., Charlier, B., Holtz, F., Cartier, C., McCammon, C., 2016. Sulfur solubility in reduced mafic silicate melts: implications for the speciation and distribution of sulfur on Mercury. *Earth Planet. Sci. Lett.* 448, 102–114, <http://dx.doi.org/10.1016/j.epsl.2016.05.024>.
- Nordheim, L., 1928. Über den Widerstand von Legierungen. *Naturwissenschaften* 16, 1042–1043, <http://dx.doi.org/10.1007/BF01506822>.
- Nosé, S., 1984. A unified formulation of the constant temperature molecular dynamics methods. *J. Chem. Phys.* 81, 511–519, <http://dx.doi.org/10.1063/1.447334>.
- Ohta, K., Kuwayama, Y., Hirose, K., Shimizu, K., Ohishi, Y., 2016. Experimental determination of the electrical resistivity of iron at Earth's core conditions. *Nature* 534, 95–98, <http://dx.doi.org/10.1038/nature17957>.
- Perdew, J.P., Burke, K., Ernzerhof, M., 1996. Generalized gradient approximation made simple. *Phys. Rev. Lett.* 77, 3865–3868, <http://dx.doi.org/10.1103/PhysRevLett.77.3865>.
- Poirier, J.-P., 1994. Light elements in the Earth's outer core: a critical review. *Phys. Earth Planet. Inter.* 85, 319–337, [http://dx.doi.org/10.1016/0031-9201\(94\)90120-1](http://dx.doi.org/10.1016/0031-9201(94)90120-1).
- Posner, E.S., Rubie, D.C., Frost, D.J., Steinle-Neumann, G., 2017a. Experimental determination of oxygen diffusion in liquid iron at high pressure. *Earth Planet. Sci. Lett.* 464, 116–123, <http://dx.doi.org/10.1016/j.epsl.2017.02.020>.

Please cite this article in press as: Wagle F, et al. Resistivity saturation in liquid iron–light-element alloys at conditions of planetary cores from first principles computations. *C. R. Geoscience* (2018), <https://doi.org/10.1016/j.crte.2018.05.002>

- Posner, E.S., Rubie, D.C., Frost, D.J., Vlček, V., Steinle-Neumann, G., 2017b. High  $P$ - $T$  experiments and first principles calculations of the diffusion of Si and Cr in liquid iron. *Geochim. Cosmochim. Acta* 203, 323–342, <http://dx.doi.org/10.1016/j.gca.2017.01.024>.
- Posner, E.S., Steinle-Neumann, G., Vlček, V., Rubie, D.C., 2017c. Structural changes and anomalous self-diffusion of oxygen in liquid iron at high pressure. *Geophys. Res. Lett.* 44, 3526–3534, <http://dx.doi.org/10.1002/2017GL072926>.
- Pozzo, M., Alfè, D., 2016. Saturation of electrical resistivity of solid iron at Earth's core conditions. *SpringerPlus* 5, 256, <http://dx.doi.org/10.1186/s40064-016-1829-x>.
- Pozzo, M., Davies, C., Gubbins, D., Alfè, D., 2012. Thermal and electrical conductivity of iron at Earth's core conditions. *Nature* 485, 355–358, <http://dx.doi.org/10.1038/nature11031>.
- Pozzo, M., Davies, C., Gubbins, D., Alfè, D., 2013. Transport properties for liquid silicon-oxygen-iron mixtures at Earth's core conditions. *Phys. Rev. B* 87, 014110, <http://dx.doi.org/10.1103/PhysRevB.87.014110>.
- Recoules, V., Crocombette, J.-P., 2005. Ab initio determination of electrical and thermal conductivity of liquid aluminum. *Phys. Rev. B* 72, 104202, <http://dx.doi.org/10.1103/PhysRevB.72.104202>.
- Rivoldini, A., Van Holst, T., Verhoeven, O., 2009. The interior structure of Mercury and its core sulfur content. *Icarus* 201, 12–30, <http://dx.doi.org/10.1016/j.icarus.2008.12.020>.
- Rückriemen, T., Breuer, D., Spohn, T., 2015. The Fe snow regime in Ganymede's core: a deep-seated dynamo below a stable snow zone. *J. Geophys. Res.* 120, 1095–1118, <http://dx.doi.org/10.1002/2014JE004781>.
- Sanloup, C., Guyot, F., Gillet, P., Fei, Y., 2002. Physical properties of liquid Fe alloys at high pressure and their bearings on the nature of metallic planetary cores. *J. Geophys. Res. Solid Earth* 107, 2272, <http://dx.doi.org/10.1029/2001JB000808>.
- Seagle, C.T., Cottrell, E., Fei, Y., Hummer, D.R., Prakapenka, V.B., 2013. Electrical and thermal transport properties of iron and iron-silicon alloy at high pressure. *Geophys. Res. Lett.* 40, 5377–5381, <http://dx.doi.org/10.1002/2013GL057930>.
- Secco, R.A., Schlössin, H.H., 1989. The electrical resistivity of solid and liquid Fe at pressures up to 7 GPa. *J. Geophys. Res.* 94, 5887–5894, <http://dx.doi.org/10.1029/JB094iB05p05887>.
- Stacey, F.D., Anderson, O.L., 2001. Electrical and thermal conductivities of Fe-Ni-Si alloy under core conditions. *Phys. Earth Planet. Inter.* 124, 153–162, [http://dx.doi.org/10.1016/S0031-9201\(01\)00186-8](http://dx.doi.org/10.1016/S0031-9201(01)00186-8).
- Stacey, F.D., Loper, D.E., 2007. A revised estimate of the conductivity of iron alloy at high pressure and implications for the core energy balance. *Phys. Earth Planet. Inter.* 161, 13–18, <http://dx.doi.org/10.1016/j.pepi.2006.12.001>.
- Suehiro, S., Ohta, K., Hirose, K., Morard, G., Ohishi, Y., 2017. The influence of sulfur on the electrical resistivity of hcp iron: implications for the core conductivity of Mars and Earth. *Geophys. Res. Lett.* 44, 8254–8259, <http://dx.doi.org/10.1002/2017GL074021>.
- Torrent, M., Jollet, F., Bottin, F., Zérah, G., Gonze, X., 2008. Implementation of the projector augmented-wave method in the abinit code: application to the study of iron under pressure. *Comput. Mater. Sci.* 42, 337–351, <http://dx.doi.org/10.1016/j.commatsci.2007.07.020>.
- Tsuno, K., Frost, D.J., Rubie, D.C., 2013. Simultaneous partitioning of silicon and oxygen into the Earth's core during early Earth differentiation. *Geophys. Res. Lett.* 40, 66–71, <http://dx.doi.org/10.1029/2012GL054116>.
- Vlček, V., de Koker, N., Steinle-Neumann, G., 2012. Electrical and thermal conductivity of al liquid at high pressures and temperatures from ab initio computations. *Phys. Rev. B* 85, 184201, <http://dx.doi.org/10.1103/PhysRevB.85.184201>.
- Wagle, F., Steinle-Neumann, G., 2018. Electrical resistivity discontinuity of iron along the melting curve. *Geophys. J. Int.* 213, 237–243, <http://dx.doi.org/10.1093/gji/ggx526>.
- Wagle, F., Steinle-Neumann, G., de Koker, N., 2018. Saturation and negative temperature coefficient of electrical resistivity in liquid iron-sulfur alloys at high densities from first principles calculations. *Phys. Rev. B* 97, 094307, <http://dx.doi.org/10.1103/PhysRevB.97.094307>.
- Wicht, J., 2002. Inner-core conductivity in numerical dynamo simulations. *Phys. Earth Planet. Inter.* 132, 281–302, [http://dx.doi.org/10.1016/S0031-9201\(02\)00078-X](http://dx.doi.org/10.1016/S0031-9201(02)00078-X).
- Ziman, J.M., 1961. A theory of the electrical properties of liquid metals. I: The monovalent metals. *Philos. Mag.* 6, 1013–1034, <http://dx.doi.org/10.1080/14786436108243361>.
- van Zytveld, J.B., 1980. Electrical resistivities of liquid transition metals. *J. Phys. (Paris)* 41, C8, <http://dx.doi.org/10.1051/jphyscol:19808126>.

Please cite this article in press as: Wagle F, et al. Resistivity saturation in liquid iron–light-element alloys at conditions of planetary cores from first principles computations. *C. R. Geoscience* (2018), <https://doi.org/10.1016/j.crte.2018.05.002>

**5 Wagle *et al.* (2018),  
Phys. Rev. B 97, 094307**

## Saturation and negative temperature coefficient of electrical resistivity in liquid iron-sulfur alloys at high densities from first-principles calculations

Fabian Wagle and Gerd Steinle-Neumann

*Bayerisches Geoinstitut, Universität Bayreuth, 95440 Bayreuth, Germany*

Nico de Koker

*School of Geosciences, University of the Witwatersrand, Private Bag 3, 2050 Wits, South Africa*



(Received 17 January 2018; published 28 March 2018)

We report results on electronic transport properties of liquid Fe-S alloys at conditions of planetary cores, computed using first-principle techniques in the Kubo-Greenwood formalism. We describe a combined effect of resistivity saturation due to temperature, compression, and chemistry by comparing the electron mean free path from the Drude response of optical conductivity to the mean interatomic distance. At high compression and high sulfur concentration the Ioffe-Regel condition is satisfied, and the temperature coefficient of resistivity changes sign from positive to negative. We show that this happens due to a decrease in the  $d$  density of states at the Fermi level in response to thermal broadening.

DOI: [10.1103/PhysRevB.97.094307](https://doi.org/10.1103/PhysRevB.97.094307)

### I. INTRODUCTION

An understanding of the stability of planetary magnetic fields and the thermal evolution of terrestrial planets is closely related to the characterization of electronic transport properties of liquid Fe and Fe alloys that make up the dynamo-active portions of their cores. Recent years have seen significant progress in this direction, and both electrical ( $\sigma$ ) and thermal ( $\lambda_{\text{th}}$ ) conductivities have been determined at high pressure  $P$  and high temperature  $T$  by means of *ab initio* simulations [1–3] and experiments [4–8]. While a consensus has emerged that  $\sigma$  at conditions of planetary cores is significantly higher than previously thought [9,10], there is considerable controversy on values of  $\lambda_{\text{th}}$  [1–3,11,12] that includes a discussion of the validity of the Wiedemann-Franz law that relates both electronic transport quantities.

For the Earth's core, Fe is likely alloyed with silicon and/or oxygen [13,14], which have therefore been the focus of previous studies [1,3–5]. By contrast, in the cores of Mercury and Mars, sulfur is expected to be the dominant light element alloying with iron [15,16]: It is cosmically abundant and shows a high solubility in liquid iron due to its compatibility in electronic structure and the similar atomic size of Fe and S [17,18]. In the Earth's core, sulfur is unlikely to play an important role as the giant Moon-forming impact has probably led to the loss of this moderately volatile element [19].

The observed decrease in conductivity ( $\sigma \propto 1/T$ ) of liquid metals in experiments [20,21] and computations, also at high  $P$  [1], is consistent with the Bloch-Grüneisen law for solids above the Debye temperature  $\theta_D$  that describes the shortening of the electron mean free path  $x_{\text{eff}} \propto 1/T$ . In the quasi-free-electron model, scattering events in the liquid occur due to the interaction of electrons with atomic potentials [22]. For this scattering mechanism, the interatomic distance sets a lower bound for the mean free path, which is known as the Ioffe-Regel condition [23], leading to saturation. Resistivity

saturation has been found to be an important factor in highly resistive transition metals and their alloys [24], in which  $x_{\text{eff}}$  is already short due to the following static and dynamic effects:

(i) Experiments at ambient  $P$  reveal that a high concentration of impurities can shorten  $x_{\text{eff}}$  sufficiently since the alloying element introduces compositional disorder [25]. Chemically induced saturation continues to take place at high  $P$ , as has been shown for the Fe-Si-Ni system [6]. Gomi *et al.* [6] combined diamond-anvil-cell experiments with first-principles calculations and showed that Matthiessen's rule [26] breaks down close to the saturation limit.

(ii) Increasing thermal disorder also induces saturation, as has been demonstrated by analyzing the temperature coefficient of resistivity (TCR) in NiCr thin films [25]. Recent computations [27] observe a sublinear trend of  $\rho(T) = 1/\sigma$  for hexagonal close packed (hcp) iron at  $P$  of the Earth's inner core.

(iii) In addition to impurities and  $T$ , pressure can lead to saturation. This has been shown for the Fe-Si system in the multi-anvil press [28].

Since electrical conductivity measurements of liquid iron and its alloys at conditions of the Earth's core are challenging [29], high- $P$  studies extrapolate ambient- $T$  [5,8] or high- $T$  experiments [7] for the solid to the melting temperature and the liquid phase, accounting for saturation by a parallel resistor model. The extrapolation of their models supports low values of  $\rho$  for the Earth's core, consistent with computational studies [1–3]. Here, we investigate the electronic transport properties for liquid iron-sulfur alloys based on first-principles simulations to complement the existing results for Fe [1,2] and the Fe-O-Si system [1,3] and to compare to recent experiments in the Fe-Si-S system [8]. The first-principles approach also provides the opportunity to explore resistivity saturation in terms of the Ioffe-Regel condition and the TCR by means of the electronic structure.

## II. METHODS

We generate representative liquid configurations using density-functional-theory-based molecular dynamics (DFT-MD) simulations, for which we then perform electronic linear response calculations to obtain transport properties.

### A. Molecular dynamics simulations

DFT-MD simulation cells contain 128 atoms, and the calculations are performed in the  $N$ - $V$ - $T$  ensemble using the plane-wave code VASP [30–32]. Cubic cells in a volume range between 7.09 and 11.82 Å<sup>3</sup>/atom (six equally spaced volumes, covering the  $P$  range of the Earth) and sulfur contents of 12.5 (Fe<sub>7</sub>S) and 25 at % (Fe<sub>3</sub>S; ~7.6 and ~16 wt %) are set up by randomly replacing Fe atoms in molten configurations from previous simulations [1]. At 8.28 Å<sup>3</sup>/atom we also set up Fe<sub>15</sub>S and Fe<sub>27</sub>S<sub>5</sub> compositions to consider the dependence of resistivity on composition in more detail. Atomic coordinates are updated using a time step of 1 fs, and  $T$  is controlled by the Nosé thermostat [33], with  $T$  between 2000 and 8000 K. At each time step, the electron density is computed using the projector augmented-wave (PAW) method [34] with the Perdew-Burke-Ernzerhof exchange-correlation functional [35] and a plane-wave cutoff energy of 400 eV. Electronic states are occupied according to Fermi-Dirac statistics at  $T$  of the thermostat. Brillouin zone sampling is restricted to the zone center. After equilibration of  $P$ ,  $T$ , and the total energy  $E$  is achieved (typically after a few hundred femtoseconds), the DFT-MD simulations are continued for at least 15 ps.

### B. Resistivity calculations

The kinetic coefficients in linear response to an electric field  $\mathbf{E}$  and a thermal gradient  $\nabla T$  build up the Onsager matrix  $\mathcal{L}_{ij}$  [36],

$$\mathbf{j}_{\text{el}} = \mathcal{L}_{11}\mathbf{E} + \mathcal{L}_{12}\nabla T, \quad (1)$$

$$\mathbf{j}_{\text{th}} = \mathcal{L}_{21}\mathbf{E} + \mathcal{L}_{22}\nabla T, \quad (2)$$

where  $\mathbf{j}_{\text{el}}$  and  $\mathbf{j}_{\text{th}}$  are electrical and thermal current densities, respectively. Electrical conductivity and the electronic contribution to thermal conductivity are then

$$\sigma = \mathcal{L}_{11} \quad (3)$$

and

$$\lambda_{\text{th}}^{\text{el}} = \frac{1}{e^2 T} \left( \mathcal{L}_{22} - \frac{\mathcal{L}_{12}^2}{\mathcal{L}_{11}} \right). \quad (4)$$

We extract at least six uncorrelated snapshots from the MD simulations (i.e., separated by time periods greater than that required for the velocity autocorrelation function to decay to zero) and compute Kohn-Sham wave functions  $\psi_k$ , their energy eigenvalues  $\epsilon_k$ , and the Cartesian gradients of the Hamiltonian with respect to a shift in wave vector  $\partial\mathcal{H}/\partial\mathbf{k}$  using the ABINIT software package [37–39]. From those, the frequency-dependent Onsager matrix elements are calculated

with the Kubo-Greenwood equations,

$$\begin{aligned} \mathcal{L}_{ij} = & (-1)^{i+j} \frac{\hbar e^2}{V_{\text{cell}}} \sum_{k',k} [f(\epsilon_{k'}) - f(\epsilon_k)] \delta(\epsilon_{k'} - \epsilon_k - \hbar\omega) \\ & \times \langle \psi_k | \hat{v} | \psi_{k'} \rangle \langle \psi_{k'} | \hat{v} | \psi_k \rangle (\epsilon_{k'} - \mu_e)^{i-1} (\epsilon_k - \mu_e)^{j-1}, \end{aligned} \quad (5)$$

as implemented in the CONDUCTI module of ABINIT [40]. In Eq. (5),  $\hbar$  denotes the reduced Planck constant,  $e$  is the elementary charge,  $V_{\text{cell}}$  is the cell volume,  $\omega$  is the frequency of the external field,  $\hat{v} = 1/\hbar \cdot \partial\mathcal{H}/\partial\mathbf{k}$  is the velocity operator, and  $\mu_e$  is the electronic chemical potential.

By fitting the Drude formula for optical conductivity

$$\Re[\sigma(\omega)] = \frac{\sigma_0}{1 + (\omega\tau)^2} \quad (6)$$

to the Kubo-Greenwood results for each snapshot, we extract the dc limit of conductivity  $\sigma_0$  (used without subscript elsewhere) and effective relaxation time  $\tau$ . Thermal conductivity is extrapolated linearly to the limit  $\omega \rightarrow 0$  over a  $\hbar\omega$  range of 2 eV. We average  $\sigma$ ,  $\tau$ , and  $\lambda_{\text{th}}$  over the snapshots and take one standard deviation as uncertainty. Calculations with denser grids of  $2 \times 2 \times 2$  and  $3 \times 3 \times 3$   $k$  points show that  $\sigma(\omega)$  is sufficiently converged (to within 3%) in calculations using a single  $k$  point (see Fig. S1 in the Supplemental Material [41]).

The resulting  $\rho(V, T)$  and  $\lambda_{\text{th}}(V, T)$  are fit with a physically motivated closed expression (Appendix A) to interpolate between results and extrapolate to conditions not investigated.

### C. Electron density of states

We compute the site-projected and angular-momentum-decomposed electron densities of states (DOSs) with the tetrahedron method [42,43], using a nonshifted  $2 \times 2 \times 2$   $k$ -point grid with small energy increments of  $1.4 \times 10^{-3}$  eV. The radii of the atomic spheres, in which the angular-momentum projections are evaluated, have been chosen to be space filling and proportional to the radii of the respective PAW spheres [34]. The DOS is computed for the same snapshots as those used for the evaluation of the Kubo-Greenwood equations and re-binned with an energy window of  $\sim 1/2k_B T$  to resolve  $T$ -dependent features in the vicinity of the Fermi energy  $E_F$ . This results in a strongly varying DOS which is independent of the smearing parameter.

## III. RESULTS AND DISCUSSION

### A. Electrical resistivity

For the low-impurity composition Fe<sub>7</sub>S, we find a dependence of  $\rho$  on  $V$  and  $T$  similar to that predicted in previous studies on pure Fe, Fe-Si, and Fe-O systems [1] (Fig. 1 and Tables S1 and S2 in the Supplemental Material [44,45]). Resistivity increases with  $V$  and  $T$  and can be reasonably well described by a linear  $T$  dependence above  $\Theta_D$  ( $\sim 1000$  K at low compression based on the equation-of-state parameters; see Appendix B and Table S3 in the Supplemental Material [46]), consistent with Bloch-Grüneisen theory. With decreasing  $V$ ,  $\Theta_D$  increases based on the thermodynamic parameters from our DFT-MD simulation, and values for  $\rho$

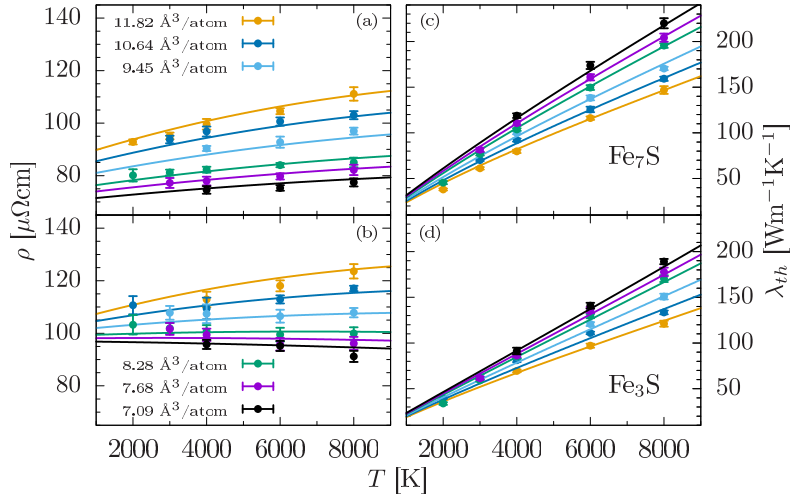


FIG. 1. Electronic transport properties of liquid Fe-S alloys as a function of temperature. The temperature coefficient of electrical resistivity of liquid (a) Fe<sub>7</sub>S and (b) Fe<sub>3</sub>S decreases with compression due to saturation. For Fe<sub>3</sub>S, the temperature coefficient of resistivity becomes negative along the smallest  $V$  isochores. Solid lines represent the best fit of Eq. (A1) to resistivity. The electronic contribution to thermal conductivity of liquid (c) Fe<sub>7</sub>S and (d) Fe<sub>3</sub>S. Solid lines have been calculated from the best fits to  $\rho(V, T)$  [Eq. (A1)] and the effective Lorenz number  $L(V, T)$  [Eq. (A5)]. Tabulated values for  $\rho$ ,  $\lambda_{th}$ , and  $L$  are given in Tables S1 and S2 in the Supplemental Material [44,45].

decrease. This behavior is well captured with the resistivity model in Appendix A.

Absolute resistivities for both compositions in the Fe-S system are similar to those for Fe-Si with the same light-element concentration [1] and higher than those for pure Fe and in the Fe-O system [1,2]. This is in contrast to experimental work [8] that estimated  $\rho$  for the solid phase in a ternary Fe-Si-S system and calculated the S impurity resistivity by using Matthiessen's rule based on previous experimental results for Fe [7] and Fe-Si [6]. Suehiro *et al.* [8] find that the influence of S on resistivity is significantly less than that of Si [6]. The experiments had to rely on this indirect determination of resistivity reduction due to sulfur, as S is hardly soluble in solid Fe at ambient  $P$ , and it is therefore difficult to synthesize a homogeneous phase as a starting material in experiments [47–50]. Further, Matthiessen's rule, applied in the analysis of the data, does not hold for systems with saturated resistivity [6].

For higher sulfur concentration, we find that  $\rho$  increases (Fig. 1; see Fig. S2 in the Supplemental Material [51]) and that the Bloch-Grüneisen behavior breaks down. The temperature coefficient of resistivity decreases with compression, up to the extreme case where it changes sign and becomes negative for Fe<sub>3</sub>S at the smallest two volumes we consider.

Negative TCRs have been observed for liquid and amorphous solid metals, for which the maximum momentum change of a scattered electron  $2k_F$  falls in the region close to the principle peak of the structure factor  $S(q)$ , as in the case of metals with two valence electrons, e.g., Eu, Yb, and Ba with a  $6s^2$  valence configuration [52], and Cu-Zr metallic glasses [53]. It is one of the great successes of Ziman theory for the resistivity of liquid metals [22,54] to explain the negative TCR in these systems. Ziman theory cannot account for the

negative TCR that we predict for Fe<sub>3</sub>S at high compression. Because for iron and the other Fe alloys considered by de Koker *et al.* [1]  $2k_F$  is near the first minimum in  $S(q)$  (Fig. S3 in the Supplemental Material [55]), thermal broadening of the structure factor will lead to positive TCR over the entire compression range. This suggests that the negative TCR is a secondary effect, driven by changes in electronic structure (Sec. III C) that are only noticeable once resistivity saturation is reached by compression and impurities simultaneously.

### B. Mean free path

In order to understand the effect of resistivity saturation from a semiclassical picture of electron transport, we calculate the effective electron mean free path as  $x_{eff} = v_F \tau$ , where  $v_F = (\hbar/m)(3\pi^2 n_{eff})^{1/3}$  is the Fermi velocity,  $n_{eff} = (m\sigma)/(e^2\tau)$  is the effective number density of conduction electrons, and  $m$  is the electron mass. Figure 2 reveals three distinctive features:

(i) For ambient  $P$  volumes ( $V = 11.82 \text{ \AA}^3/\text{atom}$ ),  $x_{eff}$  approaches the mean interatomic distance asymptotically with increasing  $T$ , consistent with dynamic resistivity saturation [25,27].

(ii) At the lowest cell  $V$  considered ( $V = 7.09 \text{ \AA}^3/\text{atom}$ ), the  $T$  dependence of  $x_{eff}$  vanishes within uncertainty. In addition,  $x_{eff}$  becomes shorter than at lower compression due to the increased density of scattering centers. At first glance, this observation appears to be inconsistent with the fact that  $\rho$  decreases with compression but can be understood in terms of electronic structure (Sec. III C).

(iii) With increasing sulfur concentration,  $x_{eff}$  decreases significantly. This reflects the expected behavior of an increased probability of impurity-caused scattering.

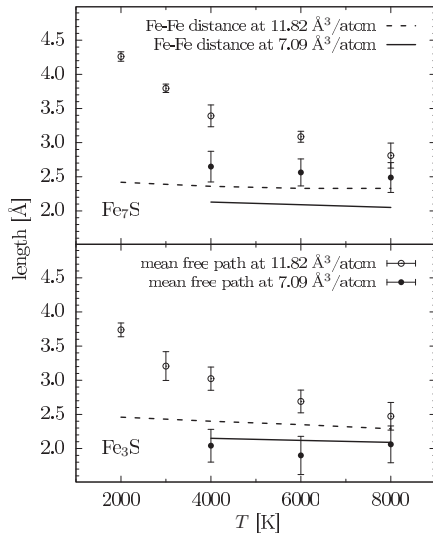


FIG. 2. Electron mean free path for liquid  $\text{Fe}_7\text{S}$  (top) and  $\text{Fe}_3\text{S}$  (bottom) for two cell volumes (near ambient  $P$  and largest compression) as a function of temperature, obtained by a Drude fit to optical conductivity [Eq. (6)]. The mean free path approaches the interatomic distance (solid lines, first peak position of the partial radial distribution function) with increasing compression and impurity concentration. For  $\text{Fe}_3\text{S}$  at the smallest cell volume, the Ioffe-Regel condition is reached.

For the highest compression the Ioffe-Regel condition is reached for  $\text{Fe}_3\text{S}$  as  $x_{\text{eff}}$  becomes equal to the mean interatomic distance within uncertainty.

### C. Electronic structure

Most of the electric current in transition metals is transported by  $s$  electrons, which can scatter into  $d$  states with a far lower Fermi velocity [56]. Partially filled  $d$  bands with a high DOS at the Fermi level lead to a high probability of  $s$ - $d$  scattering events, which dominate resistivity over  $s$ - $s$  processes [57].

Site-projected and angular-momentum-decomposed local densities of states (LDOSs) show similar changes in response to compression and  $T$  (Figs. S4 and S5 of the Supplemental Material [58,59]). Generally, peaks broaden, and the Fe  $d$  LDOS at  $E_F$  decreases, resulting in fewer states available for  $s$  electrons to scatter into. The response of the electronic structure to compression is a dominant feature as dispersion of electronic bands increases significantly due to stronger interactions [60] (Fig. S4 in the Supplemental Material [58]).

For increasing  $T$ , changes in the DOS are less pronounced (Fig. S5 in the Supplemental Material [59]) and reflect dynamic short-range changes in the liquid structure that can lead to smaller interatomic distances [61] that are also expressed by thermal pressure [27]. This is a small effect, and the negative TCR can be observed only when compression and chemical saturation in the system have been reached.

Electronic states of iron dominate the DOS of the liquid Fe-S alloys near  $E_F$ . The densities of states for Fe and  $\text{Fe}_3\text{S}$  are quite similar at the same  $V$  and  $T$  (Figs. S4 and S5 in the Supplemental Material [58,59]), and the broadenings in the vicinity of  $E_F$  due to compression and  $T$ , respectively, are almost identical. Therefore, sulfur contributes to the overall resistivity behavior in the Fe-S systems only by shortening  $x_{\text{eff}}$  through impurity scattering, as discussed in Sec. III B (Fig. 2). In comparison to silicon and oxygen, sulfur appears to be more efficient in doing so due to its similar atomic size and the efficient bonding with iron, resulting in high Fe-S coordination numbers [17].

### D. Thermal conductivity

Since lattice vibrations play only a minor role in heat transport through metals, the electronic contribution to thermal conductivity  $\lambda_{\text{th}}^{\text{el}}$  represents total conductivity  $\lambda_{\text{th}}$  to a good approximation [26]. Similar to the results for  $\rho$ , we find the Kubo-Greenwood values for  $\lambda_{\text{th}}$  (Fig. 1) to be consistent with the ones for liquid Fe-Si alloys and somewhat larger than those of Fe-O liquids from previous computations with the same light-element concentrations [1]. Contrary to electrical resistivity, we do not see any sign of saturation in  $\lambda_{\text{th}}$ , putting the validity of the Wiedemann-Franz law with a constant value of the Lorenz number  $L_0 \approx 2.44 \text{ W}\Omega/\text{K}^2$  from Drude-Sommerfeld theory in question. Indeed, thermal conductivity is significantly overestimated by using  $L_0$  and the resistivity model (Appendix A) compared to the values computed directly with the Kubo-Greenwood equations [Eq. (5)].

Recently, electron-electron scattering has been suggested to contribute significantly to  $\lambda_{\text{th}}$  of hcp iron at high  $P$  but not to  $\rho$  [12], an effect that is ignored in the independent electron approximation of the Kubo-Greenwood approach. However, it remains an open question to what degree this contribution affects thermally disordered systems. Electronic transport critically depends on the electronic structure at the Fermi level, which is quite different for a high-density liquid at high  $T$  compared to a perfect crystal. Until the influence of electron-electron scattering on transport properties of disordered  $3d$  transition metals and their alloys is better understood, values for  $\lambda_{\text{th}}$  from the Kubo-Greenwood approach should be used with caution.

### E. Application to planetary interiors

We convert resistivity values and fits in  $V$ - $T$  space (Appendix A and Table I) to  $\rho(P, T)$  by using the self-consistently obtained equations of state for  $\text{Fe}_7\text{S}$  and  $\text{Fe}_3\text{S}$  (Appendix B and Fig. S6 and Table S3 in the Supplemental Material [46,62]). Resistivity values for  $\text{Fe}_7\text{S}$  and  $\text{Fe}_3\text{S}$  (Fig. 3) are substantially larger than the corresponding ones for pure iron. While resistivities for  $\text{Fe}_7\text{S}$  along different isotherms continue to show distinctive  $P$  trends, they become indistinguishable for  $\text{Fe}_3\text{S}$  at high  $P$  due to the combined saturation effects discussed in Sec. III B. For  $\text{Fe}_3\text{S}$ , resistivity saturates at  $\sim 100 \mu\Omega \text{ cm}$ , a value which remains approximately constant and  $T$  independent over the  $P$  range of the Earth's outer core, similar to the behavior of  $\text{Fe}_3\text{Si}$  [1].

TABLE I. Fit parameters of the models for  $\rho(V, T)$  [Eqs. (A2)–(A4)] and  $L(V, T)$  [Eq. (A5)] for liquid Fe, Fe<sub>7</sub>S, and Fe<sub>3</sub>S. Uncertainties of the fit parameters are large and exceed their values in most cases.

	Fe	Fe <sub>7</sub> S	Fe <sub>3</sub> S
$\rho_{0R}$ ( $\mu\Omega$ cm)	75.10	89.03	105.2
$\rho_{1R}$ ( $\mu\Omega$ cm)	21.48	12.73	12.06
$a$	0.792	0.389	0.124
$b$	1.479	1.804	2.686
$c$ ( $\mu\Omega$ cm)	747.2	2077	6609
$d$ ( $\mu\Omega$ cm)	1405	2829	2910
$L_R$ ( $W \Omega/K^2$ )	2.005	2.105	1.991
$e$	-0.097	-0.106	-0.228
$f$	0.041	-0.027	-0.022

There is a large discrepancy between our results and the high- $T$  extrapolation of experimental resistivity [8] reported along model adiabats in the cores of Mars and the Earth [49,63]. Despite the similar compositions between the work presented here and the experiments (which fall between Fe<sub>3</sub>S and Fe<sub>7</sub>S, towards the higher sulfur concentration), the experimental profile for Earth's core shows significantly lower values, more consistent with the Kubo-Greenwood results for pure Fe [1,2]. Model values of Suehiro *et al.* [8] in the  $P$  range of the Martian

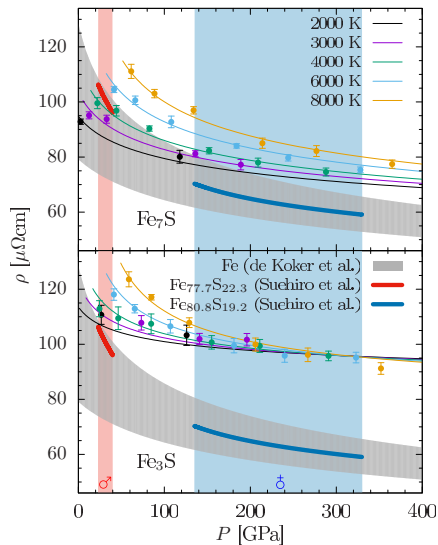


FIG. 3. Electrical resistivity of liquid Fe-S alloys as a function of pressure for Fe<sub>7</sub>S (top) and Fe<sub>3</sub>S (bottom). Solid lines are best fits of a parallel-resistor model to  $\rho(V, T)$  [Eq. (A1)] converted from  $V-T$  to  $P-T$  conditions using the equation-of-state fits (Appendix B). Results from an experimental study [8] along a model adiatherm (red line) and geotherm (blue line) as well as computational results for pure Fe [1] between 2000 and 8000 K (gray area) are included for comparison.

core are closer to our results (Fig. 3), but the slope  $(\partial\rho/\partial P)_S$  in the model based on experiments is significantly larger than in our work.

A small contribution to the difference between the experimental data and our results may come from the fact that the experiments have been performed for the solid and the simulations for the liquid, and resistivity increases discontinuously across the melting point for metals and their alloys at both ambient [64] and high  $P$  [65–68]. However, based on the Ziman approximation [22], this difference is expected to decrease with  $P$  if the density and compressibility of the coexisting solid and liquid phases become more similar. For pure iron, for example, this discontinuity is likely to become negligible at conditions of the Earth's core [69]. Rather than the difference decreasing with  $P$  as expected, it increases between the experimental data [8] and our computational results (Fig. 3).

#### IV. CONCLUSIONS

We presented electronic transport properties of liquid Fe-S alloys from DFT-MD simulations at conditions relevant for the cores of terrestrial planets. We find absolute values of electrical resistivity and thermal conductivity to be consistent with those of other Fe-light-element alloys reported in previous work [1,70], ranging from 75 to 125  $\mu\Omega$  cm and 30 to 220  $W m^{-1} K^{-1}$ . Fe alloys with low S content exhibit a positive TCR along isochores, which gradually decreases upon compression. We show that this is due to a compression-induced resistivity saturation by comparing the electron mean free path to interatomic distances. For high S concentrations (Fe<sub>3</sub>S), the mean free path is further shortened by increased impurity scattering, sufficient to reach the Ioffe-Regel condition at the lowest volumes, resulting in a saturation of resistivity. At these conditions the TCR becomes negative, which is caused by a decrease in the Fe  $d$  density of states at the Fermi level.

For applications in planetary physics, we provide models for  $\rho(V, T)$  and  $\lambda_{th}(V, T)$  (Appendix A), which, in combination with a self-consistent thermodynamic equation of state (Appendix B), can be translated to the  $P-T$  conditions of planetary cores.

#### ACKNOWLEDGMENTS

This work was supported by the Deutsche Forschungsgemeinschaft (German Science Foundation, DFG) in the Focus Program “Planetary Magnetism” (SPP 1488) with Grant No. STE1105/10-1 and Research Unit “Matter under Planetary Interior Conditions” (FOR 2440) with Grant No. STE1105/13-1. Computing and data resources for the current project were provided by the Leibniz Supercomputing Centre of the Bavarian Academy of Sciences and the Humanities. We greatly acknowledge informative discussions with V. Recoules and M. Preising on the electron density-of-states evaluation and helpful comments by an anonymous reviewer.

### APPENDIX A: MODEL FOR ELECTRICAL AND THERMAL CONDUCTIVITY

We describe the resistivity behavior  $\rho(V, T)$  with a parallel-resistor model:

$$\frac{1}{\rho(V, T)} = \frac{1}{\rho_{\text{BG}}(V, T)} + \frac{1}{\rho_{\text{sat}}(V)} + \frac{1}{\rho_{\text{el}}(T)}, \quad (\text{A1})$$

where

$$\rho_{\text{BG}} = \rho_0 \left( \frac{V}{V_0} \right)^a + \rho_1 \left( \frac{V}{V_0} \right)^b \frac{T}{T_0} \quad (\text{A2})$$

is the empirical expression used by de Koker *et al.* [1] based on the Bloch-Grüneisen formula.

$$\rho_{\text{sat}} = c \left( \frac{V}{V_0} \right)^{\frac{1}{3}} \quad (\text{A3})$$

is a term accounting for resistivity saturation, and

$$\rho_{\text{el}} = d \frac{T_0}{T} \quad (\text{A4})$$

describes the effect of thermal broadening of the DOS. The assumptions entering equations (A1)–(A4) are as follows:

(i) Sources of resistivity contributions in Eq. (A1) are independent, and therefore, conductivities are additive.

(ii) In the limit of high  $T$ , the Bloch-Grüneisen formula is linear in  $T$ . Both residual resistivity [first term in Eq. (A2)] and the material-dependent prefactor of the second term are well described by a power law in  $V/V_0$ .

(iii) Saturation resistivity [Eq. (A3)] is proportional to interatomic distance and therefore increases  $\propto (V/V_0)^{1/3}$ . This is consistent with the saturation resistivities for pure Fe reported by Ohta *et al.* [7].

(iv) Since the effect of thermal broadening on the DOS at  $E_F$  can be attributed to a resistivity contribution due to thermal pressure (Fig. S5 in the Supplemental Material [59]), we describe  $\rho_{\text{el}}$  in Eq. (A4) as inversely proportional to  $T$ .

Rather than fitting a model for  $\lambda_{\text{th}}$  directly, we compute an effective Lorenz number  $L$  at each simulation and fit  $L(V, T)$  as [1]

$$L(V, T) = L_R \left( \frac{V}{V_0} \right)^e \left( \frac{T}{T_0} \right)^f. \quad (\text{A5})$$

Fit parameters are listed in Table I.

### APPENDIX B: EQUATION-OF-STATE MODEL

In order to describe electronic transport properties as a function of  $P$  suitable for comparison to experiments and for applications in planetary models, we fit a thermodynamic model to the  $\text{Fe}_7\text{S}$  and  $\text{Fe}_3\text{S}$  results that is based on a separation of the Helmholtz energy in an ideal gas, electronic and excess term [71,72]. The volume dependence of the excess term is represented by Eulerian finite strain  $f$  with the exponent  $n = 2$  and a similarly reduced  $T$  term  $\Theta$  with the exponent  $m = 0.79$  and expansion orders  $\mathcal{O}_f = 3$  and  $\mathcal{O}_\Theta = 2$ , parameters that describe the results for liquid iron well [1]. Figure S6 in the Supplemental Material shows the quality of the fit for  $E$ ,  $P$ , and the electronic entropy  $S_{\text{el}}$  of the DFT-MD results [62]. Thermodynamic parameters at reference conditions are summarized in Table S3 of the Supplemental Material [46].

- 
- [1] N. de Koker, G. Steinle-Neumann, and V. Vlček, *Proc. Natl. Acad. Sci. USA* **109**, 4070 (2012).
- [2] M. Pozzo, C. Davies, D. Gubbins, and D. Alfè, *Nature (London)* **485**, 355 (2012).
- [3] M. Pozzo, C. Davies, D. Gubbins, and D. Alfè, *Phys. Rev. B* **87**, 014110 (2013).
- [4] C. T. Seagle, E. Cottrell, Y. Fei, D. R. Hummer, and V. B. Prakapenka, *Geophys. Res. Lett.* **40**, 5377 (2013).
- [5] H. Gomi, K. Ohta, K. Hirose, S. Labrosse, R. Caracas, M. J. Verstraete, and J. W. Hernlund, *Phys. Earth Planet. Inter.* **224**, 88 (2013).
- [6] H. Gomi, K. Hirose, H. Akai, and Y. Fei, *Earth Planet. Sci. Lett.* **451**, 51 (2016).
- [7] K. Ohta, Y. Kuwayama, K. Hirose, K. Shimizu, and Y. Ohishi, *Nature (London)* **534**, 95 (2016).
- [8] S. Suehiro, K. Ohta, K. Hirose, G. Morard, and Y. Ohishi, *Geophys. Res. Lett.* **44**, 8254 (2017).
- [9] F. D. Stacey and O. L. Anderson, *Phys. Earth Planet. Inter.* **124**, 153 (2001).
- [10] F. D. Stacey and D. E. Loper, *Phys. Earth Planet. Inter.* **161**, 13 (2007).
- [11] Z. Konôpková, R. S. McWilliams, N. Gómez-Pérez, and A. F. Goncharov, *Nature (London)* **534**, 99 (2016).
- [12] L. V. Pourovskii, J. Mravlje, A. Georges, S. I. Simak, and I. A. Abrikosov, *New J. Phys.* **19**, 073022 (2017).
- [13] K. Tsuno, D. J. Frost, and D. C. Rubie, *Geophys. Res. Lett.* **40**, 66 (2013).
- [14] J. Badro, J. P. Brodholt, H. Piet, J. Siebert, and F. J. Ryerson, *Proc. Natl. Acad. Sci. USA* **112**, 12310 (2015).
- [15] S. A. Hauck, J.-L. Margot, S. C. Solomon, R. J. Phillips, C. L. Johnson, F. G. Lemoine, E. Mazarico, T. J. McCoy, S. Padovan, S. J. Peale, M. E. Perry, D. E. Smith, and M. T. Zuber, *J. Geophys. Res.* **118**, 1204 (2013).
- [16] K. Lodders and B. Fegley, *Icarus* **126**, 373 (1997).
- [17] D. Alfè and M. J. Gillan, *Phys. Rev. B* **58**, 8248 (1998).
- [18] K. Hirose, S. Labrosse, and J. Hernlund, *Annu. Rev. Earth Planet. Sci.* **41**, 657 (2013).
- [19] G. Dreibus and H. Palme, *Geochim. Cosmochim. Acta* **60**, 1125 (1996).
- [20] J. B. van Zytveld, *J. Phys. Colloques* **41**, C8 (1980).
- [21] P. D. Desai, T. K. Chu, H. M. James, and C. Y. Ho, *Phys. Chem. Ref. Data* **13**, 1069 (1984).
- [22] J. M. Ziman, *Philos. Mag.* **6**, 1013 (1961).
- [23] A. F. Ioffe and A. R. Regel, in *Progress in Semiconductors*, Vol. 4, edited by A. F. Gibson, F. A. Kroger, and R. E. Burgess (London: Heywood, 1960), p 237.

- [24] O. Gunnarsson, M. Calandra, and J. E. Han, *Rev. Mod. Phys.* **75**, 1085 (2003).
- [25] J. H. Mooij, *Phys. Status Solidi A* **17**, 521 (1973).
- [26] N. W. Ashcroft and N. D. Mermin, *Solid State Physics* (Saunders College, Philadelphia, 1976).
- [27] M. Pozzo and D. Alfè, *SpringerPlus* **5**, 256 (2016).
- [28] S. Kiarasi and R. A. Secco, *Phys. Status Solidi B* **252**, 2034 (2015).
- [29] D. Dobson, *Nature (London)* **534**, 45 (2016).
- [30] G. Kresse and J. Hafner, *Phys. Rev. B* **47**, 558(R) (1993).
- [31] G. Kresse and J. Furthmüller, *Comput. Mater. Sci.* **6**, 15 (1996).
- [32] G. Kresse and J. Furthmüller, *Phys. Rev. B* **54**, 11169 (1996).
- [33] S. Nosé, *J. Chem. Phys.* **81**, 511 (1984).
- [34] G. Kresse and D. Joubert, *Phys. Rev. B* **59**, 1758 (1999).
- [35] J. P. Perdew, K. Burke, and M. Ernzerhof, *Phys. Rev. Lett.* **77**, 3865 (1996).
- [36] L. Onsager, *Phys. Rev.* **37**, 405 (1931).
- [37] X. Gonze, *Phys. Rev. B* **55**, 10337 (1997).
- [38] X. Gonze, B. Amadon, P.-M. Anglade, J.-M. Beuken, F. Bottin, P. Boulanger, F. Bruneval, D. Caliste, R. Caracas, M. Côté, T. Deutsch, L. Genovese, P. Ghosez, M. Giantomassi, S. Goedecker, D. R. Hamann, P. Hermet, F. Jollet, G. Jomard, S. Leroux, M. Mancini, S. Mazevet, M. J. T. Oliveira, G. Onida, Y. Pouillon, T. Rangel, G.-M. Rignanese, D. Sangalli, R. Shaltaf, M. Torrent, M. J. Verstraete, G. Zerah, and J. W. Zwanziger, *Comput. Phys. Commun.* **180**, 2582 (2009).
- [39] M. Torrent, F. Jollet, F. Bottin, G. Zerah, and X. Gonze, *Comput. Mater. Sci.* **42**, 337 (2008).
- [40] V. Recoules and J. P. Crocombette, *Phys. Rev. B* **72**, 104202 (2005).
- [41] See Fig. S1 in the Supplemental Material at <http://link.aps.org/supplemental/10.1103/PhysRevB.97.094307> for a convergence study of optical conductivity with respect to Brillouin zone sampling.
- [42] O. Jepsen and O. K. Andersen, *Phys. Rev. B* **29**, 5965 (1984).
- [43] G. Lehmann and M. Taut, *Phys. Status Solidi B* **54**, 469 (1972).
- [44] See Table S1 in the Supplemental Material for  $\rho$ ,  $\lambda_{th}$ , and  $L$  of  $\text{Fe}_7\text{S}$  as a function of  $V$ ,  $T$ , and  $P$ .
- [45] See Table S2 in the Supplemental Material for  $\rho$ ,  $\lambda_{th}$ , and  $L$  of  $\text{Fe}_3\text{S}$  as a function of  $V$ ,  $T$ , and  $P$ .
- [46] See Table S3 in the Supplemental Material for thermodynamic parameters of Fe,  $\text{Fe}_7\text{S}$  and  $\text{Fe}_3\text{S}$  from the equation-of-state fit according to the modified thermodynamic model described in Appendix B.
- [47] J. Li, Y. Fei, H. K. Mao, K. Hirose, and S. R. Shieh, *Earth Planet. Sci. Lett.* **193**, 509 (2001).
- [48] A. Stewart, M. Schmidt, W. Westrenen, and C. Liebske, *Science* **316**, 1323 (2008).
- [49] S. Kamada, E. Ohtani, H. Terasaki, T. Sakai, M. Miyahara, Y. Ohishi, and N. Hirao, *Earth Planet. Sci. Lett.* **359**, 26 (2012).
- [50] Y. Mori, H. Ozawa, K. Hirose, R. Simmyo, S. Tateno, G. Morard, and Y. Ohishi, *Earth Planet. Sci. Lett.* **464**, 135 (2017).
- [51] See Fig. S2 in the Supplemental Material for electrical resistivity as a function of sulfur content, which includes Ref. [73].
- [52] H.-J. Güntherodt, E. Hauser, H. U. Künzi, R. Evans, J. Evers, and E. Kaldis, *J. Phys. F* **6**, 1513 (1976).
- [53] Y. Waseda and H. S. Chen, *Phys. Status Solidi B* **87**, 777 (1978).
- [54] T. E. Faber and J. M. Ziman, *Philos. Mag.* **11**, 153 (1965).
- [55] See Fig. S3 in the Supplemental Material for thermal broadening of the static structure factor.
- [56] N. F. Mott, *Proc. R. Soc. London, Ser. A* **153**, 699 (1936).
- [57] N. F. Mott, *Philos. Mag.* **26**, 1249 (1972).
- [58] See Fig. S4 in the Supplemental Material for broadening of the electron density of states with decreasing cell volume.
- [59] See Fig. S5 in the Supplemental Material for broadening of the electron density of states with increasing temperature.
- [60] R. E. Cohen, L. Stixrude, and E. Wasserman, *Phys. Rev. B* **56**, 8575 (1997).
- [61] P. Hunt, M. Sprik, and R. Vuilleumier, *Chem. Phys. Lett.* **376**, 68 (2003).
- [62] See Fig. S6 in the Supplemental Material for the equation-of-state fit according to the modified thermodynamic model described in Appendix B.
- [63] Y. Fei and C. Bertka, *Science* **308**, 1120 (2005).
- [64] A. M. Rosenfeld and M. J. Stott, *Phys. Rev. B* **42**, 3406 (1990).
- [65] R. A. Secco and H. H. Schlössin, *J. Geophys. Res.* **94**, 5887 (1989).
- [66] R. E. Silber, R. A. Secco, and W. Yong, *J. Geophys. Res. Solid Earth* **122**, 5064 (2017).
- [67] I. C. Ezenwa and R. A. Secco, *Earth Planet. Sci. Lett.* **474**, 120 (2017).
- [68] I. C. Ezenwa, R. A. Secco, W. Yong, M. Pozzo, and D. Alfè, *J. Phys. Chem. Solids* **110**, 386 (2017).
- [69] F. Wagle and G. Steinle-Neumann, *Geophys. J. Int.* **213**, 237 (2018).
- [70] M. Pozzo, C. Davies, D. Gubbins, and D. Alfè, *Earth Planet. Sci. Lett.* **393**, 159 (2014).
- [71] N. de Koker and L. Stixrude, *Geophys. J. Int.* **178**, 162 (2009).
- [72] V. Vlček, N. de Koker, and G. Steinle-Neumann, *Phys. Rev. B* **85**, 184201 (2012).
- [73] L. Nordheim, *Naturwissenschaften* **16**, 1042 (1928).

***Supplemental Material: Saturation and negative temperature coefficient of electrical resistivity in liquid iron-sulfur alloys at high densities from first principles calculations***

Fabian Wagle and Gerd Steinle-Neumann

*Bayerisches Geoinstitut, Universität Bayreuth, 95440 Bayreuth, Germany.*

Nico de Koker

*School of Geosciences, University of the Witwatersrand, Johannesburg, South Africa.*

(Dated: March 8, 2018)

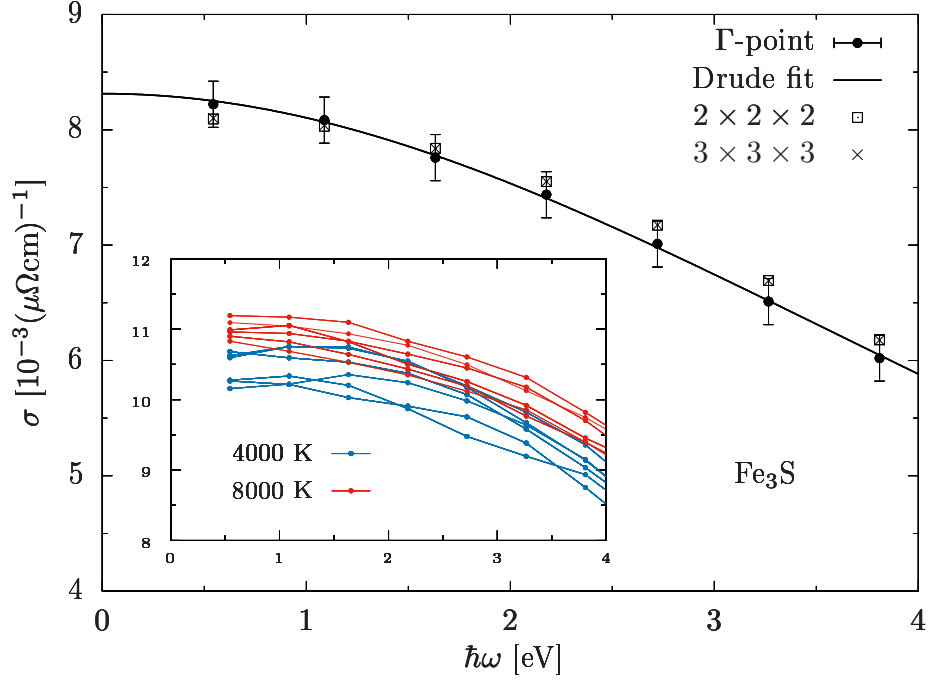


FIG. S1. Optical conductivity  $\sigma(\omega)$  for  $\text{Fe}_3\text{S}$  ( $V = 11.82 \text{ \AA}^3/\text{atom}$ ,  $T = 8000 \text{ K}$ ) fitted with a Drude model (equation 6). Results are converged to within 3% with respect to Brillouin-zone sampling by using the zone center only. The inset shows various  $\sigma(\omega)$  curves from different MD snapshots for  $\text{Fe}_3\text{S}$  at  $V = 7.09 \text{ \AA}^3/\text{atom}$  for 4000 K and 8000 K, demonstrating that the negative temperature coefficient of resistivity is statistically significant.

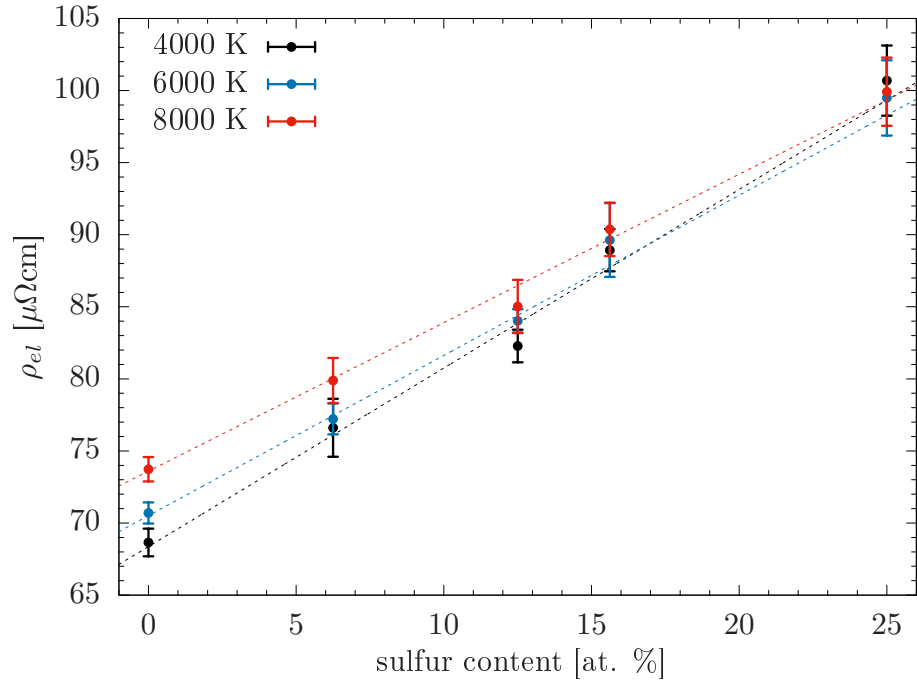


FIG. S2. Electrical resistivity as a function of sulfur concentration at a volume of  $8.28 \text{ \AA}^3/\text{atom}$  for Fe,  $\text{Fe}_{15}\text{S}$  (3.7 wt.%),  $\text{Fe}_7\text{S}$  (7.6 wt.%),  $\text{Fe}_{27}\text{S}_5$  (9.6 wt.%) and  $\text{Fe}_3\text{S}$  (16 wt.% sulfur) with linear regressions to guide the eye. Although the simulations have been performed at the same atomic volume, the molar volumes vary along the  $x$ -axis and are therefore not comparable *sensu stricto* and cannot be fit with a Nordheim rule-like expression.<sup>73</sup>

<sup>73</sup>L. Nordheim, Naturwiss. **16**, 1042 (1928)

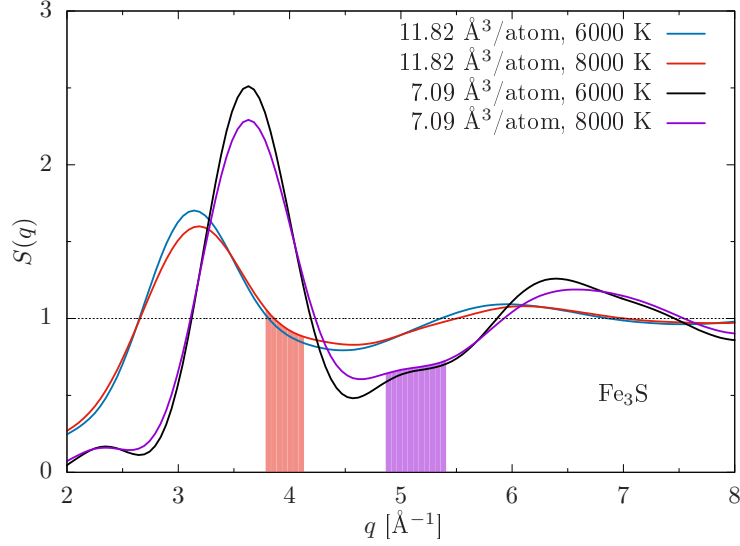


FIG. S3. Temperature dependence of static structure factors  $S(q)$  of  $\text{Fe}_3\text{S}$  for lowest ( $V = 11.82 \text{ \AA}^3/\text{atom}$ ) and highest compression ( $V = 7.09 \text{ \AA}^3/\text{atom}$ ). The shaded areas correspond to the wavenumber of a backscattering event ( $2k_F$ ) at the respective volume, computed by  $k_F = (3\pi^2 n_{\text{eff}})^{1/3}$  with the corresponding uncertainty. According to Ziman's formula,<sup>22</sup> the change of  $S(q)$  at this value determines the temperature coefficient of resistivity. Based on the structure factor and the location of  $2k_F$ , one expects a positive temperature coefficient of resistivity for both compressions.

<sup>22</sup>J. M. Ziman, *Philos. Mag.* **6**, 1013 (1961)

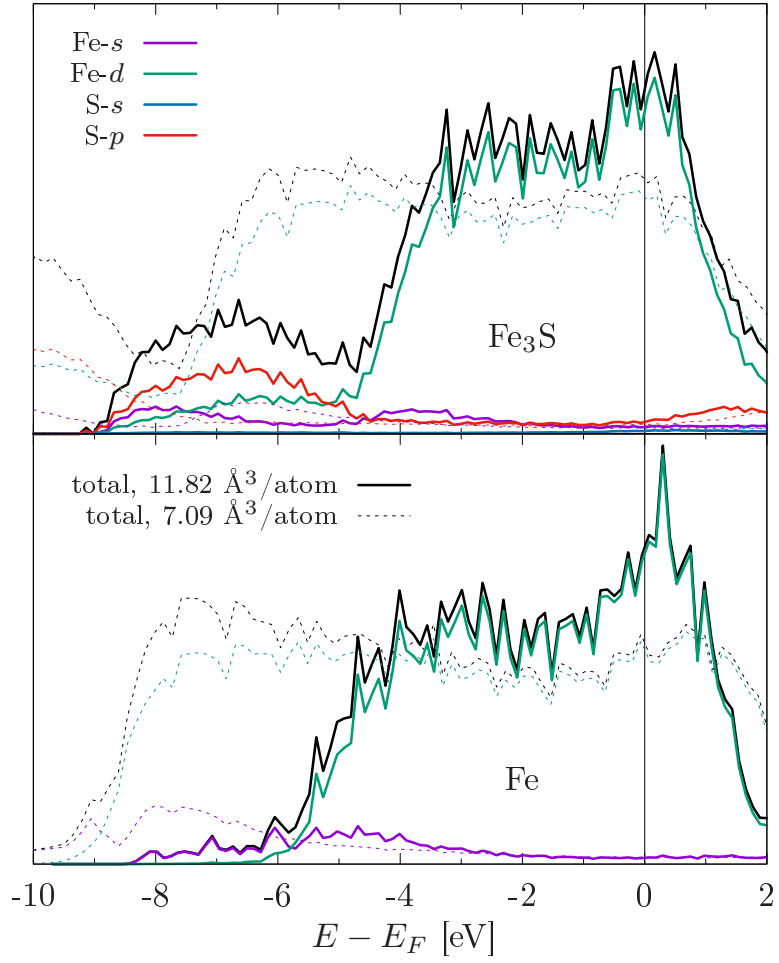


FIG. S4. Broadening of site- and angular momentum-projected electron densities of states for  $\text{Fe}_3\text{S}$  (top) and pure Fe (bottom) at 4000 K with decreasing cell volume.

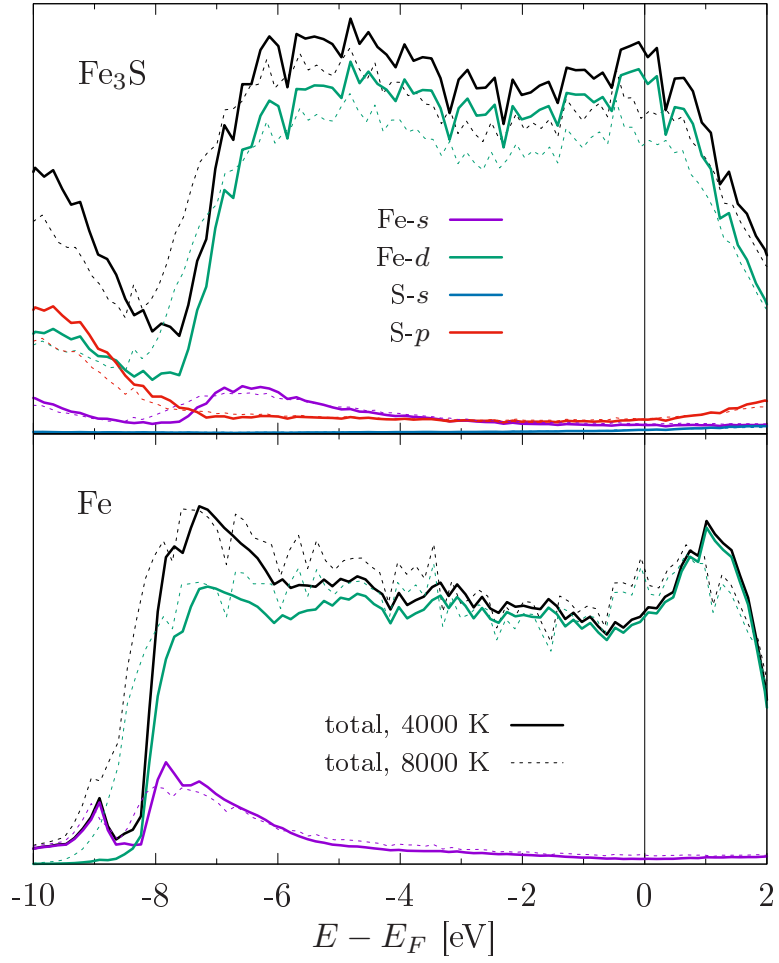


FIG. S5. Broadening of site- and angular momentum-projected densities of states with increasing  $T$  (4000 K and 8000 K) for  $\text{Fe}_3\text{S}$  (top) and pure Fe (bottom) at a cell volume of  $7.09 \text{ \AA}^3/\text{atom}$ .

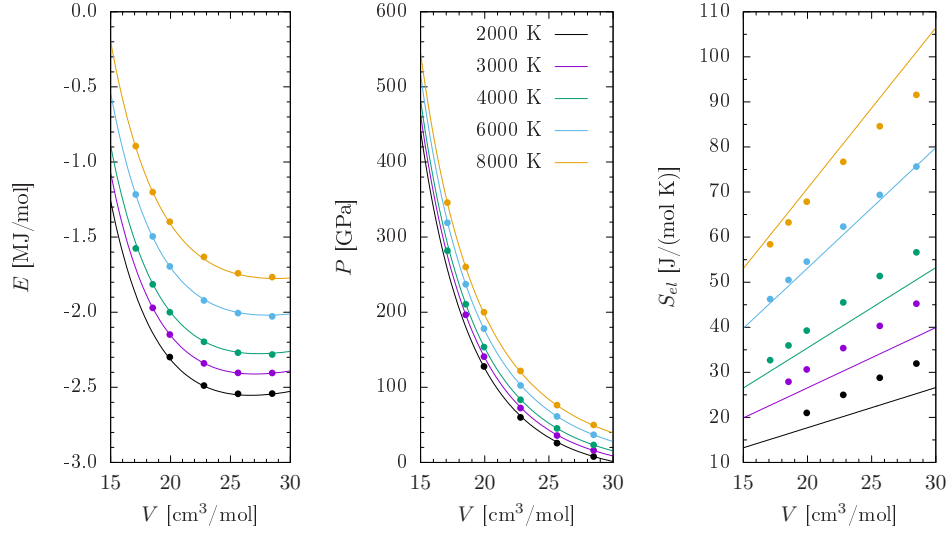


FIG. S6. Equation of state fit (lines) to DFT-MD results (dots) for liquid  $\text{Fe}_3\text{S}$  by a self consistent thermodynamic description:<sup>71</sup> Internal energy  $E$ , pressure  $P$  (without electronic entropy contribution) and electronic entropy  $S_{el}$  as a function of volume along isotherms.  $S_{el}$  is not particularly well represented by the global fit, but contributes only little to total  $P$ . The maximal error for  $T = 8000$  K is well below 2 GPa.

<sup>71</sup>N. de Koker and L. Stixrude, *Geophys. J. Int.* **178**, 162 (2009)

TABLE S1. Calculated values for pressure, electrical resistivity, thermal conductivity and Lorenz number of Fe<sub>7</sub>S from first principles computations, with reference volume  $V_0 = 11.82 \text{ \AA}^3/\text{atom}$ . Uncertainties of  $P$  due to the equation of state fit are below 1 GPa.

$V/V_0$	$T$ [K]	$P$ [GPa]	$\rho$ [ $\mu\Omega\text{cm}$ ]	$\lambda_{th}$ [ $\text{Wm}^{-1}\text{K}^{-1}$ ]	$L$ [ $10^{-8}\text{W}\Omega\text{K}^{-2}$ ]
1.0	2000	3	$93 \pm 1$	$38 \pm 1$	$1.77 \pm 0.05$
	3000	12	$95 \pm 1$	$62 \pm 1$	$1.94 \pm 0.05$
	4000	22	$100 \pm 2$	$80 \pm 2$	$1.98 \pm 0.06$
	6000	41	$105 \pm 1$	$116 \pm 2$	$2.02 \pm 0.04$
	8000	62	$111 \pm 3$	$147 \pm 4$	$2.04 \pm 0.07$
0.9	3000	33	$94 \pm 1$	$70 \pm 1$	$2.19 \pm 0.04$
	4000	44	$97 \pm 2$	$92 \pm 2$	$2.23 \pm 0.06$
	6000	66	$101 \pm 2$	$126 \pm 3$	$2.11 \pm 0.06$
	8000	89	$103 \pm 2$	$159 \pm 2$	$2.05 \pm 0.04$
0.8	4000	83	$90 \pm 1$	$100 \pm 2$	$2.26 \pm 0.04$
	6000	108	$93 \pm 2$	$138 \pm 3$	$2.14 \pm 0.06$
	8000	134	$97 \pm 1$	$170 \pm 2$	$2.07 \pm 0.04$
0.7	2000	118	$80 \pm 2$	$46 \pm 2$	$1.82 \pm 0.08$
	3000	136	$81 \pm 1$	$77 \pm 2$	$2.08 \pm 0.05$
	4000	152	$82 \pm 1$	$104 \pm 1$	$2.13 \pm 0.04$
	6000	184	$84 \pm 1$	$150 \pm 3$	$2.09 \pm 0.04$
	8000	214	$85 \pm 2$	$195 \pm 2$	$2.08 \pm 0.05$
0.65	3000	189	$77 \pm 2$	$82 \pm 2$	$2.10 \pm 0.07$
	4000	209	$78 \pm 2$	$111 \pm 2$	$2.16 \pm 0.06$
	6000	244	$80 \pm 1$	$161 \pm 3$	$2.13 \pm 0.05$
	8000	277	$82 \pm 2$	$204 \pm 4$	$2.10 \pm 0.07$
0.6	4000	288	$75 \pm 2$	$119 \pm 2$	$2.21 \pm 0.06$
	6000	328	$75 \pm 1$	$174 \pm 4$	$2.18 \pm 0.06$
	8000	365	$77 \pm 2$	$220 \pm 6$	$2.12 \pm 0.07$

TABLE S2. Calculated values for pressure, electrical resistivity, thermal conductivity and Lorenz number of Fe<sub>3</sub>S from first principles computations, with reference volume  $V_0 = 11.82 \text{ \AA}^3/\text{atom}$ . Uncertainties of  $P$  due to the equation of state fit are below 1 GPa.

$V/V_0$	$T$ [K]	$P$ [GPa]	$\rho$ [ $\mu\Omega\text{cm}$ ]	$\lambda_{th}$ [ $\text{Wm}^{-1}\text{K}^{-1}$ ]	$L$ [ $10^{-8}\text{W}\Omega\text{K}^{-2}$ ]
1.0	4000	25	$113 \pm 3$	$70 \pm 2$	$1.96 \pm 0.07$
	6000	41	$118 \pm 2$	$97 \pm 2$	$1.91 \pm 0.06$
	8000	59	$124 \pm 3$	$121 \pm 3$	$1.87 \pm 0.06$
0.9	2000	27	$111 \pm 3$	$40 \pm 1$	$2.20 \pm 0.08$
	4000	46	$109 \pm 4$	$81 \pm 2$	$2.22 \pm 0.10$
	6000	66	$113 \pm 2$	$111 \pm 1$	$2.09 \pm 0.04$
	8000	85	$117 \pm 1$	$133 \pm 2$	$1.95 \pm 0.03$
0.8	3000	73	$108 \pm 3$	$64 \pm 2$	$2.29 \pm 0.09$
	4000	85	$107 \pm 4$	$85 \pm 2$	$2.29 \pm 0.10$
	6000	107	$107 \pm 2$	$121 \pm 2$	$2.14 \pm 0.06$
	8000	129	$108 \pm 2$	$151 \pm 3$	$2.03 \pm 0.05$
0.7	2000	126	$103 \pm 4$	$34 \pm 1$	$1.75 \pm 0.10$
	3000	141	$102 \pm 2$	$59 \pm 1$	$2.01 \pm 0.06$
	4000	155	$101 \pm 2$	$85 \pm 3$	$2.15 \pm 0.08$
	6000	181	$100 \pm 3$	$129 \pm 2$	$2.15 \pm 0.07$
	8000	206	$100 \pm 2$	$170 \pm 4$	$2.13 \pm 0.07$
0.65	3000	196	$102 \pm 2$	$62 \pm 2$	$2.08 \pm 0.08$
	4000	211	$99 \pm 2$	$86 \pm 2$	$2.15 \pm 0.07$
	6000	240	$96 \pm 2$	$136 \pm 3$	$2.17 \pm 0.07$
	8000	267	$96 \pm 3$	$178 \pm 5$	$2.14 \pm 0.08$
0.6	4000	291	$96 \pm 2$	$91 \pm 4$	$2.18 \pm 0.10$
	6000	323	$95 \pm 2$	$141 \pm 3$	$2.23 \pm 0.07$
	8000	352	$91 \pm 2$	$189 \pm 3$	$2.16 \pm 0.06$

TABLE S3. Parameters of the modified thermodynamic model by *de Koker and Stixrude*<sup>71</sup> for  $V_0 = 11.82 \text{ \AA}^3/\text{atom}$  and  $T_0 = 2000 \text{ K}$ . Values for extensive variables are per mol of formula units.

		Fe	Fe <sub>7</sub> S	Fe <sub>3</sub> S
$P_{xs0}$	[GPa]	-2.335	0.846	5.534
$K_{T,xs0}$	[GPa]	131.4	137.8	140.0
$K'_{T,xs0}$		5.161	4.694	4.736
$\alpha K_{T,xs0}$	[GPa/K]	$8.822 \cdot 10^{-3}$	$8.620 \cdot 10^{-3}$	$7.194 \cdot 10^{-3}$
$V_0 \left( \frac{\partial \alpha K_T}{\partial V} \right)_{T,xs0}$	[GPa/K]	$-1.563 \cdot 10^{-2}$	$-1.660 \cdot 10^{-2}$	$-1.327 \cdot 10^{-2}$
$T_0 \left( \frac{\partial \alpha K_T}{\partial T} \right)_{T,xs0}$	[GPa/K]	$-3.348 \cdot 10^{-3}$	$-2.376 \cdot 10^{-3}$	$-1.808 \cdot 10^{-3}$
$V_0^2 \left( \frac{\partial^2 \alpha K_T}{\partial V^2} \right)_{T,xs0}$	[GPa/K]	$2.840 \cdot 10^{-2}$	$5.115 \cdot 10^{-2}$	$3.534 \cdot 10^{-2}$
$C_{V,xs0}$	[J/(mol K)]	18.50	185.1	92.90
$V_0 \left( \frac{\partial C_V}{\partial V} \right)_{T,xs0}$	[kJ/(mol K)]	15.84	317.1	79.57
$V_0^2 \left( \frac{\partial^2 C_V}{\partial V^2} \right)_{T,xs0}$	[kJ/(mol K)]	$2.113 \cdot 10^{-2}$	$3.094 \cdot 10^{-1}$	$1.133 \cdot 10^{-1}$
$\zeta_0$	[J/(mol K <sup>2</sup> )]	3.486	30.04	12.63
$\xi$		0.843	1.096	1.006

<sup>71</sup>N. de Koker and L. Stixrude, Geophys. J. Int. **178**, 162 (2009)

**6 Wagle & Steinle-Neumann (2018),  
Geophys. J. Int. 213, 237–243**



## Electrical resistivity discontinuity of iron along the melting curve

Fabian Wagle and Gerd Steinle-Neumann

Bayerisches Geoinstitut, Universität Bayreuth, 95447 Bayreuth, Germany. E-mail: [fabian.wagle@uni-bayreuth.de](mailto:fabian.wagle@uni-bayreuth.de)

Accepted 2017 December 8. Received 2017 November 28; in original form 2017 August 22

### SUMMARY

Discontinuous changes of electrical resistivity  $\rho_{el}$  (increase), density  $\rho$  and isothermal compressibility  $\beta_T$  (decrease) occur across the melting temperature of metals and can be directly related by Ziman's theory in the long-wavelength approximation. By evaluating experimental data at ambient pressure, we show that Ziman's approximation holds for iron and other simple and transition metals. Using a thermodynamic model to determine  $\beta_T$  for  $\gamma$ -,  $\epsilon$ - and liquid Fe and a previously published model for  $\rho_{el}$  of liquid Fe, we apply Ziman's approximation to calculate  $\rho_{el}$  of solid Fe along the melting curve. For pure Fe, we find the discontinuity in  $\rho_{el}$  to decrease with pressure and to be negligibly small at inner core boundary conditions. However, if we account for light element enrichment in the liquid outer core, the electrical resistivity decrease across the inner core boundary is predicted to be as large as 36 per cent.

**Key words:** Electrical properties; High pressure behaviour; Core.

### 1 INTRODUCTION

Electrical resistivity  $\rho_{el}$  of liquid metals and alloys under extreme conditions is a critical parameter for the stability and evolution of planetary dynamos. In particular, the magnetic fields of the Earth, Mercury and Ganymede are thought to be generated by a self-sustained dynamo in the convecting liquid portions of their cores, which are composed of mainly iron and a variety of lighter elements (Merrill *et al.* 1996; Sarson *et al.* 1997; Anderson *et al.* 2011). In that context, the role of the inner core (IC) in magnetic field generation remains a subject of controversy (Olson & Amit 2014). Initial geodynamic studies (Hollerbach & Jones 1993; Glatzmaier & Roberts 1995) reported evidence that finite electrical resistivity in the Earth's solid IC has a stabilizing effect on the magnetic field and therefore leads to a decrease in the frequency of global field reversals. Subsequently, however, there have been conflicting results regarding this argument, ranging from support of the initial inference (Dharmaraj & Stanley 2012), no influence (Wicht 2002), to an increased number of excursion in the presence of a conducting IC when compared to results with an insulator at the centre of the planet (Lhuillier *et al.* 2013). For conducting ICs, these studies have relied on conductivity values of the IC being the same as for the outer core (OC), while one would expect that resistivity changes across the IC boundary (ICB) for two reasons: (i) The structure of solid and liquid are quite different and resistivity changes across the melting temperature ( $T_m$ ) and (ii) light elements will not equally partition between the OC and the IC. In the current manuscript we look at these two effects with the goal to provide values of  $\rho_{el}$  for use in geodynamo simulations that may help to better assess the effect of the IC on magnetic field generation.

In general, metals exhibit a distinct increase in electrical resistivity upon melting. For iron, it increases by  $\sim 8$  per cent at ambient

pressure ( $P$ ; van Zytveld 1980; Table 1), a value that remains approximately constant up to 6 GPa as determined in large volume press experiments (Secco & Schlössin 1989; see Supporting Information Fig. S1). In similar experiments, Ezenwa & Secco (2017b) recently determined a jump of similar magnitude for another transition metal, Co, while for the closed  $d$ -shell metals, Zn and Cu, the discontinuity is significantly larger (Ezenwa & Secco 2017a; Ezenwa *et al.* 2017). These data are of very high quality and determine the jump across  $T_m$  with great precision. At higher  $P$ , static experiments using the diamond anvil cell (DAC) are more scarce and the small sample size and potential temperature ( $T$ ) gradients inside a DAC make high  $P$ - $T$  experiments challenging, especially close to  $T_m$  (Dobson 2016), resulting in large uncertainties of the data and consequently the determination of a potential resistivity discontinuity. Ohta *et al.* (2016) recently reported  $T$ -dependent resistivities for the solid and the liquid phase of iron up to 51 GPa measured in the DAC, and they describe an increase by as much as  $\sim 20$  per cent across melting (see Supporting Information Fig. S2). At higher  $P$ , Ohta *et al.* (2016) relied on resistivity measurements for the solid hcp ( $\epsilon$ ) phase of Fe only, and in order to estimate  $\rho_{el}$  for the liquid, they used a Bloch–Grüneisen fit—taking resistivity saturation into account—to their data to extrapolate to  $T_m$  and added 20 per cent to account for the increase of  $\rho_{el}$  upon melting in an *ad-hoc* fashion. Gomi *et al.* (2013) performed measurements of  $\rho_{el}$  for hcp Fe up to 100 GPa at room  $T$  only, and argue along the theory of Mott (1972) that iron at core conditions is close to saturation resistivity and therefore the increase of  $\rho_{el}$  on melting should be negligible. In the development of their model resistivity and its application to the Earth's core, Gomi *et al.* (2013) do not distinguish between the solid and liquid phase.

Complementary to experiments, electronic transport properties at high  $P$  have been calculated by evaluating the Kubo–Greenwood

**Table 1.** Thermophysical data for pure iron at ambient pressure at the melting point ( $T_m = 1808 \pm 5$  K)<sup>a</sup>. Resistivities have been measured by Cezairliyan & McClure (1974)<sup>a</sup> and van Zytveld (1980)<sup>b</sup>. If not reported directly, values measured by Dever (1972)<sup>c</sup>, Basinski *et al.* (1955)<sup>d</sup>, Tsu *et al.* (1985)<sup>e</sup>, Drotning (1981)<sup>f</sup> and compiled by Desai (1986)<sup>g</sup> have been extrapolated to  $T_m$  while using the misfit as uncertainty. For the liquid phase, a scenario including values for  $\rho$  and  $\alpha$  from Assael *et al.* (2006)<sup>h</sup> has been tabulated for comparison. A column of thermodynamic properties for liquid Fe from the model of Komabayashi (2014)<sup>i</sup> has been included. Compressibilities  $\beta_S$  and  $\beta_T$  have been calculated using eqs (6) and (7).

	$\delta$ -Fe	Drotning	Liquid Fe Assael	Thermodynamic model <sup>i</sup>
$\rho_{el}$ [ $\mu\Omega$ cm]	$127.0 \pm 0.6^a$		$137.6 \pm 1.0^b$	
$v_p$ [ $\text{km s}^{-1}$ ]	$4.73 \pm 0.07^c$	$3.98 \pm 0.03^e$		3.98
$v_s$ [ $\text{km s}^{-1}$ ]	$2.49 \pm 0.06^c$			
$\rho$ [ $\text{g cm}^{-3}$ ]	$7.29 \pm 0.02^d$	$7.017 \pm 0.002^f$	$7.04 \pm 0.06^h$	7.09
$\alpha$ [ $10^{-5} \text{ K}^{-1}$ ]	$6.5 \pm 0.1^d$	$8.8 \pm 0.1^f$	$13.2 \pm 0.1^h$	9.0
$c_p$ [ $\text{J g}^{-1} \text{K}^{-1}$ ]	$0.80 \pm 0.06^g$		$0.84 \pm 0.05^g$	0.82
$\beta_S$ [ $\text{GPa}^{-1}$ ]	$1/(103 \pm 6)$	$1/(111 \pm 2)$	$1/(112 \pm 2)$	1/112
$\beta_T$ [ $\text{GPa}^{-1}$ ]	$1/(91 \pm 5)$	$1/(88 \pm 2)$	$1/(70 \pm 2)$	1/87
$\frac{\rho_{el}^{\text{liquid}}}{\rho_{el}^{\text{solid}}} \left( \frac{\rho^{\text{liquid}}}{\rho^{\text{solid}}} \right)^2 \left( \frac{\beta_T^{\text{liquid}}}{\beta_T^{\text{solid}}} \right)^{-1}$		$0.97 \pm 0.05$	$0.78 \pm 0.05$	$0.98 \pm 0.05$

(KG) formula for the Onsager kinetic coefficients on results of density functional theory (DFT)-based molecular dynamics (MD) simulations (Vlček *et al.* 2012; de Koker *et al.* 2012; Pozzo *et al.* 2012, 2013, 2014), a computationally expensive approach. For pure liquid iron at conditions of the Earth's ICB, these studies agree on values of resistivity slightly above  $60 \mu\Omega$  cm (de Koker *et al.* 2012; Pozzo *et al.* 2012), while for  $\varepsilon$ -Fe at similar densities,  $T$ -dependent values of  $\rho_{el}^{\text{solid}} = 53\text{--}57 \mu\Omega$  cm have been reported (Pozzo *et al.* 2014). These results suggest that a change in  $\rho_{el}$  on melting—albeit small—persists to core conditions.

The determination of electronic transport properties of metals under extreme  $P$  and  $T$  is challenging both experimentally and computationally, and remains a topic of a controversial discussion. In this study, we address the question of electrical resistivity of solid Fe close to  $T_m$  along the melting curve by a different approach: We use Ziman's theory to relate electronic and elastic properties upon melting, which we test on experimental data of Fe at ambient pressure. We then apply this method along the melting curve and infer resistivities of the solid phase at high  $P$  based on previously published values for the liquid and discuss the influence of light element alloying and partitioning at crystallization of the IC, as it is relevant for cores of terrestrial planetary bodies.

## 2 METHODS

The Ziman formula for electrical resistivity (Ziman 1961)

$$\rho_{el} = \frac{a_0 \hbar}{e^2} \frac{4\pi^3 Z}{a_0 k_F} \frac{1}{(2k_F)^4} \int_0^{2k_F} S(q) |U(q)|^2 q^3 dq \quad (1)$$

has been widely applied to determine  $\rho_{el}$  for metallic liquids up to the warm dense matter regime (e.g. Burrill *et al.* 2016). In this model, quasi-free conduction electrons of momentum  $\hbar\mathbf{k}$  scatter off screened ionic potentials  $U(q)$ , where  $q = |\mathbf{k} - \mathbf{k}'|$  is the scattering wavenumber. The spatial arrangement of scattering centres is described by the static ion-ion structure factor  $S(q)$  in reciprocal space and incorporates an implicit dependence on density  $\rho$  and  $T$ . The pre-factor  $\frac{a_0 \hbar}{e^2} \approx 21.74 \mu\Omega$  cm is the atomic unit of resistivity (with  $a_0$  being the Bohr radius,  $\hbar$  the reduced Planck constant and  $e$  the elementary charge),  $Z$  the number of valence electrons and  $k_F$  the Fermi wavenumber. Due to conservation of momentum, scattering takes place from and into states at the Fermi level. Therefore, the

largest possible change of momentum upon an elastic collision is  $2k_F$  for a backscattered electron ( $\mathbf{k} \rightarrow \mathbf{k}' = -\mathbf{k}$ ) which determines the upper integration boundary.

In the derivation of eq. (1), several approximations have been made. (i) The Fermi surface is assumed to be isotropic. For liquids and amorphous solids, this is always the case. For many crystalline solids it is a good approximation as has been shown for bcc and fcc metals (Papaconstantopoulos 1986). In addition, if one is interested in resistivity of a polycrystal, the Hashin-Shtrikman (HS) bounds (Hashin & Shtrikman 1963) for  $\rho_{el}$  are very narrow for the group 8 elements Ru and Os, that crystallize in the hcp phase at ambient  $P$  (Volkenshteyn *et al.* 1978; Schriempf 1968) (see Supporting Information Table S2). (ii) Higher frequency ( $\omega$ ) moments of  $S(q, \omega)$  have been omitted, since they are dominated by interionic contributions which are generally very small (Cheung & Ashcroft 1978). Furthermore, for  $T$  above the Debye temperature ( $\theta_D$ ), the  $\omega$ -dependence due to the distribution function  $\frac{\hbar\omega}{k_B T} / (e^{\frac{\hbar\omega}{k_B T}} - 1) = \frac{\hbar\omega}{k_B T} / [1 + \frac{\hbar\omega}{k_B T} + \dots] - 1 \approx 1$  (with the Boltzmann constant  $k_B$ ) can be neglected. (iii) The spread of the Fermi-Dirac distribution ( $k_B T$ ) is larger than the maximum energy transfer by phonons ( $k_B \theta_D$ ) at these conditions. Therefore, it is reasonable to treat electron scattering in solids at high  $T$  quasi-elastically.

By means of eq. (1), Ashcroft & Lekner (1966) calculated resistivities for a number of liquid metals by using different model potentials and an analytical expression for the hard sphere structure factor  $S^{\text{hs}}(q)$  (Wertheim 1963). Their results agree reasonably well with experimental values at ambient  $P$ . Taking  $\rho$ -dependence of  $S^{\text{hs}}(q)$  into account, the Ziman formula has been applied to  $P$  of the Earth's OC by Jain & Evans (1971), who constrained the resistivity of liquid iron at the core-mantle boundary to be  $104 \pm 6 \mu\Omega$  cm at 3473 K. The KG approach yields values of about two thirds of this number at comparable  $P$  and  $T$ , which may indicate a breakdown of the hard sphere approximation at high densities.

As the ionic potential  $U(q)$  does not change across  $T_m$ , the increase of  $\rho_{el}$  upon melting occurs due to the transition from a crystalline into a disordered structure, which is reflected by changes in  $S(q)$  and  $\rho$ . As a first order approximation, Ziman (1961) proposed to replace the integral in eq. (1) by the integrand's value at  $q = 0$ . While  $S(q)$  contains implicit information on density, other factors in eq. (1) depend on  $\rho$  explicitly:  $U$  by its normalization to  $-2/3 \cdot E_F$  at  $q = 0$  ( $E_F$  being the Fermi energy), and the Fermi radius  $k_F$ . For the

free electron gas, they scale as  $E_F \propto \varrho^{2/3}$  and  $k_F \propto \varrho^{1/3}$ , respectively. While Fe is not a free electron metal, its Fermi level shows the same dependence on volume (Supporting Information Fig. S3). Combining  $k_F^{-5}$  in the pre-factor with  $E_F^{-2}$  from the integrand, resistivity decreases  $\propto \varrho^{-3}$ . If one considers the ratio of resistivities in the liquid and the solid phase at  $T_m$ , in the Ziman approximation the following relation holds:

$$\frac{\rho_{\text{el}}^{\text{liquid}}}{\rho_{\text{el}}^{\text{solid}}} \approx \frac{S(0)^{\text{liquid}}}{S(0)^{\text{solid}}} \left( \frac{\varrho^{\text{liquid}}}{\varrho^{\text{solid}}} \right)^{-3}. \quad (2)$$

On the other hand, the distribution of atoms in condensed matter determines bulk elastic parameters. Since the thermodynamic limit

$$\lim_{q \rightarrow 0} S(q) = \varrho k_B T \beta_T \quad (3)$$

is known from fluctuation theory (March 1990), the structure factor ratio in eq. (2) can be reformulated in terms of isothermal compressibilities, thermodynamically defined as  $\beta_T = -\varrho \partial(1/\varrho)/\partial P$ , and Ziman's approximation becomes

$$\frac{\rho_{\text{el}}^{\text{liquid}}}{\rho_{\text{el}}^{\text{solid}}} \approx \frac{\beta_T^{\text{liquid}}}{\beta_T^{\text{solid}}} \left( \frac{\varrho^{\text{liquid}}}{\varrho^{\text{solid}}} \right)^{-2} \quad (4)$$

or

$$\frac{\rho_{\text{el}}^{\text{liquid}}}{\rho_{\text{el}}^{\text{solid}}} \left( \frac{\varrho^{\text{liquid}}}{\varrho^{\text{solid}}} \right)^2 \left( \frac{\beta_T^{\text{liquid}}}{\beta_T^{\text{solid}}} \right)^{-1} \approx 1. \quad (5)$$

Jain & Evans (1971) inserted a model for  $\varrho$ ,  $T$  and  $\beta_T$  of the Earth into eq. (3), which fully defines the variation of  $S^{\text{hs}}(q)$  with  $P$  and  $T$ . While we do not calculate absolute resistivity values, we use the long-wavelength approximation to eq. (1) as a method to estimate the relative increase of  $\rho_{\text{el}}$  from  $\rho_{\text{el}}^{\text{liquid}}$  to  $\rho_{\text{el}}^{\text{solid}}$  across the melting curve based on thermodynamic parameters.

The application of eq. (4) is not limited to this direction. High  $P$  experiments such as those performed by Gomi *et al.* (2013) or Ohta *et al.* (2016) for the solid could make use of it to convert  $\rho_{\text{el}}^{\text{solid}}$  to  $\rho_{\text{el}}^{\text{liquid}}$  or cross-check their data.

### 3 RESULTS AND DISCUSSION

#### 3.1 Ambient pressure

We assess the validity of relation (5) for iron at ambient  $P$  by compiling experimental data for  $\rho_{\text{el}}$ ,  $\varrho$  and  $\beta_T$  right above and below  $T_m$ . Electrical resistivity of iron in the solid state has been measured up to 1800 K (Cezairliyan & McClure 1974) and for the liquid starting at 1808 K (van Zytveld 1980), with a ratio of  $\rho_{\text{el}}^{\text{liquid}}/\rho_{\text{el}}^{\text{solid}} = 1.08 \pm 0.01$  (Table 1).

To obtain compressibilities, we rely on ultrasonic measurements of the longitudinal and transverse acoustic velocities ( $v_p$  and  $v_s$ , respectively), which are related to isentropic compressibility  $\beta_S$  via

$$v_p^2 - \frac{4}{3}v_s^2 = \frac{1}{\varrho\beta_S}, \quad (6)$$

with  $v_s = 0$  for the liquid. To convert  $\beta_S$  to  $\beta_T$ , one has to apply the thermodynamic relation

$$\beta_T = \beta_S + \frac{\alpha^2 T}{\varrho c_p}, \quad (7)$$

with  $c_p$  being the heat capacity at constant  $P$  and  $\alpha$  the coefficient of thermal expansion. If not directly reported, we extrapolated the thermophysical quantities in eq. (7) to  $T_m$  (see Table 1).

To the best of our knowledge, no data exist on acoustic velocities for the  $\delta$ -phase of iron (in the bcc structure) which is in equilibrium with the liquid at ambient  $P$ . Instead, we use single crystal elastic constants of the  $\alpha$ -phase (also in the bcc structure) from Dever (1972) above 1050 K, calculate  $v_p$  and  $v_s$  from a Voigt–Reuss–Hill polycrystalline average and linearly extrapolate to  $T_m$  (Table 1). This approach is well justified as any magnetic contribution to  $\beta_T$  vanishes above the Curie temperature (1043 K), and the  $\alpha$ - and  $\delta$ -phase stability region can be viewed as belonging to the same stability field that is connected at negative pressure (Komabayashi & Fei 2010). In order to apply eq. (7), we use values for  $\varrho$  and  $\alpha$  from the X-ray diffraction study of Basinski *et al.* (1955) and  $c_p$  from Cezairliyan & McClure (1974).

Thermodynamic parameters for liquid iron are more controversial. Measured sound velocities range from 3820 to 4052 m s<sup>-1</sup> (Nasch *et al.* 1994; Casas *et al.* 1984) and  $\varrho$  from 6937 to 7120 kg m<sup>-3</sup> (Blumm & Henderson 2000; Hixson *et al.* 1990). For  $v_p$  we choose the measurements by Tsu *et al.* (1985) (Table 1) that are most consistent with values computed with the thermodynamic model of Komabayashi (2014). Density values are closely associated with those of thermal expansivity  $\alpha$  which has the strongest influence on the determination of  $\beta_T$  from  $\beta_S$ , as it enters in quadratic form in eq. (7). As for the solid phase, values of  $\varrho$  and  $\alpha$  should be chosen consistently, i.e. come from the same underlying data of  $\varrho(T)$ . Thermal expansivity of liquid iron has been the topic of a long-standing controversy (Williams 2009) with either values below  $0.9 \times 10^{-4}$  K<sup>-1</sup> (e.g. Drotning 1981; Nasch & Steinemann 1995; Blumm & Henderson 2000) or larger than  $1.1 \times 10^{-4}$  K<sup>-1</sup> (e.g. Kirshenbaum & Cahill 1962; Saito *et al.* 1969; Hixson *et al.* 1990). With the exception of the dilatometer work of Blumm & Henderson (2000), the former data stem from  $\gamma$ -ray attenuation studies and the latter from constant mass setups (e.g. Archimedeian, maximum bubble pressure, levitation techniques). Following Assael *et al.* (2006), Williams (2009) argued for the larger  $\alpha$  on the basis of potential systematic errors due to the sample geometry in  $\gamma$ -ray attenuation. However, constant mass methods may underestimate effects of wetting, surface tension and viscosity (Drotning 1981; Nasch *et al.* 1994), which could also account for the discrepancy. Using the values recommended by Assael *et al.* (2006),  $\beta_T = 1/(70 \pm 2)$  GPa<sup>-1</sup>, with  $\varrho$  and  $\alpha$  from Drotning (1981),  $\beta_T = 1/(88 \pm 2)$  GPa<sup>-1</sup>. Only for the  $\beta_T$  value based on  $\varrho$  and  $\alpha$  of Drotning (1981), the Ziman approximation (eq. 5) holds (Table 1).

The thermodynamic limit of  $S(q)$  (eq. 3) provides an alternative route to the determination of  $\beta_T$  independent of  $\alpha$ . We have fitted measured  $S(q)$  of liquid iron (Waseda & Ohtani 1974) by means of a Percus–Yevick hard-sphere expression in the long wavelength limit (see Supporting Information Figs S4 and S5) and find, despite considerable uncertainty, a compressibility value that is consistent with the acoustic-velocity-based value using  $\varrho$  and  $\alpha$  of Drotning (1981), supporting the validity of Ziman's approximation for iron at ambient  $P$ . Model parameters for liquid iron from Komabayashi (2014) also agree well with the  $S(q)$ -based  $\beta_T$  and satisfy eq. (5) in combination with the experimental data of  $\delta$ -Fe (Table 1).

A similar evaluation of eq. (5) for other metallic elements can be found in the Supporting Information (Tables S3–S5). We find that the resistivity ratio is well represented by the right hand side of eq. (4) for the simple metals Na and Al, and the 3d transition metals Co and Ni. For Zn and the noble metals Cu, Ag and Au—all metals with closed  $d$ -shell—it is systematically underestimated by a factor of  $\sim 1.5$ , that is, the increase in  $\rho_{\text{el}}$  across melting (left-hand side of eq. 4) is significantly larger than the ratio of thermodynamic properties (right-hand side of eq. 4). For Co, Cu and Zn,

the resistivity jump at ambient  $P$  is consistent with the experiments up to 5 GPa (Ezenwa & Secco 2017a,b; Ezenwa *et al.* 2017).

### 3.2 High pressure

In order to obtain the right hand side of eq. (4) at high  $P$  for Fe, we compute  $\varrho$  and  $\beta_T$  on both the liquid and the solid side of the melting curve with the model of Komabayashi (2014) (Fig. 1a). For the liquid, the model yields a value for  $\varrho^{\text{liquid}}$  which is consistent with experimental work by Tateyama *et al.* (2011) at 4.3 GPa and shock experiments up to  $\sim 440$  GPa (Brown & McQueen 1986; Brown *et al.* 2000) (see Supporting Information Fig. S6). The thermodynamic model by Komabayashi (2014) has been designed to reproduce results from DAC and multi-anvil experiments for the solid phases. The applicability of this model in the geophysical context is further supported when comparing its ratio of adiabatic compressibilities at the ICB ( $\beta_S^{\text{liquid}}/\beta_S^{\text{solid}} = 1.02$ ) with that of PREM ( $\beta_S^{\text{liquid}}/\beta_S^{\text{solid}} = 1.03$ ) (Dziewonski & Anderson 1981).

Fig. 1(b) shows both  $\rho_{\text{el}}^{\text{liquid}}$  and  $\rho_{\text{el}}^{\text{solid}}$  for pure Fe as a function of  $P$ , covering conditions up to 360 GPa, the pressure in the Earth's centre. Resistivities in the liquid phase have been calculated from the modified Bloch–Grüneisen model by de Koker *et al.* (2012) and  $\rho_{\text{el}}^{\text{solid}}$  has been computed by means of eq. (5). We predict  $\rho_{\text{el}}^{\text{solid}}$  for iron in the range of 69–71  $\mu\Omega\text{cm}$  at conditions of the cores of Mars, Mercury and Ganymede, while  $\rho_{\text{el}}^{\text{liquid}} \approx 78 - 88 \mu\Omega\text{cm}$ .

The KG results by de Koker *et al.* (2012) underestimate  $\rho_{\text{el}}^{\text{liquid}}$  at ambient conditions and low  $P$  compared to experiments, and this mismatch suggests that  $\rho_{\text{el}}^{\text{solid}}$  should also be considered with caution there. Two effects contribute to this discrepancy. (i) The underlying equation of state overestimates density at ambient  $P$  by  $\sim 20$  per cent, similar to the small volume at zero pressure reported for liquid iron from DFT–MD simulations by Ichikawa *et al.* (2014). Smaller volumes lead to reduced resistivity values. (ii) Recent results of Drchal *et al.* (2017) indicate that there is a possible contribution of spin disorder to  $\rho_{\text{el}}$  at high  $T$ , which has not been taken into account by previous computational studies. At higher  $P$ , however, resistivity values of de Koker *et al.* (2012) are in good agreement with shock wave data (Keeler 1971; Matassov 1977; Bi *et al.* 2002).

Stacey & Anderson (2001) have argued that  $\rho_{\text{el}}$  remains constant along the melting curve. In their derivation of  $\partial(\ln \rho_{\text{el}})/\partial P = 0$ , they express the Grüneisen parameter in terms of an average lattice frequency, and they do not distinguish between the liquid and the solid phase. Since the melting point defines an extreme case of anharmonicity, it is not clear to what degree their conclusion is applicable to the liquid phase. Indeed, in contrast to a relatively strong change of  $-\partial(\ln \rho_{\text{el}})/\partial P$  along the melting curve for liquid Fe (Fig. 1c), the corresponding slopes for both the fcc ( $< 10^{-3} \text{ GPa}^{-1}$ ) and hcp phases ( $< 4 \times 10^{-4} \text{ GPa}^{-1}$ ) are small, supporting the hypothesis of Stacey & Anderson (2001) to first order for the solid phases.

An interesting feature of the model is the predicted decrease of  $\rho_{\text{el}}^{\text{solid}}$  at the  $\gamma$ - $\varepsilon$ -liquid triple point. Resistivity generally decreases with increasing charge carrier density:  $\rho_{\text{el}}$  scales with  $\varrho$  between  $\propto \varrho^{-3}$  (eq. 2) and  $\propto \varrho^{-2}$  (eq. 4), depending on the implicit  $\varrho$ -dependence of  $S(q)$ . In Ziman's long wavelength approximation (eq. 2), this behaviour is captured both directly (increase in  $\varrho$ ) and indirectly, by  $\beta_T$  decreasing from the  $\gamma$  to the  $\varepsilon$  phase.

Although measurements of Ohta *et al.* (2016) confirm an increase of  $\rho_{\text{el}}$  upon melting up to 51 GPa within large uncertainties, their

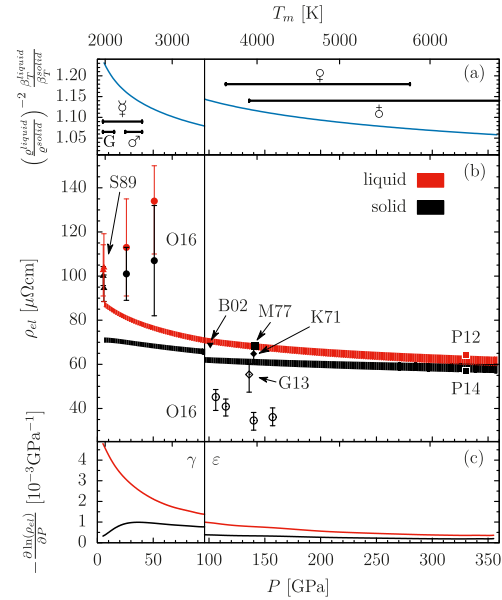


**Figure 1.** (a) Liquid to solid compressibility/density ratio for Fe along the melting curve from the thermodynamic model of Komabayashi (2014) used in Ziman's approximation (right-hand side of eq. 4). The lower x-axis label and ticks show pressure, the upper ones the corresponding melting temperature. Pressure intervals indicated correspond to core  $P$  in the terrestrial bodies of our solar system (Ganymede, Mercury, Mars, Venus and Earth). The vertical line represents the  $\gamma$ - $\varepsilon$ -liquid triple point in the model of Komabayashi (2014; 96 GPa and 3300 K). (b) Electrical resistivities in the liquid (red curve) and the solid (black curve) phases of Fe along the melting curve. For the liquid phase, the modified Bloch–Grüneisen fit from de Koker *et al.* (2012) has been evaluated along the melting curve, while the resistivity in the solid has been calculated using the ratios shown in panel (a) and applying eq. (4). The band widths take fitting uncertainties of the original Kubo–Greenwood results by de Koker *et al.* (2012) into account. Laboratory data (filled symbols) are by Secco & Schlössin (1989) (S89) and Ohta *et al.* (2016) (O16) from static experiments, and by Bi *et al.* (2002) (B02), Keeler (1971) (K71) and Matassov (1977) (M77) from shock wave experiments. For  $\rho_{\text{el}}^{\text{liquid}}$  and  $\rho_{\text{el}}^{\text{solid}}$ , data by Secco & Schlössin (1989) and Ohta *et al.* (2016) up to 51 GPa have been fitted linearly in the liquid and solid regions, respectively, and extrapolated towards  $T_m$  from both sides (see Supporting Information Figs S1 and S2). For the shock wave experiments, the lowest  $P$  point by Bi *et al.* (2002) and the highest  $P$  point each by Keeler (1971) and Matassov (1977) have been used, all for the solid phase. Temperatures along the Hugoniot at these pressures (Brown & McQueen 1986) are significantly below the melting point. Open circles in the  $P$ -range between 100 and 160 GPa show values calculated from combined Bloch–Grüneisen/resistivity-saturation fit parameters given in Ohta *et al.* (2016) and evaluated at  $T_m$  of Komabayashi (2014). G13 (open diamond) represents the high  $T$  extrapolation of a room temperature DAC experiment reported in Gomi *et al.* (2013), also taking resistivity saturation into account. At inner core boundary  $P$ , the Kubo–Greenwood results by Pozzo *et al.* (2012, 2014) (P12 and P14) are included for liquid and solid Fe, respectively. (c) Negative logarithmic derivative  $-\partial(\ln \rho_{\text{el}})/\partial P$  for liquid and solid iron along its melting curve. While the  $P$ -gradient is significant in the liquid, it is negligible in the solid, particularly for  $\varepsilon$ -Fe.

absolute values suggest  $\rho_{\text{el}}$  to increase as a function of  $P$  for the  $\gamma$ -phase along  $T_m$ . This is neither consistent with an expected decrease of  $\rho_{\text{el}} \propto Q^{-2 \dots -3}$ , nor in quantitative agreement with KG results. Resistivities computed with the Bloch-Grüneisen/resistivity saturation model of Ohta *et al.* (2016) for  $\varepsilon$ -Fe at  $P > 100$  GPa, where  $\varepsilon$ -Fe coexists with the liquid along the melting curve, show the expected decrease of  $\rho_{\text{el}}^{\text{solid}}$  with  $P$  within the uncertainties. Absolute values, however, are significantly smaller than KG results, estimates from Ziman's approximation and shock wave experiments (Bi *et al.* 2002; Keeler 1971; Matassov 1977; Fig. 1). Gomi *et al.* (2013) reported  $\rho_{\text{el}}$  of  $\varepsilon$ -Fe based on DAC experiments at 300 K. Although their model also takes resistivity saturation into account, their predicted value at core mantle boundary pressure plots significantly higher than those of Ohta *et al.* (2016) and is consistent with our model.

The resistivity contrast across the  $\varepsilon$ -liquid phase boundary decreases gradually towards higher  $P$ . For ICB pressure and  $T_m = 6382$  K (Komabayashi 2014), Ziman's approximation yields a value of  $58 \pm 2 \mu\Omega \text{ cm}$  for solid  $\varepsilon$ -iron, which is only marginally different from the  $62 \pm 2 \mu\Omega \text{ cm}$  in the liquid phase (increase on melting by 7 per cent). At comparable  $T$  (6350 K), Pozzo *et al.* (2014) computed solid resistivity values slightly lower than our result for pure iron ( $57 \mu\Omega \text{ cm}$ ), which—in combination with their value for liquid Fe of  $64 \mu\Omega \text{ cm}$  (Pozzo *et al.* 2012)—yields a discontinuity of 12 per cent.

As no reliable thermodynamic model for Co is currently available, we are not able to test whether the recently reported resistivity data by Ezenwa & Secco (2017b) follow the relation of eq. (5) at high  $P$  as well as it does at ambient pressure (Supporting Information Table S4).

### 3.3 Influence of light element partitioning

With the addition of light element impurities, such as Si, O, S or C, resistivity will increase with impurity concentration. Although Matthiessen's rule will be violated close to saturation resistivity (Gomi *et al.* 2016), this general behaviour continues to hold for compositions in the Fe–O–Si system for both the liquid (de Koker *et al.* 2012; Pozzo *et al.* 2013) and the solid (Pozzo *et al.* 2014). Since light elements can dissolve in higher concentration in the liquid than in the solid and lead to a depression of the liquidus  $T$  in the binary system (Anderson & Ahrens 1994; Alfè *et al.* 2002), our method cannot be easily applied to the Earth's core.

We can, however, compare the estimated  $\rho_{\text{el}}^{\text{solid}}$  of pure Fe and  $\rho_{\text{el}}^{\text{liquid}}$  of selected alloys. As a result of light element segregation into the liquid OC, the resistivity contrast is significantly enhanced compared to pure iron. When we combine our estimate for  $\rho_{\text{el}}$  of solid Fe at the ICB pressure of  $\sim 58 \mu\Omega \text{ cm}$  with that of liquid Fe<sub>0.82</sub>Si<sub>0.10</sub>O<sub>0.08</sub> of  $79 \mu\Omega \text{ cm}$  (Pozzo *et al.* 2014) or  $75 \mu\Omega \text{ cm}$  for liquid Fe<sub>7</sub>Si (de Koker *et al.* 2012), resistivity in the OC would be larger than in the IC by 29–36 per cent.

Although the influence of IC resistivity on the frequency of global field reversals is controversial as we discuss in the Introduction, a change of  $\rho_{\text{el}}$  at the ICB provides an important constraint on the boundary conditions of dynamo simulations. By using the discontinuity of  $\rho_{\text{el}}$ , its possible effect on the magnetic field could be explored for terrestrial planets up to the pressure of the Earth's IC. It is worth noting that the applicability of the model is neither limited by the size of the IC nor the  $P$  at the ICB, which makes it viable for models that include a growing IC.

## 4 CONCLUSIONS

Having analysed data for isothermal compressibility and electrical resistivity at ambient  $P$ , we find that the increase of electrical resistivity of iron upon melting can be represented by a change of  $Q$  and  $S(Q)$  in the long-wavelength limit to first order. High  $P$  experiments (Secco & Schlössin 1989; Deng *et al.* 2013; Ohta *et al.* 2016) and the computational work of Pozzo *et al.* (2012, 2014) indicate that a change of electrical resistivity persists along and across the melting curve. Knowing five out of six quantities on both sides of the melting curve in Ziman's approximation (eq. 5), this observation allows for a first order estimate of the remaining quantity. We combine DFT-MD results for  $\rho_{\text{el}}^{\text{liquid}}$  (de Koker *et al.* 2012) and the compressibility/density ratio in eq. (4) from a thermodynamic model of Fe (Komabayashi 2014) to compute  $\rho_{\text{el}}^{\text{solid}}$  along the melting curve of iron up to 360 GPa.

For planetary cores, the difference in electrical resistivity is likely to be amplified by differences in chemical composition across an ICB, since light elements prefer to remain in solution in the OC. This difference might be as large as 36 per cent for the Earth's core. As long as the pressure of a growing IC does not cross a solid-solid phase boundary,  $\rho_{\text{el}}^{\text{solid}}$  at the ICB remains approximately constant, as suggested by Stacey & Anderson (2001).

## ACKNOWLEDGEMENTS

Data to produce the results of this manuscript are contained in this manuscript, the Supporting Information or in the corresponding references. This work was supported by the German Science Foundation (DFG) in the Focus Program Planetary Magnetism (SPP 1488, STE1105/10-1). We greatly appreciate helpful discussion on Ziman's theory with Vojtěch Vlček and Philipp Sperling and on implications for planetary dynamos with Johannes Wicht. Comments of anonymous reviewers helped to significantly improve the manuscript.

## REFERENCES

- Alfè, D., Gillan, M.J. & Price, G.D., 2002. Composition and temperature of the Earth's core constrained by combining *ab initio* calculations and seismic data, *Earth planet Sci. Lett.*, **195**, 91–98.
- Anderson, B.J. *et al.*, 2011. The global magnetic field of Mercury from MESSENGER orbital observations, *Science*, **333**, 1859–1862.
- Anderson, W. & Ahrens, T., 1994. An equation of state for liquid iron and implications for the Earth's core, *J. geophys. Res.*, **99**, 4273–4284.
- Ashcroft, N.W. & Lekner, J., 1966. Structure and resistivity of liquid metals, *Phys. Rev.*, **145**, 83–90.
- Assael, M.J. *et al.*, 2006. Reference data for the density and viscosity of liquid aluminum and liquid iron, *J. Phys. Chem. Ref. Data*, **35**, 285–300.
- Basinski, Z.S., Hume-Rothery, W. & Sutton, A.L., 1955. The lattice expansion of iron, *Proc. R. Soc. A*, **229**, 459–467.
- Bi, Y., Tan, H. & Jing, F., 2002. Electrical conductivity of iron under shock compression up to 200 GPa, *J. Phys.: Condens. Matter*, **14**, 10 849–10 854.
- Blumm, J. & Henderson, J. B., 2000. Measurement of the volumetric expansion and bulk density of metals in the solid and molten regions, *High Temp. – High Press.*, **32**, 109–113.
- Brown, J.M. & McQueen, R.G., 1986. Phase transitions, Grüneisen parameter, and elasticity for shocked iron between 77 GPa and 400 GPa, *J. geophys. Res.*, **91**, 7485–7494.
- Brown, J.M., Fritz, J.N. & Hixson, R.S., 2000. Hugoniot data for iron, *J. Appl. Phys.*, **88**, 5496–5498.

- Burrill, D.J., Feinblum, D.V., Charest, M.R.J. & Starrett, C.E., 2016. Comparison of electron transport calculations in warm dense matter using the Ziman formula, *High Energy Dens. Phys.*, **19**, 1–10.
- Casas, J., Keita, N.M. & Steinemann, S.G., 1984. Sound velocity in liquid titanium, vanadium and chromium, *Phys. Chem. Liq.*, **14**, 155–158.
- Cezairliyan, A. & McClure, J.L., 1974. Thermophysical measurements on iron above 1500 K using a transient (subsecond) technique, *J. Res. Nat. Bur. Stds.*, **78A**, 1–4.
- Cheung, J. & Ashcroft, N.W., 1978. Resistivity of liquid metals under elevated pressure, *Phys. Rev. B*, **18**, 559–568.
- de Koker, N., Steinle-Neumann, G. & Vlček, V., 2012. Electrical resistivity and thermal conductivity of liquid Fe alloys at high P and T, and heat flux in Earth's core, *Proc. Natl. Acad. Sci. USA*, **109**, 4070–4073.
- Deng, L.W., Seagle, C., Fei, Y.W. & Shahar, A., 2013. High pressure and temperature electrical resistivity of iron and implications for planetary cores, *Geophys. Res. Lett.*, **40**, 33–37.
- Desai, P.D., 1986. Thermodynamic properties of iron and silicon, *J. Phys. Chem. Ref. Data*, **15**, 967–983.
- Dever, D.J., 1972. Temperature dependence of the elastic constants in  $\alpha$ -iron single crystals: relationship to spin order and diffusion anomalies, *J. Appl. Phys.*, **43**, 3293–3301.
- Dharmaraj, G. & Stanley, S., 2012. Effect of inner core conductivity on planetary dynamo models, *Phys. Earth planet. Inter.*, **212**, 1–9.
- Dobson, D., 2016. Earth's core problem, *Nature*, **534**, 45.
- Drchal, V., Kudrnovský, J., Wagenknecht, D., Turek, I. & Khmelevskiy, S., 2017. Transport properties of iron at Earth's core conditions: the effect of spin disorder, *Phys. Rev. B*, **96**, 024432, 1–4.
- Drotning, W.D., 1981. Thermal expansion of iron, cobalt, nickel, and copper at temperatures up to 600 K above melting, *High Temp. – High Press.*, **13**, 441–458.
- Dziewonski, A.M. & Anderson, D.L., 1981. Preliminary reference Earth model, *Phys. Earth planet. Inter.*, **25**, 297–356.
- Ezenwa, I.C. & Secco, R.A., 2017a. Constant electrical resistivity of Zn along the melting boundary up to 5 GPa, *High Press. Res.*, **37**, 319–333.
- Ezenwa, I.C. & Secco, R.A., 2017b. Invariant electrical resistivity of Co along the melting boundary, *Earth planet. Sci. Lett.*, **474**, 120–127.
- Ezenwa, I.C., Secco, R.A., Yong, W., Pozzo, M. & Alfè, D., 2017. Electrical resistivity of solid and liquid Cu up to 5 GPa: Decrease along the melting boundary, *J. Phys. Chem. Solids*, **110**, 386–393.
- Glatzmaier, G.A. & Roberts, P.H., 1995. A three-dimensional convective dynamo solution with rotating and finitely conducting inner core and mantle, *Phys. Earth planet. Inter.*, **91**, 63–75.
- Gomi, H., Ohta, K., Hirose, K., Labrosse, S., Caracas, R., Verstraete, M.J. & Hernlund, J.W., 2013. The high conductivity of iron and thermal evolution of the Earth's core, *Phys. Earth planet. Inter.*, **224**, 88–103.
- Gomi, H., Hirose, K., Akai, H. & Fei, Y., 2016. Electrical resistivity of substitutionally disordered hcp Fe-Si and Fe-Ni alloys: Chemically-induced resistivity saturation in the Earth's core, *Earth planet. Sci. Lett.*, **451**, 51–61.
- Hashin, Z. & Shtrikman, S., 1963. Conductivity of Polycrystals, *Phys. Rev.*, **130**, 129–133.
- Hixson, R.S., Winkler, M.A. & Hodgdon, M.L., 1990. Sound speed and thermophysical properties of liquid iron and nickel, *Phys. Rev. B*, **42**, 6485–6491.
- Hollerbach, R. & Jones, C.A., 1993. A geodynamo model incorporating a finitely conducting inner core, *Phys. Earth planet. Inter.*, **75**, 317–327.
- Ichikawa, H., Tsuchiya, T. & Tange, Y., 2014. The P-V-T equation of state and thermodynamic properties of liquid iron, *J. geophys. Res.*, **119**, 240–252.
- Jain, A. & Evans, R., 1971. Calculation of the electrical resistivity of liquid iron in the Earth's core, *Nat. Phys. Sci.*, **235**, 165–167.
- Keeler, R.N., 1971. Electrical conductivity of condensed media at high pressures, in *Physics of High Energy Density*, Vol. 48, pp. 106–125, eds Caldirola, P. & Knoepel, H., Academic.
- Kirshenbaum, A.D. & Cahill, J.A., 1962. The Density of liquid iron from the melting point to 2500 K, *Trans. Metall. AIME*, **224**, 816–819.
- Komabayashi, T., 2014. Thermodynamics of melting relations in the system Fe-FeO at high pressure: Implications for oxygen in the Earth's core, *J. geophys. Res.*, **119**, 4164–4177.
- Komabayashi, T. & Fei, Y., 2010. Internally consistent thermodynamic database for iron to the Earth's core conditions, *J. geophys. Res.*, **115**, B03202, 1–12.
- Lhuillier, F., Hulot, G. & Gallet, Y., 2013. Statistical properties of reversals and chrons in numerical dynamos and implications for the geodynamo, *Phys. Earth planet. Inter.*, **220**, 19–36.
- March, N.H., 1990. *Liquid Metals: Concepts and Theory*, Cambridge Univ. Press.
- Matassov, G., 1977. The Electrical Conductivity of Iron-Silicon Alloys at High Pressures and the Earth's Core, *PhD thesis*, University of California.
- Merrill, R.T., McElhinny, M.W. & McFadden, P.L., 1996. *The Magnetic Field of the Earth: Paleo-magnetism, the Core and the Deep Mantle*, Academic Press.
- Mott, N.F., 1972. The Electrical Resistivity of Liquid Transition Metals, *Phil. Mag.*, **26**, 1249–1261.
- Nasch, P.M. & Steinemann, S.G., 1995. Density and thermal expansion of molten manganese, iron, nickel, copper, aluminum and tin by means of the gamma-ray attenuation technique, *Phys. Chem. Liq.*, **29**, 43–58.
- Nasch, P.M., Manghnani, N.H. & Secco, R.A., 1994. Sound velocity measurements in liquid iron by ultrasonic interferometry, *J. geophys. Res.*, **99**, 4285–4291.
- Ohta, K., Kuwayama, Y., Hirose, K., Shimizu, K. & Ohishi, Y., 2016. Experimental determination of the electrical resistivity of iron at Earth's core conditions, *Nature*, **534**, 95–98.
- Olson, P. & Amit, H., 2014. Magnetic reversal frequency scaling in dynamos with thermochemical convection, *Phys. Earth planet. Inter.*, **229**, 122–133.
- Papaconstantopoulos, D.A., 1986. *Handbook of the Band Structure of Elemental Solids*, Plenum Press.
- Pozzo, M., Davies, C., Gubbins, D. & Alfè, D., 2012. Thermal and electrical conductivity of iron at Earth's core conditions, *Nature*, **485**, 355–358.
- Pozzo, M., Davies, C., Gubbins, D. & Alfè, D., 2013. Transport properties for liquid silicon-oxygen-iron mixtures at Earth's core conditions, *Phys. Rev. B*, **87**, 014110, 1–10.
- Pozzo, M., Davies, C., Gubbins, D. & Alfè, D., 2014. Thermal and electrical conductivity of solid iron and iron-silicon mixtures at Earth's core conditions, *Earth planet. Sci. Lett.*, **393**, 159–164.
- Saito, T., Shiraishi, Y. & Sakuma, Y., 1969. Density measurement of molten metals by levitation technique at temperatures between 1800° and 2200° C, *Trans. Iron Steel Inst. Japan*, **9**, 118–126.
- Sarson, G.R., Jones, C.A., Zhang, K. & Schubert, G., 1997. Magnetoconvection dynamos and the magnetic fields of Io and Ganymede, *Science*, **276**, 1106–1108.
- Schriempf, J.T., 1968. Thermal and electrical resistivities of Osmium from 2 to 20°K, *Solid State Commun.*, **6**, 873–876.
- Secco, R.A. & Schlössin, H.H., 1989. The electrical resistivity of solid and liquid Fe at pressures up to 7 GPa, *J. geophys. Res.*, **94**, 5887–5894.
- Stacey, F.D. & Anderson, O.L., 2001. Electrical and thermal conductivities of Fe-Ni-Si alloy under core conditions, *Phys. Earth planet. Inter.*, **124**, 153–162.
- Tateyama, R., Ohtani, E., Terasaki, H., Nishida, K., Shibazaki, Y., Suzuki, A. & Kikegawa, T., 2011. Density measurements of liquid Fe-Si alloys at high pressure using the sink-float method, *Phys. Chem. Miner.*, **38**, 801–807.
- Tsu, Y., Takano, K. & Shiraishi, Y., 1985. The velocities of ultrasound in molten iron, cobalt and nickel, *Bull. Res. Inst. Miner. Dressing Metall.*, **41**, 1–8.
- van Zytveld, J.B., 1980. Electrical resistivities of liquid transition metals, *J. Phys. Colloq.*, **41**, C8-503–C8-506.
- Vlček, V., de Koker, N. & Steinle-Neumann, G., 2012. Electrical and thermal conductivity of Al liquid at high pressures and temperatures from ab initio computations, *Phys. Rev. B*, **85**, 184201, 1–7.
- Volkenshteyn, N.V., Startsev, V.Y., Cherepanov, V.I., Azhazha, V.M., Kovtun, G.P. & Yelenskiy, V.A., 1978. Electric resistance anisotropy of Ruthenium

- and Rhenium single crystals at 2–300 K, *Fiz. Met. Metalloved.*, **45**, 1187–1199.
- Waseda, Y. & Ohtani, M., 1974. Static structure of liquid noble and transition metals by X-ray diffraction, *Phys. Status Solidi b*, **62**, 535–546.
- Wertheim, M.S., 1963. Exact solution of the Percus-Yevick integral equation for hard spheres, *Phys. Rev. Lett.*, **10**, 321–323.
- Wicht, J., 2002. Inner-core conductivity in numerical dynamo simulations, *Phys. Earth planet. Inter.*, **132**, 281–302.
- Williams, Q., 2009. Bottom-up versus top-down solidification of the cores of small solar system bodies: constraints on paradoxical cores, *Earth planet. Sci. Lett.*, **284**, 564–569.
- Ziman, J.M., 1961. A theory of the electrical properties of liquid metals. I. The monovalent metals, *Phil. Mag.*, **6**, 1013–1034.

## SUPPORTING INFORMATION

Supplementary data are available at [GJI](http://gji.oup.com) online.

- Figure S1.** Electrical resistivity as a function of  $T$  for pure iron at high  $P$  as reported by Secco & Schlössin (1989). Thick vertical lines indicate  $T_m$  from the model of Komabayashi (2014). Dashed lines represent the linear fit in both liquid and solid, which has been used to extrapolate towards  $T_m$  and determine the discontinuity there.
- Figure S2.** Electrical resistivity as a function of  $T$  for pure iron at high  $P$  as reported by Ohta et al. (2016). Thick vertical lines indicate  $T_m$  from the model of Komabayashi (2014). Dashed lines represent the linear fit in both liquid and solid, which has been used to extrapolate towards  $T_m$  and determine the discontinuity there.
- Figure S3.** Fermi level from DFT-MD simulations of liquid Fe as a function of  $(V/V_0)^{-2/3}$ . The offset at zero density is due to the ambiguity of the energy zero in DFT-MD.
- Figure S4.**  $S(q)$  of liquid Fe in the long wavelength region at ambient  $P$  and three different  $T$ , measured by Waseda & Ohtani (1974). The solid lines represent a fit to the data up to  $1.5 \text{ \AA}^{-1}$  with a Percus-Yevick expression of the structure factor of a hard sphere liquid.
- Figure S5.** Isothermal bulk modulus  $K_T$  as a function of  $T$ . Red circles have been obtained by fitting a Percus-Yevick expression of the hard-sphere structure factor up to  $1.5 \text{ \AA}^{-1}$  to data by Waseda & Ohtani (1974), and extrapolating to the thermodynamic limit  $\lim_{q \rightarrow 0} S(q) = \rho k_B T / K_T$  (Figure 4). They agree well with the model of Komabayashi (2014) (red line) within the error. Considerable uncertainties due to the extrapolation towards  $q \rightarrow 0$  propagate to a large uncertainty for  $K_T$  at  $T_m$ . However, the  $S(q)$ -based data provide strong support for a thermal expansivity  $\alpha$  of  $\sim 0.9 \cdot 10^{-4} \text{ K}^{-1}$ , as

long as two physical constraints are met: (a)  $\partial K_T / \partial T < 0$  in the liquid and (b)  $K_T^{\text{liquid}} < K_T^{\text{solid}}$  (black square) at  $T_m$ . The other red symbols refer to values of  $\beta_T^{\text{liquid}}$  (Table 1 in the paper), obtained by different datasets for density  $\rho$  and thermal expansivity  $\alpha$  of liquid Fe at  $T_m$  and ambient  $P$ .

**Figure S6.** Relative deviations [%] of densities from shock wave experiments (Brown & McQueen 1986; Brown et al. 2000) from the liquid Fe model of Komabayashi (2014). For  $P$  larger than 260 GPa, the Hugoniot lies in the liquid stability field of iron.

**Table S1.** Electrical resistivities of Fe along the melting curve based on extrapolation of high  $P$  data, as shown in Figures 1 and 2. Lower  $P$  values correspond to data of Secco & Schlössin (1989), higher  $P$  values to data of Ohta et al. (2016). Uncertainties have been determined from errors of the linear fit towards  $T_m$ .

**Table S2.** Single crystal electrical resistivity of the group 8 elements Ru (Volkenshteyn et al. 1978) and Os (Schriempf 1968) at room temperature, Hashin-Shtrikman bounds (Hashin & Shtrikman 1963) for their polycrystal resistivity and maximum relative error due to anisotropy.

**Table S3.** Thermophysical properties of simple metals at  $T_m$ . The resistivity ratio is in good agreement with the long-wavelength approximation to Ziman's formula (equation 5). References are labeled as follows: Sobolev (2011)<sup>a</sup>, Faber (1972)<sup>b</sup>, Fritsch et al. (1973)<sup>c</sup>, Blairs (2006)<sup>d</sup>, Peng et al. (2015)<sup>e</sup>, Mills (2002)<sup>f</sup>, Tallon & Wolfenden (1979)<sup>g</sup>.

**Table S4.** Thermophysical properties of transition metals with partially occupied  $d$ -bands at  $T_m$ . The resistivity ratio is in good agreement with the long-wavelength approximation to Ziman's formula (equation 5). References are labeled as follows: Faber (1972)<sup>b</sup>, Hess et al. (1994)<sup>h</sup>, Tsu et al. (1985)<sup>i</sup>, Schramm (1962)<sup>j</sup>, Brillo & Egry (2003)<sup>k</sup>, Owen & Yates (1936)<sup>l</sup>, Desai (1987)<sup>m</sup>, Alers et al. (1960)<sup>n</sup>.

**Table S5.** Thermophysical properties of metals with fully occupied  $d$ -bands at  $T_m$ . The resistivity ratio is systematically underestimated by Ziman's long-wavelength approximation (equation 5). References are labeled as follows: Faber (1972)<sup>b</sup>, Blairs (2006)<sup>d</sup>, Owen & Yates (1934)<sup>l</sup>, Chang & Himmel (1966)<sup>o</sup>, Kanai & Tsuchiya (1993)<sup>p</sup>, Grønvold & Stølen (2003)<sup>q</sup>, Ledbetter (1977)<sup>r</sup>.

Please note: Oxford University Press is not responsible for the content or functionality of any supporting materials supplied by the authors. Any queries (other than missing material) should be directed to the corresponding author for the paper.

# Supporting Information for ”Electrical resistivity discontinuity of iron along the melting curve”

Fabian Wagle<sup>1</sup>

Gerd Steinle-Neumann<sup>1</sup>

<sup>1</sup> *Bayerisches Geoinstitut, Universität Bayreuth, Germany*

## Contents of this file

- (i) Figures S1 to S6
- (ii) Tables S1 to S5

## Additional Supporting Information (File uploaded separately)

- (i) Wolfram Mathematica<sup>®</sup> notebook

## Introduction

The Supporting Online Material contains the following information:

- Two figures (Figures S1 and S2), showing published experimental results of  $\rho_{el}(T)$  at high  $P$  in order to determine the resistivity discontinuity at the melting point ( $T_m$ ).
- One figure (Figure S3), showing the free-electron-like volume dependence of the Fermi level of liquid Fe.
- One figure (Figure S4), showing  $S(q)$  at ambient  $P$  and three different  $T$  in the long-wavelength region.
- One figure (Figure S5), showing the isothermal bulk moduli ( $K_T$ ) from the thermodynamic limit of the structure factor  $S(q \rightarrow 0)$  in comparison to  $K_T$  from the model of *Komabayashi* (2014) and  $K_T$  from other experiments at ambient  $P$ .
- One figure (Figure S6), comparing densities from shock experiments with the model of *Komabayashi* (2014) for liquid Fe.
- One table (Table S1), presenting resistivities of Fe at the melting point based on extrapolation of high  $P$  data, as shown in Figures S1 and S2.

2 *Fabian Wagle and Gerd Steinle-Neumann*

- One table (Table S2), presenting single crystal resistivities of Ru and Os and their polycrystal bounds.
- Three tables (Tables S3-S5), presenting a systematic evaluation of equation (5) for some simple, transition and noble metals.
- One Wolfram Mathematica<sup>®</sup> notebook in which the thermodynamic model of *Komabayashi* (2014) used in the manuscript is implemented.

## REFERENCES

- Alers, G. A., Neighbours, J. R. & Sato, H., 1960. Temperature dependent magnetic contributions to the high field elastic constants of Nickel and an Fe–Ni alloy, *J. Phys. Chem. Solids*, **13**, 40–55.
- Blairs, S. (2006), Correlation between surface tension, density, and sound velocity of liquid metals, *J. Coll. Inter. Sci.*, *302*, 312–314.
- Brillo, J. & Egly, I., 2003. Density Determination of Liquid Copper, Nickel, and Their Alloys, *Int. J. Thermophys.*, **24**, 1155–1170.
- Brown, J. M. & McQueen, R. G., 1986. Phase Transitions, Grüneisen Parameter, and Elasticity for Shocked Iron Between 77 GPa and 400 GPa, *J. Geophys. Res.*, **91**, 7485–7494.
- Brown, J. M., Fritz, J. N. & Hixson, R. S., 2000. Hugoniot data for iron, *J. Appl. Phys.*, **88**, 5496–5498.
- Chang, Y. A. & Himmel, L., 1966. Temperature Dependence of the Elastic Constants of Cu, Ag, and Au above Room Temperature, *J. Appl. Phys.*, **37**, 3567–3572.
- Desai, P. D. (1987), Thermodynamic properties of nickel, *Int. J. Thermophys.*, *8*, 763–780.
- Faber, T. E. (1972), *Theory of Liquid Metals*, Cambridge University Press, Cambridge.
- Fernández Guillermet, A., 1987. Critical Evaluation of the Thermodynamic Properties of Cobalt, *Int. J. Thermophys.*, **8**, 481–510.
- Fritsch, G., Geipel, F. & Prasetyo, A., 1973. The Elastic Constants of Sodium from 20 to 95°C, *J. Phys. Chem. Solids*, **34**, 1961–1969.
- Grønvold, F. & Stølen, S., 2003. Heat capacity of solid zinc from 298.15 to 692.68 K and of liquid zinc from 692.68 to 940 K: thermodynamic function values, *Thermochim. Acta*, **395**, 127–131.
- Hashin, Z. & Shtrikman, S., 1963. Conductivity of Polycrystals, *Phys. Rev.*, **130**, 129–133.
- Hess, H., Kaschnitz, E. & Pottlacher, G., 1994. Thermophysical properties of liquid cobalt, *High Pressure Research*, **12**, 29–42.
- Kanai, S. & Tsuchiya, Y., 1993. Sound Velocity in the Liquid Bismuth-Zinc System, *J. Phys. Soc. Jpn.*, **62**, 2388–2394.
- Komabayashi, T., 2014. Thermodynamics of melting relations in the system Fe–FeO at high pressure: Implications for oxygen in the Earth’s core, *J. Geophys. Res.*, **119**, 4164–4177.
- Ledbetter, H. M. (1977), Elastic Properties of Zinc: A Compilation and a Review, *J. Phys. Chem. Ref. Data*, *6*, 1181–1203.
- Mills, K. C. (2002), *Recommended Values of Thermophysical Properties for Selected Commercial Alloys*, Woodhead Publishing Ltd, Cambridge, United Kingdom, 2002, 19–25.
- Ohta, K., Kuwayama, Y., Hirose, K., Shimizu, K. & Ohishi, Y., 2016. Experimental determination of the electrical resistivity of iron at Earth’s core conditions, *Nature*, **534**, 95–98.
- Owen, E. A. & Yates, E. L., 1934. The thermal expansion of the crystal lattices of silver, platinum and zinc, *Philos. Mag.*, **17**, 113–131.
- Owen, E. A. & Yates, E. L., 1936. X-ray measurement of the thermal expansion of pure nickel, *Philos. Mag.*, **21**, 809–819.

4 Fabian Wagle and Gerd Steinle-Neumann

- Peng, H. L., Voigtmann, Th., Kollang, G., Kobatake, H. & Brillo, J., 2015. Structural and dynamical properties of liquid Al-Au alloys, *Phys. Rev. B*, **92**, 184201.
- Schramm, K.-H. (1962), Daten zur Temperaturabhängigkeit des Kompressionsmoduls reiner Metalle, *Z. Metallkde.*, **53**, 316–320.
- Schriempf, J. T., 1968. Thermal and electrical resistivities of Osmium from 2 to 20°K, *Solid State Commun.*, **6**, 873–876.
- Secco, R. A. & Schlössin, H. H., 1989. The electrical resistivity of solid and liquid Fe at pressures up to 7 GPa, *J. Geophys. Res.*, **94**, 5887–5894.
- Sobolev, V., 2011. Database of thermophysical properties of liquid metal coolants for GEN-IV – Sodium, lead, lead-bismuth eutectic (and bismuth), *Scientific report of the SCK-CEN*, Belgium.
- Tallon, J. L. & Wolfenden, A., 1979. Temperature Dependence of the Elastic Constants of Aluminum, *J. Phys. Chem. Solids*, **40**, 831–837.
- Tsu, Y., K. Takano, and Y. Shiraishi (1985), The velocities of ultrasound in molten iron, cobalt and nickel, *Res. Inst. Min. Dress. Met.*, **41**.
- Volkenshteyn, N. V., Startsev, V. Y., Cherepanov, V. I., Azhazha, V. M., Kovtun, G. P. & Yelenskiy, V. A., 1978. Electric resistance anisotropy of Ruthenium and Rhenium single crystals at 2-300 K, *Phys. Met. Metallogr.*, **45**, 1187–1199.
- Waseda, Y. & Ohtani, M., 1974. Static Structure of Liquid Noble and Transition Metals by X-Ray Diffraction, *Phys. Stat. Sol. (b)*, **62**, 535–546.

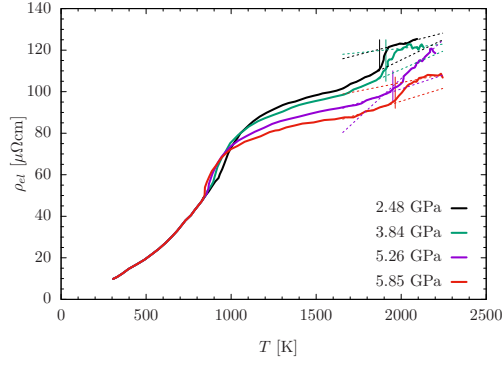


**Figure S1.** Electrical resistivity as a function of  $T$  for pure iron at high  $P$  as reported by *Secco & Schlössin* (1989). Thick vertical lines indicate  $T_m$  from the model of *Komabayashi* (2014). Dashed lines represent the linear fit in both liquid and solid, which has been used to extrapolate towards  $T_m$  and determine the discontinuity there.

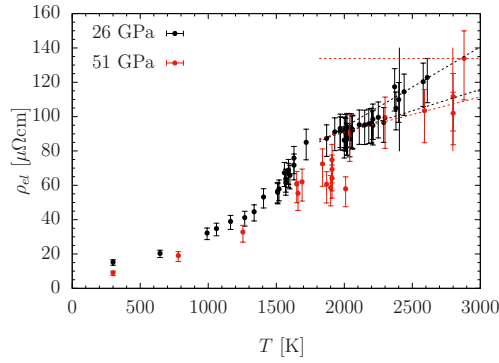


**Figure S2.** Electrical resistivity as a function of  $T$  for pure iron at high  $P$  as reported by *Ohta et al.* (2016). Thick vertical lines indicate  $T_m$  from the model of *Komabayashi* (2014). Dashed lines represent the linear fit in both liquid and solid, which has been used to extrapolate towards  $T_m$  and determine the discontinuity there.

6 Fabian Wagle and Gerd Steinle-Neumann

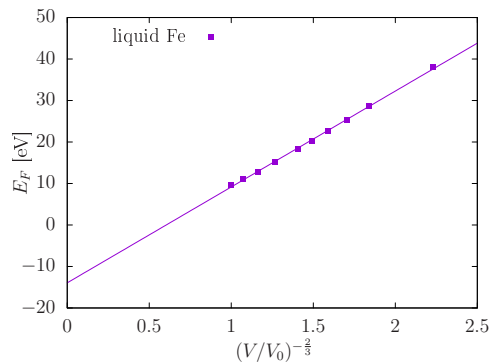


**Figure S3.** Fermi level from DFT-MD simulations of liquid Fe as a function of  $(V/V_0)^{-2/3}$ . The offset at zero density is due to the ambiguity of the energy zero in DFT-MD.

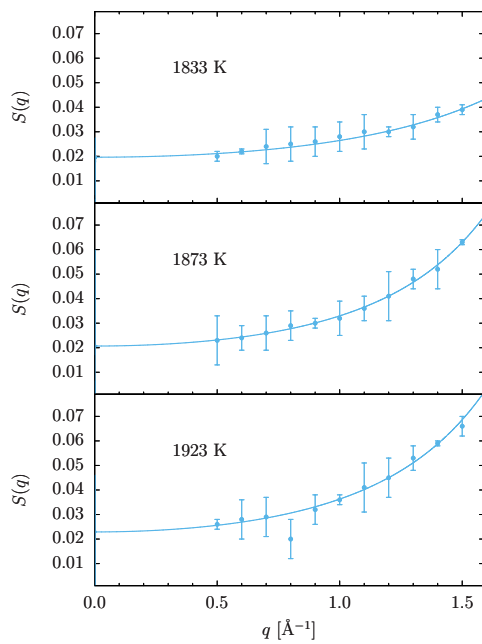


**Figure S4.**  $S(q)$  of liquid Fe in the long wavelength region at ambient  $P$  and three different  $T$ , measured by *Waseda & Ohtani (1974)*. The solid lines represent a fit to the data up to  $1.5 \text{ \AA}^{-1}$  with a Percus-Yevick expression of the structure factor of a hard sphere liquid.

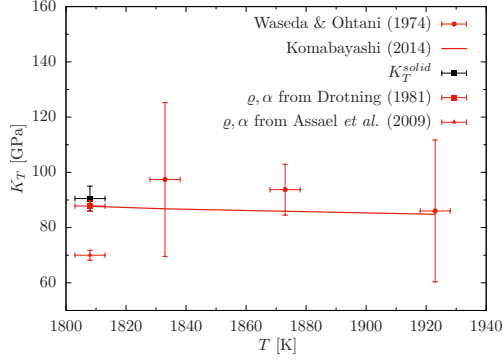


**Figure S5.** Isothermal bulk modulus  $K_T$  as a function of  $T$ . Red circles have been obtained by fitting a Percus-Yevick expression of the hard-sphere structure factor up to  $1.5 \text{ \AA}^{-1}$  to data by *Waseda & Ohtani* (1974), and extrapolating to the thermodynamic limit  $\lim_{q \rightarrow 0} S(q) = \rho k_B T / K_T$  (Figure S4). They agree well with the model of *Komabayashi* (2014) (red line) within the error. Considerable uncertainties due to the extrapolation towards  $q \rightarrow 0$  propagate to a large uncertainty for  $K_T$  at  $T_m$ . However, the  $S(q)$ -based data provide strong support for a thermal expansivity  $\alpha$  of  $\sim 0.9 \cdot 10^{-4} \text{ K}^{-1}$ , as long as two physical constraints are met: (a)  $\partial K_T / \partial T < 0$  in the liquid and (b)  $K_T^{liquid} < K_T^{solid}$  (black square) at  $T_m$ . The other red symbols refer to values of  $\beta_T^{liquid}$  (Table 1 in the paper), obtained by different datasets for density  $\rho$  and thermal expansivity  $\alpha$  of liquid Fe at  $T_m$  and ambient  $P$ .

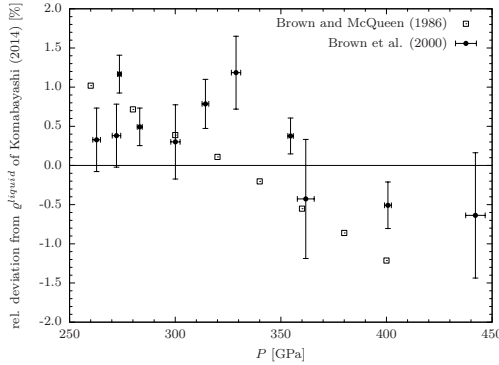


**Figure S6.** Relative deviations [%] of densities from shock wave experiments (*Brown & McQueen* 1986; *Brown et al.* 2000) from the liquid Fe model of *Komabayashi* (2014). For  $P$  larger than 260 GPa, the Hugoniot lies in the liquid stability field of iron.

8 *Fabian Wagle and Gerd Steinle-Neumann*

**Table S1.** Electrical resistivities of Fe along the melting curve based on extrapolation of high  $P$  data, as shown in Figures S1 and S2. Lower  $P$  values correspond to data of *Secco & Schlössin* (1989), higher  $P$  values to data of *Ohta et al.* (2016). Uncertainties have been determined from errors of the linear fit towards  $T_m$ .

$P$ [GPa]	$T_m$ [K]	$\rho_{el}^{liquid}$ [ $\mu\Omega\text{cm}$ ]	$\rho_{el}^{solid}$ [ $\mu\Omega\text{cm}$ ]	$\frac{\rho_{el}^{liquid}}{\rho_{el}^{solid}}$
2.48	1873	$120 \pm 7$	$110 \pm 2$	$1.09 \pm 0.07$
3.84	1910	$120 \pm 15$	$108 \pm 4$	$1.12 \pm 0.14$
5.26	1951	$103 \pm 12$	$100 \pm 4$	$1.03 \pm 0.12$
5.84	1965	$104 \pm 15$	$95 \pm 6$	$1.10 \pm 0.18$
26	2405	$113 \pm 22$	$101 \pm 12$	$1.1 \pm 0.3$
51	2798	$134^{+16}_{-24}$	$107 \pm 25$	$1.3 \pm 0.3$

**Table S2.** Single crystal electrical resistivity of the group 8 elements Ru (*Volkenshteyn et al.* 1978) and Os (*Schriempf* 1968) at room temperature, Hashin-Shtrikman bounds (*Hashin & Shtrikman* 1963) for their polycrystal resistivity and maximum relative error due to anisotropy.

	$\rho_{el}^{\parallel}$ [ $\mu\Omega\text{cm}$ ]	$\rho_{el}^{\perp}$ [ $\mu\Omega\text{cm}$ ]	$\rho_{el}^{upper}$ [ $\mu\Omega\text{cm}$ ]	$\rho_{el}^{lower}$ [ $\mu\Omega\text{cm}$ ]	$\rho_{el}^{avg}$ [ $\mu\Omega\text{cm}$ ]	rel. deviation [%]
Ru	5.15	6.65	6.15	6.06	6.11	0.8
Os	6.32	9.48	8.43	8.13	8.28	1.8

**Table S3.** Thermophysical properties of simple metals at  $T_m$ . The resistivity ratio is in good agreement with the long-wavelength approximation to Ziman’s formula (equation 5). References are labeled as follows: *Sobolev (2011)*<sup>a</sup>, *Faber (1972)*<sup>b</sup>, *Fritsch et al. (1973)*<sup>c</sup>, *Blairs (2006)*<sup>d</sup>, *Peng et al. (2015)*<sup>e</sup>, *Mills (2002)*<sup>f</sup>, *Tallon & Wolfenden (1979)*<sup>g</sup>.

		liquid	solid	$\frac{\rho_{el}^{liquid}}{\rho_{el}^{solid}} \left( \frac{\rho^{liquid}}{\rho^{solid}} \right)^2 \left( \frac{\beta_T^{liquid}}{\beta_T^{solid}} \right)^{-1}$
	$v_p$ [km s <sup>-1</sup> ]	2.53 <sup>a</sup>		
	$\rho$ [g cm <sup>-3</sup> ]	0.93 <sup>a</sup>	0.95 <sup>a,b</sup>	
	$\alpha$ [10 <sup>-5</sup> K <sup>-1</sup> ]	25.4 <sup>a</sup>		
<b>Na</b>	$c_P$ [J g <sup>-1</sup> K <sup>-1</sup> ]	1.43 <sup>a</sup>		<b>1.1</b>
	$\beta_T$ [GPa <sup>-1</sup> ]	1/5.3	1/6.5 <sup>c</sup>	
	$T_m$ [K]	371 <sup>b</sup>		
	$\rho_{el}^{liquid} / \rho_{el}^{solid}$	1.45 <sup>b</sup>		
	$v_p$ [km s <sup>-1</sup> ]	4.56 <sup>d</sup>		
	$\rho$ [g cm <sup>-3</sup> ]	2.29 <sup>e</sup>	2.56 <sup>f</sup>	
	$\gamma$	1.45 <sup>d</sup>		
<b>Al</b>	$\beta_T$ [GPa <sup>-1</sup> ]	1/34	1/56 <sup>g</sup>	<b>1.0</b>
	$T_m$ [K]	933 <sup>b</sup>		
	$\rho_{el}^{liquid} / \rho_{el}^{solid}$	2.20 <sup>b</sup>		

10 *Fabian Wagle and Gerd Steinle-Neumann*

**Table S4.** Thermophysical properties of transition metals with partially occupied  $d$ -bands at  $T_m$ . The resistivity ratio is in good agreement with the long-wavelength approximation to Ziman’s formula (equation 5). References are labeled as follows: *Faber* (1972)<sup>b</sup>, *Hess et al.* (1994)<sup>h</sup>, *Tsu et al.* (1985)<sup>i</sup>, *Schramm* (1962)<sup>j</sup>, *Brillo & Egrý* (2003)<sup>k</sup>, *Owen & Yates* (1936)<sup>l</sup>, *Desai* (1987)<sup>m</sup>, *Alers et al.* (1960)<sup>n</sup>.

		liquid	solid	$\frac{\rho_{el}^{liquid}}{\rho_{el}^{solid}} \left( \frac{\varrho^{liquid}}{\varrho^{solid}} \right)^2 \left( \frac{\beta_T^{liquid}}{\beta_T^{solid}} \right)^{-1}$
<b>Fe</b>		see table 1		<b>1.0</b>
<b>Co</b>	$\varrho$ [g cm <sup>-3</sup> ]	7.90 <sup>h</sup>	8.28 <sup>h</sup>	
	$\beta_T$ [GPa <sup>-1</sup> ]	1/103 <sup>i</sup>	1/109 <sup>j</sup>	<b>0.9</b>
	$T_m$ [K]		1765 <sup>i</sup>	
	$\rho_{el}^{liquid}/\rho_{el}^{solid}$		1.09 <sup>b</sup>	
<b>Ni</b>	$\varrho$ [g cm <sup>-3</sup> ]	7.93 <sup>k</sup>	8.07 <sup>l</sup>	
	$\alpha$ [10 <sup>-5</sup> K <sup>-1</sup> ]		6.83 <sup>l</sup>	
	$c_P$ [J g <sup>-1</sup> K <sup>-1</sup> ]		0.70 <sup>m</sup>	
	$\beta_S$ [GPa <sup>-1</sup> ]		1/147 <sup>n</sup>	<b>1.1</b>
	$\beta_T$ [GPa <sup>-1</sup> ]	1/102 <sup>i</sup>	1/121	
	$T_m$ [K]		1726 <sup>i</sup>	
	$\rho_{el}^{liquid}/\rho_{el}^{solid}$		1.33 <sup>b</sup>	

**Table S5.** Thermophysical properties of metals with fully occupied  $d$ -bands at  $T_m$ . The resistivity ratio is systematically underestimated by Ziman’s long-wavelength approximation (equation 5). References are labeled as follows: *Faber* (1972)<sup>b</sup>, *Blairs* (2006)<sup>d</sup>, *Owen & Yates* (1934)<sup>l</sup>, *Chang & Himmel* (1966)<sup>o</sup>, *Kanai & Tsuchiya* (1993)<sup>p</sup>, *Grønvold & Stølen* (2003)<sup>a</sup>, *Ledbetter* (1977)<sup>r</sup>

		liquid	solid	$\frac{\rho_{el}^{liquid}}{\rho_{el}^{solid}} \left( \frac{\rho^{liquid}}{\rho^{solid}} \right)^2 \left( \frac{\beta_T^{liquid}}{\beta_T^{solid}} \right)^{-1}$
<b>Cu</b>	$\rho$ [g cm <sup>-3</sup> ]	8.10 <sup>d</sup>	8.44 <sup>b,d</sup>	
	$\beta_T$ [GPa <sup>-1</sup> ]	1/67 <sup>d</sup>	1/91 <sup>o</sup>	
	$T_m$ [K]		1356 <sup>b</sup>	<b>1.4</b>
	$\rho_{el}^{liquid} / \rho_{el}^{solid}$		2.10 <sup>b</sup>	
<b>Ag</b>	$\rho$ [g cm <sup>-3</sup> ]	9.33 <sup>d</sup>	9.68 <sup>b,d</sup>	
	$\beta_T$ [GPa <sup>-1</sup> ]	1/52 <sup>d</sup>	1/66 <sup>o</sup>	
	$T_m$ [K]		1233 <sup>b</sup>	<b>1.5</b>
	$\rho_{el}^{liquid} / \rho_{el}^{solid}$		2.10 <sup>b</sup>	
<b>Au</b>	$\rho$ [g cm <sup>-3</sup> ]	17.3 <sup>d</sup>	18.2 <sup>b,d</sup>	
	$\beta_T$ [GPa <sup>-1</sup> ]	1/76 <sup>d</sup>	1/116 <sup>o</sup>	
	$T_m$ [K]		1336 <sup>b</sup>	<b>1.4</b>
	$\rho_{el}^{liquid} / \rho_{el}^{solid}$		2.30 <sup>b</sup>	
<b>Zn</b>	$v_p$ [km s <sup>-1</sup> ]	2.85 <sup>p</sup>		
	$\rho$ [g cm <sup>-3</sup> ]	6.53 <sup>p</sup>	6.92 <sup>l</sup>	
	$\alpha$ [10 <sup>-5</sup> K <sup>-1</sup> ]	14.3 <sup>p</sup>	11.3 <sup>l</sup>	
	$c_P$ [J g <sup>-1</sup> K <sup>-1</sup> ]	0.51 <sup>a</sup>	0.47 <sup>a</sup>	
	$\beta_S$ [GPa <sup>-1</sup> ]	1/53	1/61 <sup>r</sup>	
	$\beta_T$ [GPa <sup>-1</sup> ]	1/43	1/52	
	$T_m$ [K]		693 <sup>b</sup>	<b>1.6</b>
	$\rho_{el}^{liquid} / \rho_{el}^{solid}$		2.20 <sup>b</sup>	



## **(Eidesstattliche) Versicherungen und Erklärungen**

(§9 Satz 2 Nr. 3 PromO BayNAT)

Hiermit versichere ich eidesstattlich, dass ich die Arbeit selbstständig verfasst und keine anderen als die von mir angegebenen Quellen und Hilfsmittel benutzt habe (vgl. Art. 64 Abs. 1 Satz 6 BayHSchG).

(§9 Satz 2 Nr. 3 PromO BayNAT)

Hiermit erkläre ich, dass ich die Dissertation nicht bereits zur Erlangung eines akademischen Grades eingereicht habe und dass ich nicht bereits diese oder eine gleichartige Doktorprüfung endgültig nicht bestanden habe.

(§9 Satz 2 Nr. 4 PromO BayNAT)

Hiermit erkläre ich, dass ich Hilfe von gewerblichen Promotionsberatern bzw. -vermittlern oder ähnlichen Dienstleistern weder bisher in Anspruch genommen habe noch künftig in Anspruch nehmen werde.

(§9 Satz 2 Nr. 7 PromO BayNAT)

Hiermit erkläre ich mein Einverständnis, dass die elektronische Fassung meiner Dissertation unter Wahrung meiner Urheberrechte und des Datenschutzes einer gesonderten Überprüfung unterzogen werden kann.

(§9 Satz 2 Nr. 8 PromO BayNAT)

Hiermit erkläre ich mein Einverständnis, dass bei Verdacht wissenschaftlichen Fehlverhaltens Ermittlungen durch universitätsinterne Organe der wissenschaftlichen Selbstkontrolle stattfinden können.

Bayreuth, den 10. September 2018